

FLOW AROUND CYLINDRICAL TOWERS: THE STABILISING ROLE OF VERTICAL RIBS

LT ALBERTI

**Thesis presented in partial fulfilment of the requirements for the
degree of Master of Engineering (Civil)
at the University of Stellenbosch**



PROF. GPAG VAN ZIJL
Study leader

STELLENBOSCH

December 2006

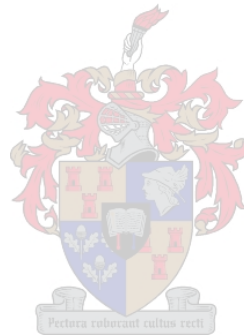
DECLARATION

I, the undersigned, hereby declare that the work contained in this thesis is my own original work and that I have not previously in its entirety or in part submitted it at any university for a degree.

Signature:

LT Alberti

Date:



SUMMARY

The aim of this thesis is to study the stabilising effect which vertical ribs may have on a tall cylindrical structure, with the focus on the proposed Solar Chimney.

The report begins with a brief introduction to the Solar Chimney concept. A study is made of flow regimes which exist for flow around a circular cylinder and these flow regimes, together with their characteristics, are described. Various threats to the Solar Chimney are identified and will be investigated. The natural shape and strength of the Saguaro Cactus leads to the investigation of vertically ribbed cylinders.

Experimental wind tunnel tests are performed in Tokyo, Japan to obtain external pressure distributions. A smooth cylindrical model, as well as two different configurations of vertically ribbed cylinders are tested. These external pressure distributions are numerically integrated in order to obtain calculated drag coefficient values for the cylinders.

The drag coefficients for a smooth cylinder and cylinders with vertical ribs are obtained experimentally by means of total drag force measurements. These tests were performed in the wind tunnel at the University of Stellenbosch. The effect of aspect ratio of a smooth cylinder is also addressed.

Computational Fluid Dynamics (CFD) analyses are carried out using the CFD software program, FLUENT. Both the drag coefficient and the external pressure distributions were investigated in this way. The differences between theoretical conditions and those of real life conditions of a smooth cylinder are discussed.

The report ends by concluding the stabilising effect of vertical ribs on tall cylindrical structures and how these ribs may eliminate some of the present threats to the proposed Solar Chimney.

SAMEVATTING

Die doel van hierdie tesis is om die stabiliseringseffek van vertikale ribbe om silindriese strukture te ondersoek, met die klem op die voorgestelde Sontoring.

As inleiding word 'n kort agtergrond van die Sontoring gegee. Vloei rondom 'n sirkelvormige silinder word vanuit literatuur bestudeer. Die verskillende vloiepatrone en eienskappe word hier verduidelik. Gevare tot die stabiliteit van die Sontoring is geïdentifiseer en sal ondersoek word. Die idee van 'n vertikaal geribde struktuur kom uit die natuur vanaf die Saguaro Kaktus.

Eksperimentele windtonnel toetse is in Tokyo, Japan uitgevoer om die eksterne drukverspreiding te bepaal. 'n Sirkelvormige silinder asook twee verskillende vertikaal geribde silinders word getoets. Die eksterne drukverspreiding word numeries integreer om die weerstandskoeffisiënt te bereken vir die onderskeie silinders.

Die weerstandskoeffisiënt vir 'n sirkelvormige silinder asook vir vertikaal geribde silinders word eksperimenteel bereken vanaf die totale weerstandskrag. Hierdie toetse is onderneem in die Universiteit van Stellenbosch se windtonnel. Die invloed van die hoogte tot deursnee aspek van die silinder word aangespreek.

Berekeningsvloeiameganika (CFD) analise word uitgevoer met FLUENT CFD programmatuur. Beide die weerstandskoeffisiënt en die eksterne drukverspreiding word hiermee ondersoek. Die verskille tussen teoretiese en ware vloei rondom 'n sirkelvormige silinder word bespreek.

Hierdie verslag sluit af deur die stabiliseringseffek van vertikale ribbe op hoë silindriese strukture op te som, asook hoe hierdie ribbe sekere van die huidige gevare op die voorgestelde Sontoring teenwerk.

ACKNOWLEDGEMENTS

Prof GPAG van Zijl, my study leader, for always inspiring me and keeping me motivated.
Also for offering me the wonderful opportunity to travel to Japan.

Prof Y Tamura, for his kind invitation to the COE program, which together with his support,
allowed me to study as a short term researcher in Tokyo, Japan.

Hanno Reuter, for all his time and assistance in introducing me to Fluid Mechanics.

Thomas Kingsley, for his help with FLUENT and guidance in CFD modelling.

Prof TW von Backström and the Department of Mechanical Engineering, for their
cooperation.

Cobus Zietzman and Michael Lorek for their assistance with the Wind Tunnel testing.

Dion Viljoen, Louis Fredericks and the Mechanical workshop guys, for their assistance.



Marlé Lötter, for all the admin work always done efficiently and with a smile.

Sachi Koizumi, for all her help and translations during my stay at Tokyo Polytechnic
University.

Philippe Mainçon, Cobus van Dyk, Darren Pierce, Billy Bosshoff, George Gerber and many
others who helped along the way.

Shimizu Corporation, Tokyo, Japan, for their excellent facilities & assistance with the wind
tunnel testing.

André du Toit, for proof reading, for keeping me sane and giving me a non-engineer's
perspective.

TERMS OF REFERENCE

Transcritical flow and its characteristics need to be studied in order to understand what conditions the proposed Solar Chimney will experience under wind loading.

Experimental tests should be performed with the aim of determining the structural role that vertical ribs may play in stabilising a tall cylindrical tower. Various aspects of flow characteristics such as pressure coefficients and drag need to be tested.

Numerical analyses by means of Computational Fluid Dynamics are to be carried out so as to compare with the experimental results and expand upon them.

Conclusions need to be drawn with regard to the structural stability that vertical ribs may provide to tall cylindrical towers.

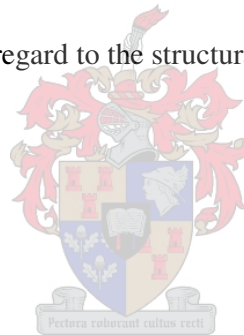
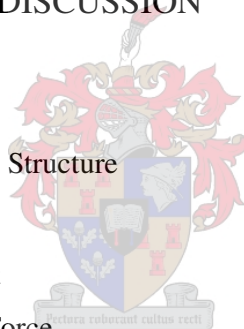


TABLE OF CONTENTS

DECLARATION	
SUMMARY	i
SAMEVATTING	ii
ACKNOWLEDGEMENTS	iii
TERMS OF REFERENCE	iv
TABLE OF CONTENTS	v
SYMBOLS AND ACRONYMS	ix
GLOSSARY	x
1. INTRODUCTION	1
1.1. Background of the Solar Chimney	1
1.2. Theory of Fluid Mechanics	2
1.2.1. Well Established Literature	3
1.2.2. The Purpose of Vertical Ribs	3
1.3. Explanation of Flow Regimes	3
1.4. Possible Threats to the Solar Chimney	11
1.4.1. Cross-Wind Oscillation	11
1.4.2. Along Wind Oscillation	11
1.4.3. Toppling of Chimney	11
1.4.4. Ovalisation	11
1.5. Contribution of this thesis	12
2. INVESTIGATING VERTICAL RIBS – WHY AND HOW	13
2.1. Nature as a Guide	13
2.2. Strategy of Investigation	15
2.2.1. Cross-Wind Oscillation	15
2.2.2. Along Wind Oscillation	15
2.2.3. Toppling of Chimney	15
2.2.4. Ovalisation	16
2.3. Computational Fluid Dynamics	16

2.4. Subject and Objectives of this Report	16
2.5. Limitations and Scope of this Report	16
3. EXTERNAL PRESSURE DISTRIBUTIONS –	
WIND TUNNEL TESTING:	
SHIMIZU CORPORATION, TOKYO, JAPAN	17
3.1. Test Setup	17
3.1.1. Wind Tunnel Testing Facility	17
3.1.2. Models	18
3.1.3. Test Setup	19
3.1.4. Data Acquisition	20
3.1.5. Limitations	20
3.2. Results	20
3.2.1. Fluctuations with Height along Cylinder	20
3.2.2. Effect of Varying Wind Speeds	23
3.2.3. Conclusion: Smooth vs Vertical Ribs	26
3.3. Drag Calculations from Experimental Results	26
3.3.1. Calculation of Drag Coefficient	26
3.3.2. Effect of Vertical Ribs on Drag	27
3.4. Conclusions	28
4. DRAG COEFFICIENTS -	
WIND TUNNEL TESTING:	
UNIVERSITY OF STELLENBOSCH	29
4.1. Experimental Setup	29
4.1.1. Wind Tunnel Testing Facility	29
4.1.2. Models	31
4.1.3. Test Setup	32
4.1.4. Data Acquisition	32
4.1.5. Limitations	33
4.2. Results: Smooth Cylinder	33
4.2.1. The Influence of Aspect Ratio	33
4.2.2. Drag on a Finite Cylinder of Aspect Ratio 2.59	34
4.3. Results: Cylinder with Small Vertical Ribs	35
4.4. Results: Cylinder with Large Vertical Ribs	37

4.5. Conclusions	38
5. COMPUTATIONAL FLUID DYNAMICS	39
5.1. Introduction and Input Parameters	39
5.1.1. GAMBIT – The Meshed Models	40
5.1.2. FLUENT – Conditions	43
5.1.3. Limitations	44
5.2. Drag on a Smooth Cylinder	45
5.2.1. Theoretical Conditions	45
5.2.2. Real Life Conditions	46
5.3. Drag on Vertically Ribbed Cylinders	48
5.4. External Pressure Distributions	50
5.5. Conclusions	55
6. THE STABILISING ROLE OF VERTICAL RIBS: INTERPRETATION AND DISCUSSION	56
6.1. Drag Fluctuation	56
6.2. Pressure Distribution	57
6.3. Forces and Moments on the Structure	58
7. CONCLUSIONS	60
7.1. Stabilised Drag Coefficient	60
7.2. Better Prediction of Drag Force	60
7.3. Reduction in Along Wind Oscillation Threat	60
7.4. Comparable Forces and Moments	61
7.5. Unsymmetrical External Pressure Distribution Eliminated	61
7.6. Stabilised External Pressure Distribution	62
7.7. Reduction of Ovalisation Threat	62
7.8. Cross-wind Oscillation Postulation	62
8. RECOMMENDATIONS AND PROPOSALS FOR FUTURE STUDIES	63
8.1. Dynamic Modelling	63
8.2. Optimum Vertical Rib Size	63
8.3. Transcritical Flow Regime	63
8.4. Flow Visualisation	64
8.5. Aero-elastic Model Testing	64

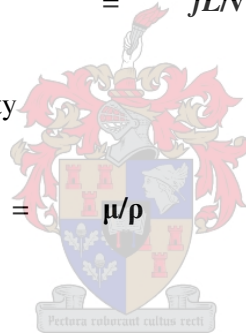


9. REFERENCES	65
APPENDIX A: DETAILED REPORT OF WIND TUNNEL TESTING: SHIMIZU CORPORATION, TOKYO, JAPAN	68
APPENDIX B: WIND TUNNEL TEST RESULTS: SHIMIZU CORPORATION, TOKYO, JAPAN	76
APPENDIX C: DETAILED REPORT OF WIND TUNNEL TESTING: UNIVERSITY OF STELLENBOSCH	91
APPENDIX D: WIND TUNNEL TEST RESULTS: UNIVERSITY OF STELLENBOSCH	100
APPENDIX E: FLUENT CFD RESULTS	106
APPENDIX F: MATLAB PROGRAMMES	114
LIST OF ILLUSTRATIONS	129
LIST OF TABLES	130
LIST OF EQUATIONS	131



SYMBOLS AND ACRONYMS

A	frontal area	
C_d	drag coefficient	
C_p	external pressure coefficient	
D	diameter	
f	frequency of vortex shedding	
F_d	drag force	
k_s	roughness parameter	
L	characteristic length	
Re	Reynold's number	= vD/ν
St	Strouhal number	= fL/v
v	velocity	
μ	coefficient of viscosity	
ρ	density	
ν	kinematic viscosity	= μ/ρ

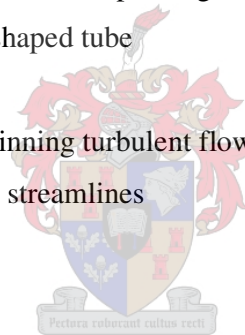


AR	Aspect Ratio
CFD	Computational Fluid Dynamics
PISO	Pressure Implicit with Splitting of Operators
SIMPLE	Semi-Implicit Method for Pressure Linked Equations
US	University of Stellenbosch

GLOSSARY

Aspect Ratio	the ratio of the cylinder's height over diameter
Boundary Layer	the layer of slower flow of a fluid due to friction with the surface over which it is flowing
Bridge Amplifier	cancels out the large background voltages and currents before they enter the input of an electronic amplifier so that all of the amplification available can be used to measure the small changes that are of interest
Gradient Height	is the height at which the vertical wind profile is fully developed and no longer affected by the boundary layer
Hypodermic pipes	thin hollow pipes
Ovalisation	a failure mode of a cylindrical tower where the circular shape of the tower is deformed or made oval
Pressure Transducer	is a device that converts the mechanical force of applied pressure into electrical energy
Resonance	is an increase in the oscillatory energy absorbed by a system when the frequency of the oscillations matches the system's natural frequency of vibration (its <i>resonant frequency</i>)
Reynolds Number	is a flow parameter used to classify dynamically similar flows, i.e. flows which have geometrical similar streamlines around geometrical similar bodies ($R_e = vD/\nu$)

Separation Angle	the angle at which flow breaks away from the wall of the cylinder to form the wake downstream of the cylinder
Selection Box	selects each channel and conveys its pressure measurement to the transducer
Stagnation Point	is the point at which the airflow divides
Supercritical Regime	is the flow regime in the Reynolds number range of $3 \times 10^5 < Re < 10^6$
Transcritical Flow	is the flow regime of Reynolds numbers greater than 10^6
Venturi	is a system for speeding the flow of air, by constricting it in a cone-shaped tube
Vortex	is a spinning turbulent flow (or any spiral whirling motion) with closed streamlines



1. INTRODUCTION

This report forms part of the Master of Civil Engineering Degree at the University of Stellenbosch. It focuses on the effect of vertical ribs on cylindrical towers. The motivation for this research is based on the proposed Solar Chimney.

1.1 Background on the Solar Chimney

The Solar Chimney, or Solar Updraft Tower, was the idea of German Engineer, Jörg Schlaich. It is proposed to be a solution to the world's energy crisis, by providing a source of environmentally friendly electrical power. The challenge now lies in who will be first to successfully construct his challenging idea.

The Solar Chimney principle is illustrated in Figure 1.1.

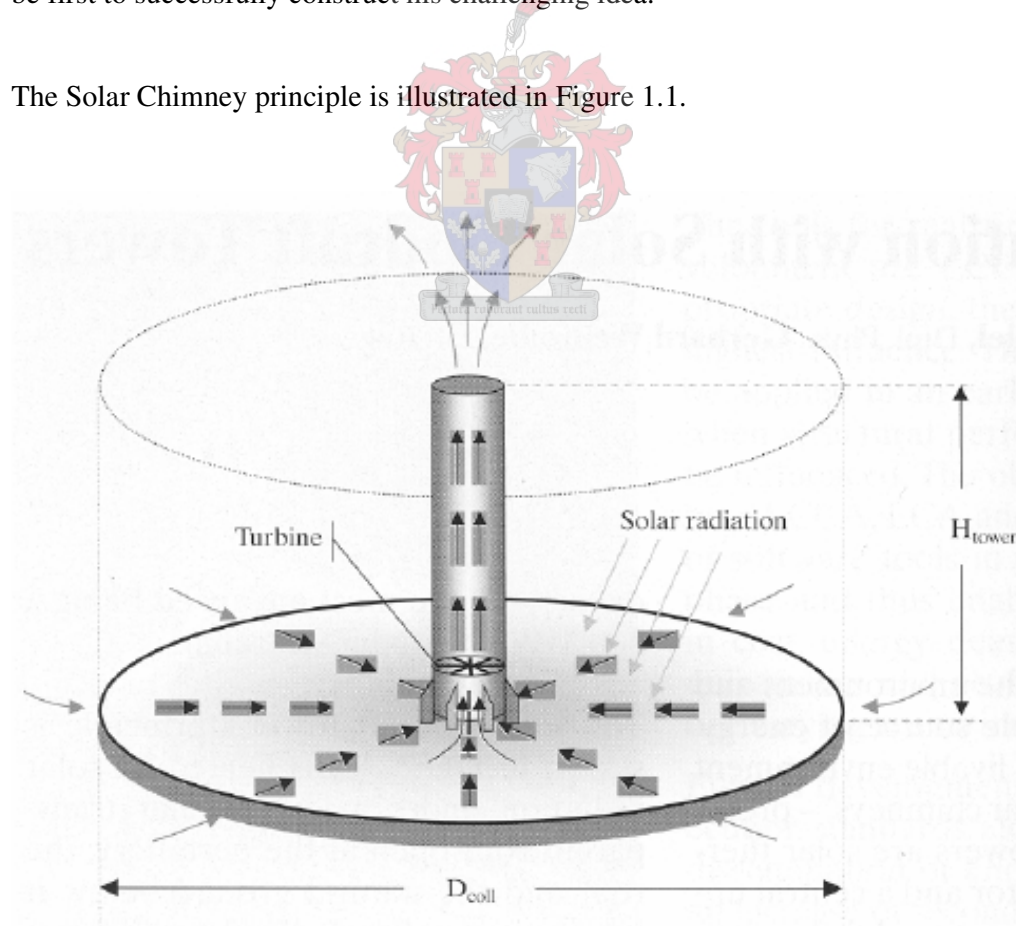


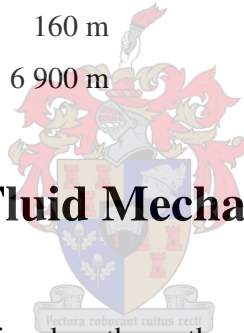
Figure 1.1: Solar Chimney Principle (Schlaich, 2004)

Air below a transparent circular collector is heated by solar radiation. A large chimney structure, with inlets at its base, is situated in the centre of the collector. The hot air below the collector naturally rises up the chimney. This causes a suction effect which draws atmospheric air in from the open perimeter of the collector. As the hot air rises up the chimney, it flows through either one large turbine, or numerous smaller turbines (this is still to be determined). These turbines are linked to conventional generators. A conversion of heat energy to kinetic energy, kinetic energy to mechanical energy and mechanical energy to electric energy is thus achieved.

The dimensions for a full scale, 200 MW Solar Chimney are changing as research furthers and optimisations are made. At the University of Stellenbosch, research is presently being done using the following proposed dimensions (Van Dyk, 2001):

Tower height:	1 500 m
Tower diameter:	160 m
Collector diameter:	6 900 m

1.2 Theory of Fluid Mechanics



The theory of fluid mechanics involves the mathematical modelling of fluid flow by means of obtaining differential equations from the fundamental laws of physics. These include differential equations of continuity, momentum and energy. Full explanations of the development of these differential equations can be found in *Mechanics of Fluids* by Potter and Wiggert.

Computational Fluid Dynamics (CFD) is similar to Finite Element Analysis. In CFD, the fluid moving around the body is analysed based on the finite volume method. In order to achieve this, the fluid domain is discretized into a finite set of control volumes and the algebraic differential equations are solved. For this study, the software program FLUENT was used to perform the CFD analyses.

1.2.1 Well Established Literature

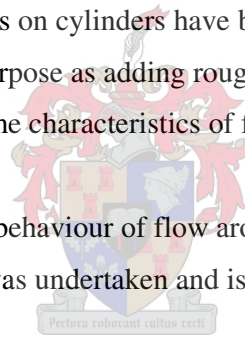
A large amount of literature is available on flow around smooth cylinders. Due to its size, the proposed Solar Chimney falls entirely into the transcritical flow regime. Unfortunately, existing literature is limiting in that it does not reach into the transcritical flow regime.

As literature shows, the flow around smooth cylinders is very sensitive. Even the slightest imperfection or roughness may have a large influence on the flow characteristics such as drag coefficient or pressure distribution around the cylinder.

1.2.2 The Purpose of Vertical Ribs

Many different roughnesses on cylinders have been studied. The idea of vertical ribs does not serve the same purpose as adding roughness, but serves rather to change the shape of the cylinder and the characteristics of flow around it.

In order to understand the behaviour of flow around a cylinder, an in depth study of the various flow regimes was undertaken and is summarised as an explanation of flow regimes.



1.3 Explanation of Flow Regimes

Reynolds number (R_e) is a flow parameter used to classify dynamically similar flows, i.e. flows which have geometrical similar streamlines around geometrically similar bodies.

$$R_e = \frac{vD}{\nu} \quad (1.1)$$

Where

- v = crosswind velocity
- D = diameter of cylinder
- ν = kinematic viscosity of air

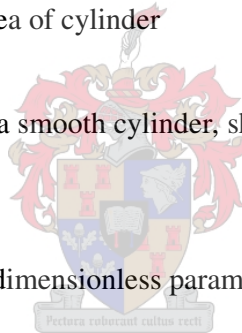
Different flow regimes display different flow characteristics. Flows which display similar characteristics (usually at similar Reynolds numbers) are grouped together and described by a certain flow regime. The following is an explanation of various flow regimes around circular cylinders based on Reynolds number.

The drag force (F_d) on a cylinder can be expressed in terms of a dimensionless drag coefficient (C_d). The drag coefficient is a function of the object's shape as well as the properties of the fluid moving past the object. In the case of a cylinder, the drag coefficient is described as follows:

$$C_d = \frac{F_d}{0.5 \rho v^2 A} \quad (1.2)$$

Where ρ = density of air
 v = wind speed
 A = frontal area of cylinder

The drag coefficient graph for a smooth cylinder, showing the various flow regimes can be seen in Figure 1.2.



The Strouhal number (St) is a dimensionless parameter used to describe vortex shedding and is defined as follows:

$$St = \frac{fL}{v} \quad (1.3)$$

Where f = frequency of vortex shedding
 L = characteristic length
 v = wind speed

All values given here are approximations, due to variation caused for example by surface roughness, and cannot be taken as exact. It is not possible to exactly define the Reynolds numbers range at which each flow regime exists. The aim is however to understand the transitions between flow regimes and their impact on structural stability.

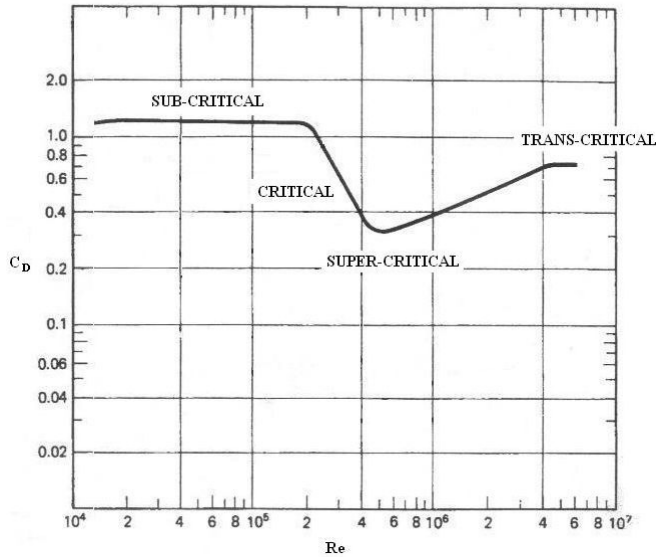
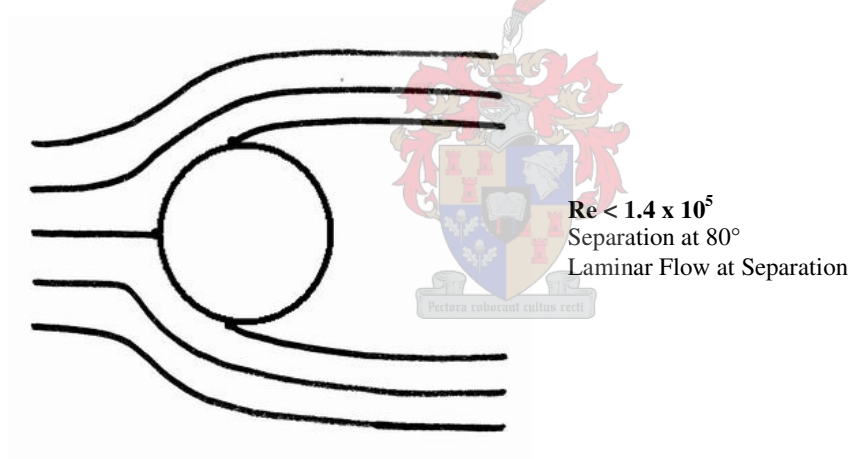


Figure 1.2: Drag Coefficient for a Smooth Cylinder

SUB-CRITICAL FLOW REGIME

$$\underline{(Re < 1.4 \times 10^5)}$$



Boundary layer and Separation

The boundary layer is in a stable condition of laminar flow. Separation occurs while the boundary layer remains laminar. Separation takes place at 80° from the approach angle of flow. A wide wake downstream of the cylinder forms due to this small angle at which separation occurs.

Drag

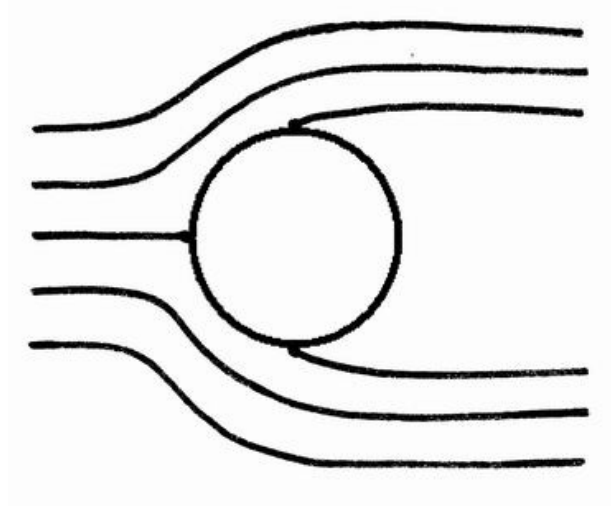
The mean drag co-efficient C_D is observed as 1.2.

Strouhal

The Strouhal number is 0.2.

CRITICAL FLOW REGIME (a)

$(1.4 \times 10^5 < Re < 2.8 \times 10^5)$



$1.4 \times 10^5 < Re < 2.8 \times 10^5$
 Separation at 90°
 Laminar Flow at Separation

Boundary layer and Separation

The boundary layer is still in a stable condition of laminar flow. Separation occurs while the boundary layer remains laminar. The angle at which separation takes place begins to increase (from 80°), thus causing the wake downstream of the cylinder to narrow.

Drag

The mean drag co-efficient C_D decreases gradually from 1.2 to 0.8.

Strouhal

The Strouhal number remains 0.2.

**CRITICAL FLOW REGIME (b)**

$(2.8 \times 10^5 < Re < 3.0 \times 10^5)$

Boundary layer and Separation

The boundary layer becomes unstable. Random changes which cannot be described occur during this transition. The angle at which separation takes place continues to increase, thus causing the wake downstream of the cylinder to narrow.

Drag

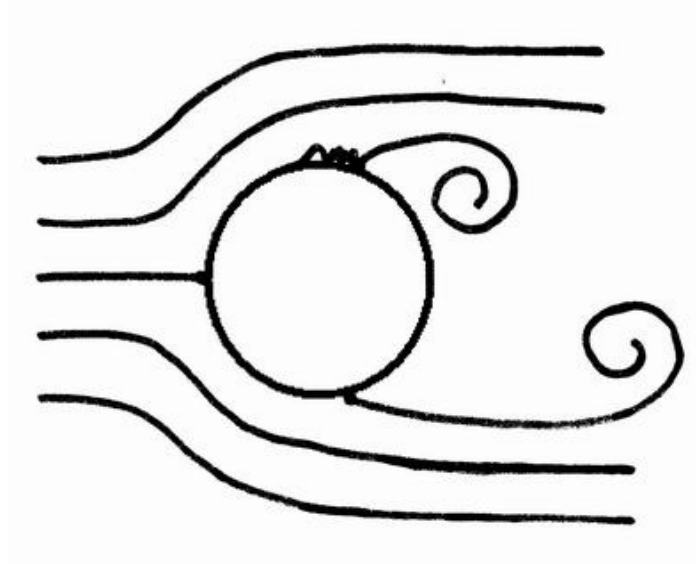
The mean drag co-efficient C_D continues to decrease from 0.8 to 0.6.

Strouhal

The Strouhal number remains 0.2.

CRITICAL FLOW REGIME (c)

$(3.0 \times 10^5 < Re < 3.3 \times 10^5)$



$2.8 \times 10^5 < Re < 3.3 \times 10^5$
 Separation at 100°
 Alternating Separation Bubble

Boundary layer and Separation

The boundary layer becomes bi-stable. This means that alternating sides of the boundary layer around the cylinder appear to be stable. One-sided separation occurs at alternating sides of the cylinder. This alternation of pressure forces causes a punching effect on the sides of the cylinder, which may result in oscillation of the cylinder.

Separation occurs by means of the formation of a separation bubble. This separation bubble is formed by the boundary layer's laminar flow being disturbed, thus separating from the surface. The flow then becomes turbulent and reattaches to the cylinder for a short distance until finally separating from the cylinder to form a wake.

The angle at which alternating separation takes place is 100° , thus causing the wake downstream of the cylinder to be narrower than that of the sub-critical flow regime.

Drag

The mean drag co-efficient C_D continues to decrease to 0.5.

Strouhal

The Strouhal number increases to 0.33.

CRITICAL FLOW REGIME (d)

$(3.3 \times 10^5 < Re < 3.5 \times 10^5)$

Boundary layer and Separation

The boundary layer once again becomes unstable as it undergoes transition. Random changes occur during this transition. The angle at which separation takes place continues to increase, thus causing the wake downstream of the cylinder to narrow.

Drag

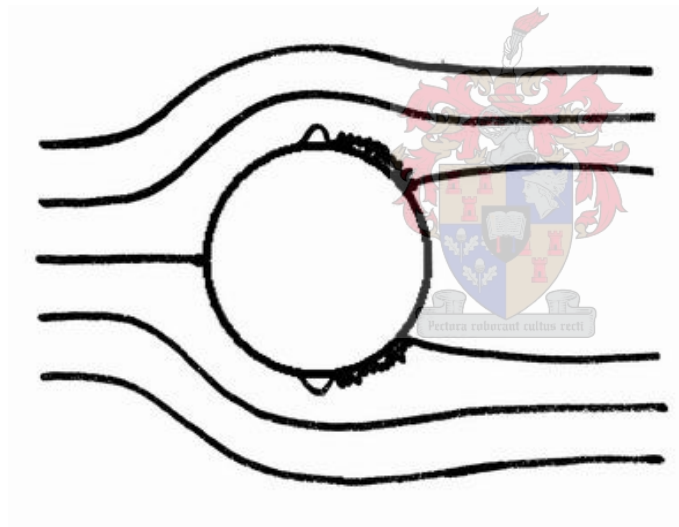
The mean drag co-efficient C_D continues to decrease from 0.5 to 0.4.

Strouhal

The Strouhal number decreases slightly to 0.31.

SUPER-CRITICAL FLOW REGIME

$(3.5 \times 10^5 < Re < 1.0 \times 10^6)$



$3.5 \times 10^5 < Re < 1.0 \times 10^6$
Separation at 140°
Separation Bubbles Both Sides

Boundary layer and Separation

The boundary layer becomes stable once again. Separation occurs simultaneously at both sides of the cylinder by means of the formation of two separation bubbles (one at each side of the cylinder). A separation bubble is formed by the boundary layer's laminar flow being disturbed and thus separating from the surface. The flow then becomes turbulent and reattaches to the cylinder for a short distance until finally separating from the cylinder to form a wake.

Separation takes place at 140° from the approach angle of flow. A narrow wake downstream of the cylinder forms due to this large angle at which separation occurs. This wake is narrower than the wake in both the sub-critical and critical flow regimes.

Drag

The mean drag co-efficient C_D is observed to be at its lowest value, 0.3.

Strouhal

The Strouhal number increases to 0.48.

TRANSITION

$$\mathbf{(1.0 \times 10^6 < Re < 5.0 \times 10^6)}$$

Boundary layer and Separation

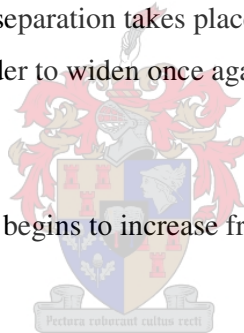
The boundary layer once again becomes unstable. Random changes occur during this transition. The angle at which separation takes place begins to decrease, thus causing the wake downstream of the cylinder to widen once again.

Drag

The mean drag co-efficient C_D begins to increase from 0.3 to 0.8.

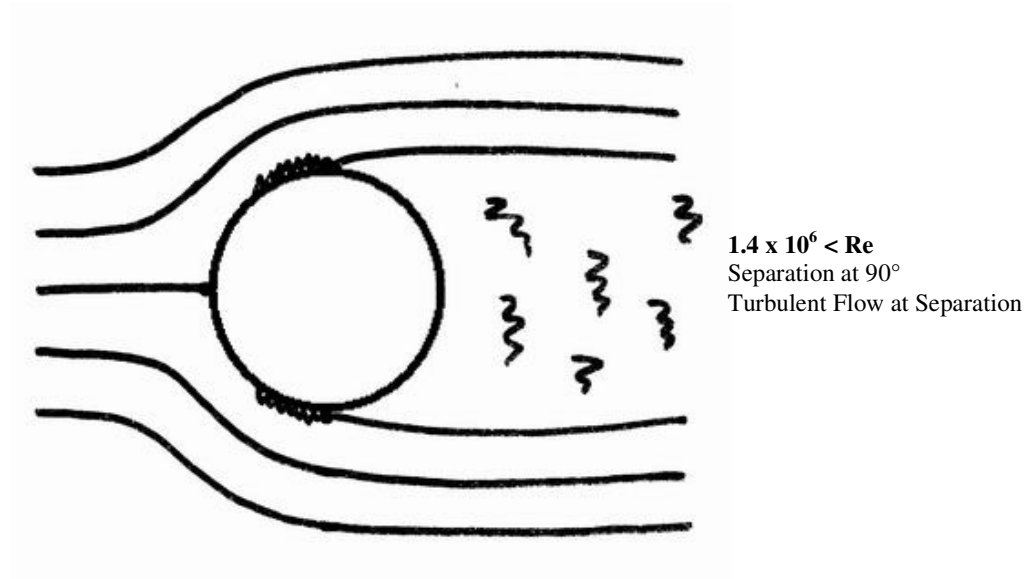
Strouhal

The Strouhal number is unstable and varies from 0.1 to 0.45.



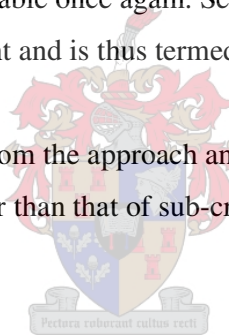
TRANS-CRITICAL FLOW REGIME

$(5.0 \times 10^6 < Re)$

**Boundary layer and Separation**

The boundary layer becomes stable once again. Separation occurs only after the boundary layer is fully turbulent and is thus termed turbulent separation.

Separation takes place at 90° from the approach angle of flow. The wake downstream of the cylinder is slightly narrower than that of sub-critical flow, but wider than that of critical and super-critical flow.

**Drag**

The mean drag co-efficient C_D is observed to remain constant at a value of 0.8.

Strouhal

The Strouhal number is 0.28.

1.4 Possible Threats to the Solar Chimney

The following are some of the possible threats which have been identified for the Solar Chimney.

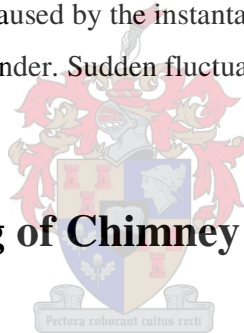
1.4.1 Cross Wind Oscillation

Cross wind oscillation is caused by the uneven shedding of vortices. This is best observed by means of flow visualisation.

1.4.2 Along Wind Oscillation

Along wind oscillation is caused by the instantaneous variation in pressure distribution around the cylinder. Sudden fluctuations of drag force can also cause along wind excitation.

1.4.3 Toppling of Chimney



Toppling of the chimney would be due to the moment about the base of the chimney. This is a function of the total pushover force which in turn is influenced by the drag coefficient.

1.4.4 Ovalisation

This is caused by large variation in pressure distribution around the cylinder, causing the cylinder to distort from its circular shape.

1.5 Contribution of this Thesis

This thesis will help to quantify the stabilising role of vertical ribs on a cylindrical structure in terms of the above mentioned areas of concern. Experimental work is done in order to investigate the external pressure coefficients as well as drag of vertically ribbed cylinders. Computational Fluid Dynamics is used to verify these results and extrapolate them. This thesis aims to shed light on the structural behaviour of vertically ribbed cylinders in comparison to smooth cylindrical structures.



2. INVESTIGATING VERTICAL RIBS - WHY AND HOW

2.1 Nature as a Guide

The Saguaro Cactus (Figure 2.1) can grow to a height of 15 m tall. They are cylindrical structures with diameters of 0.3 m to over 0.8 m. This h/d ratio, where h = height and d = diameter, compares with the Solar Chimney's proposed h/d ratio of approximately 9. The Saguaro Cactus is exposed to extreme wind conditions and has adapted to withstand these wind forces that are encountered in its natural environment. It experiences flows at Reynolds numbers up to $Re = 10^6$, which may place it in the transcritical zone together with the Solar Chimney.

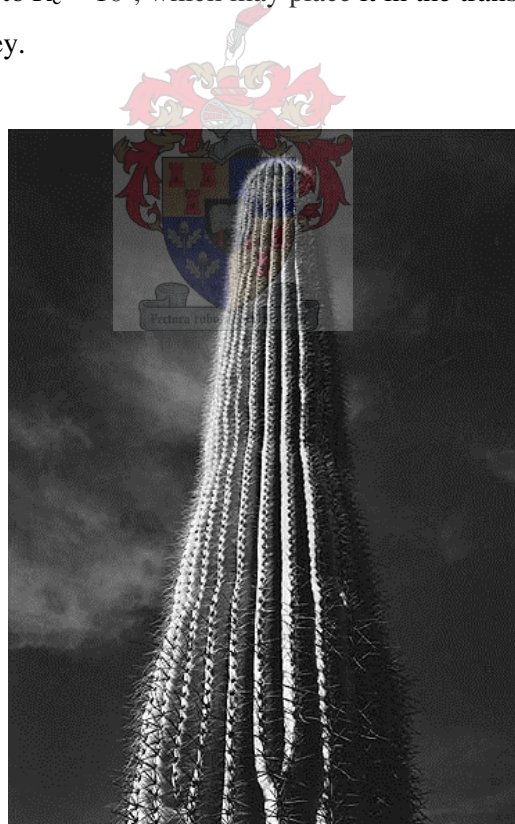


Figure 2.1: The Saguaro Cactus (Talley, 2002)

Hence, the proposal arises to look towards the Saguaro Cactus for a favourable aerodynamic buff body for the Solar Chimney.

Studies on the behaviour of flow around cactus shaped cylinders have been conducted and a short summary of their results follow (Talley, 2002).

The complex surface geometry of Saguaros is caused by longitudinal cavities and spines. Only the effect of the longitudinal cavities has been investigated. The number of cavities depends on the trunk diameter so as to maintain a fraction cavity depth (l/d , where l = depth of the cavity and d = diameter of the cylinder) of approximately 0.07 at a height of 1.5 m.

The results of five different cylinders are shown in Figure 2.2 where the l/d ratio is varied, one cylinder is smooth and one cylinder has a uniform roughness of $k_s/d = 8.41 \times 10^{-3}$.

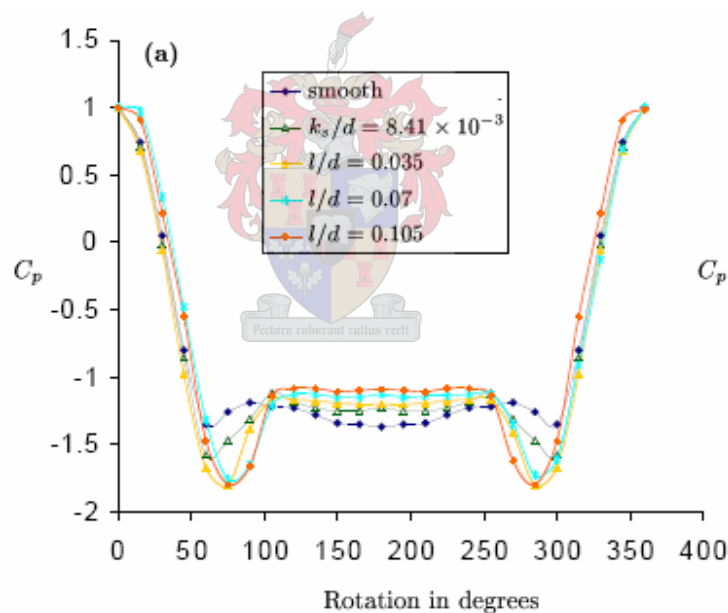


Figure 2.2: Pressure distribution of all cylinders at $Re = 1.1 \times 10^5$ (Talley, 2002)

It can be seen that there is a greater pressure recovery (the reduction of suction at the back of the cylinder) for cylinders with cavities than for smooth and rough cylinders, but also that the cylinders with cavities have greater negative pressures on the sides of the cylinder.

The exact secret of the damping mechanism of the Saguaro Cactus, or vertical ribs, has not yet been revealed. Thorough testing at a range of Reynolds Numbers that include both super-critical and transcritical flows would be necessary to better understand the natural damping mechanism of the Saguaro Cactus.

2.2 Strategy of Investigation

Different methods are necessary in order to investigate each of the possible threats to (failure modes of) the Solar Chimney.

2.2.1 Cross Wind Oscillation

The postulation is made that cross wind oscillation is not a threat to the solar chimney in the transcritical flow regime into which it falls. This postulation is made based on theoretical studies of the various flow regimes (Chapter 1) and their developments. Experimental research in this regard does not form part of this thesis.

2.2.2 Along Wind Oscillation

To be investigated by means of obtaining the external pressure distribution around the models experimentally in Japan. The fluctuation of drag coefficient will be tested in the University of Stellenbosch (US) wind tunnel as this will also influence along wind oscillation.

2.2.3 Toppling of Chimney

To be tested experimentally in the US wind tunnel by measuring the total drag force on the chimney and obtaining the drag coefficients. Total force diagrams and moments about the base of the chimney will also be discussed in the concluding chapters.

2.2.4 Ovalisation

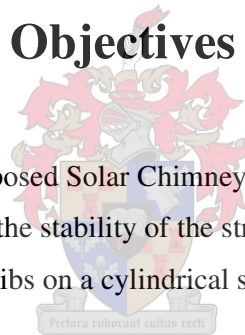
To be investigated by obtaining the external pressure distribution around the cylinder models experimentally in Japan.

2.3 Computational Fluid Dynamics

Computational Fluid Dynamics (CFD) is used to expand upon the experimental conditions. A more detailed understanding of sensitivity parameters such as model smoothness and air turbulence is also investigated. The computer program FLUENT was used for these CFD analyses.

2.4 Subject and Objectives of this Report

Wind forces acting on the proposed Solar Chimney are, at this stage of research, perceived as a great danger to the stability of the structure. This report takes a look at the stabilising role of vertical ribs on a cylindrical structure.



The objectives of this report are to quantify the effect of vertical ribs on each one of the failure mechanisms of the Solar Chimney. An attempt will also be made to make reliable postulations as to flow behaviour into the transcritical flow regime.

2.5 Limitations and Scope of this Report

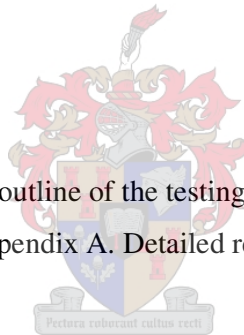
Due to the limitations which exist in being able to experimentally obtain transcritical Reynolds numbers, the experimental work done for this thesis is carried out at lower Reynolds numbers. CFD analyses are also not able to be carried out at transcritical flow conditions due to the lack of numerical solver for such conditions.

3. EXTERNAL PRESSURE DISTRIBUTIONS – WIND TUNNEL TESTING: SHIMIZU CORPORATION, TOKYO, JAPAN

The aim of the experiment is to investigate the effect of vertical ribs on the external pressure distribution on a circular cylinder.

3.1 Test Setup

This section gives only a brief outline of the testing procedure. For a detailed report of testing methods, please see Appendix A. Detailed results of the tests can be found in Appendix B.



3.1.1 Wind Tunnel Testing Facility

Wind tunnel tests were performed in the closed circuit wind tunnel at the Shimizu Corporation, Institute of Technology in Tokyo, Japan. A photo of a model of the wind tunnel can be seen in Figure 3.1.

Maximum wind speeds of 35 m/s can be generated in the wind tunnel by the 4m diameter fan. Small vibrations of the model were however observed at wind speeds above 25m/s resulting in the maximum tested wind speed being 25m/s.

The testing section has size 3.5m width x 20m length x 2.5m height. The model size was thus determined in order to ensure a blockage ratio of less than 5%. The blockage ratio for the models was 4%.

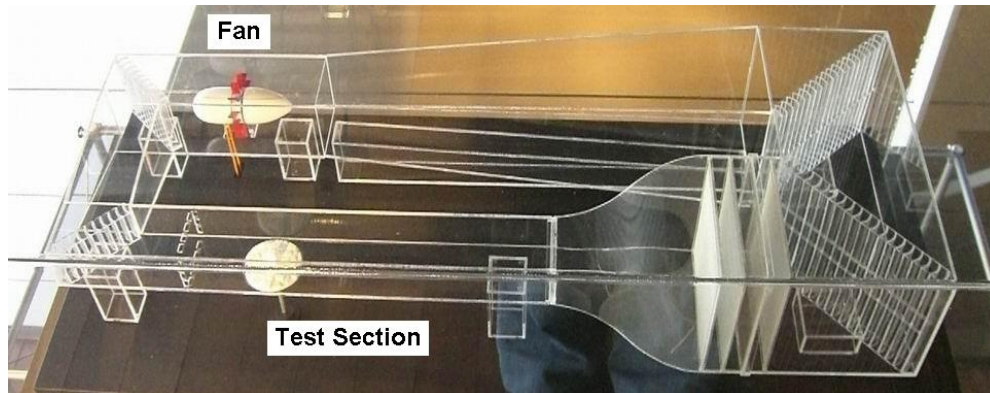


Figure 3.1: The Model of the Closed Circuit Wind Tunnel, Shimizu Corporation, Tokyo, Japan.

3.1.2 Models

Three different chimney models were used. All models were 1000 mm in length (height) and closed at the top end to reduce 3D flow effects. 300 mm diameter Perspex pipe was used for all three models. V-shaped Perspex strips were added around two of the models in order to create vertical ribs.

The first model was a smooth circular cylinder with outer diameter of 300 mm. The aspect ratio ($AR = \text{height} / \text{diameter}$) of the smooth cylinder was $1000/300 = 3.33$. Pressure taps were placed every 8° around the circumference of the cylinder. There were three rows of these pressure taps at heights of 400 mm, 500 mm and 600 mm from the base.

The second model was a cylinder with 45 vertical ribs (one vertical rib every 8°). The ribs extended 21 mm from the circular pipe, making the cylinder outer diameter 342 mm. The l/d ratio of the model (where $l = \text{depth of vertical rib}$ and $d = \text{diameter of cylinder}$) was thus $21/300 = 0.07$. Pressure taps were placed every 8° around the circumference of the cylinder between the vertical ribs (on the circular cylinder

wall). There were three rows of these pressure taps at heights of 400 mm, 500 mm and 600 mm from the base.

The third model was that of a cylinder with 90 vertical ribs (one vertical rib every 4°). The ribs extended 21 mm from the circular pipe, making the cylinder outer diameter 342 mm. The l/d ratio of the model was thus $21/300 = 0.07$. Pressure taps were placed every 8° around the circumference of the cylinder between every second vertical rib (on the circular cylinder wall). There were three rows of these pressure taps at heights of 400 mm, 500 mm and 600 mm from the base.

The three models are shown schematically in Figure 3.2.

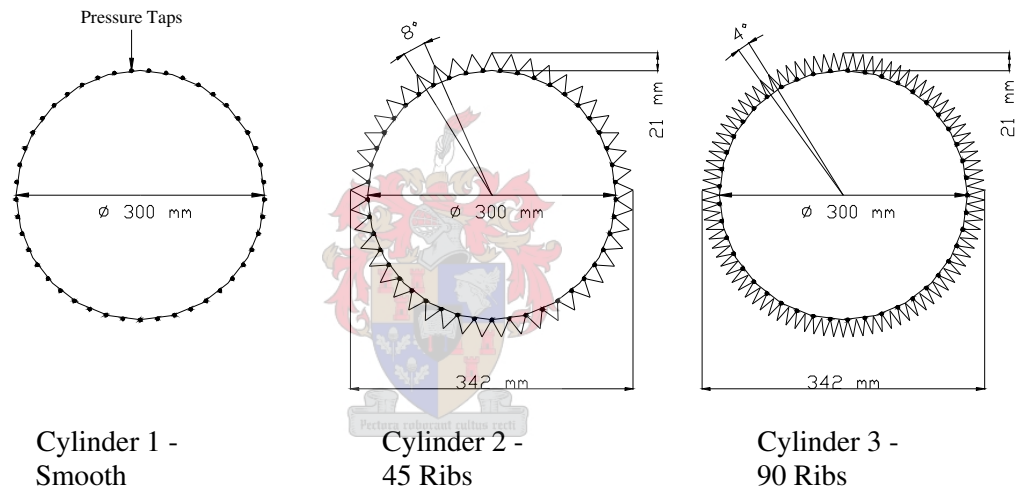


Figure 3.2: Three cylinder models of height 1000 mm used for this test.

3.1.3 Test Setup

The model is secured to the floor of the wind tunnel standing vertically in the centre of the test section. Details and photos of the test setup can be found in Appendix A.

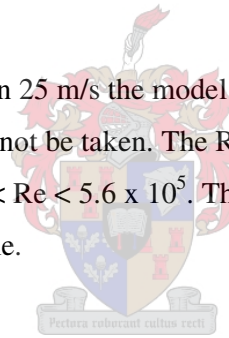
3.1.4 Data Acquisition

All data acquisition is done by means of the computer system connected to the wind tunnel and measurement apparatus. The external pressure distributions are obtained in the form of data files which are then analysed with the help of Matlab. Matlab programs produce both graphs for the external pressure distributions as well as for calculating the drag coefficients.

3.1.5 Limitations

Due to the low rpm needed to produce low wind speeds, wind speeds below 10 m/s are not very stable. This is clearly seen for the data sets for the wind speed equal to 5 m/s. These readings will thus not be considered for analysis.

At wind speeds higher than 25 m/s the model begins to vibrate and accurate pressure readings can thus not be taken. The Reynolds number range that was able to be tested is thus $9.9 \times 10^4 < Re < 5.6 \times 10^5$. This unfortunately does not extend into the transcritical flow regime.



3.2 Results

The results of the experimental work are discussed here. All the results data can be found in Appendix B.

3.2.1 Fluctuations with height along the cylinder

There were three rows of pressure taps on each cylinder at heights of 400 mm, 500 mm and 600 mm from the base. The pressure measurements obtained from these three different heights are now compared.

CYLINDERS WITH 45 AND 90 VERTICAL RIBS:

For all wind speeds, it was found that the pressure distribution on the front of the cylinder was the same for all three heights of pressure taps up to an angle of 60° from the approach angle.

For angles greater than 60° towards the rear of the cylinder, the pressure distributions for the three heights differed slightly. The top row of pressure points (row A) always had a slightly more negative (greater suction) pressure coefficient than that of the middle row (row B). The middle row (row B) once again had a slightly more negative (greater suction) pressure coefficient than that of the bottom row (row C). This is shown in Figure 3.3 for a wind speed of 20m/s. It was found that this order of difference remained the same for all wind speeds.

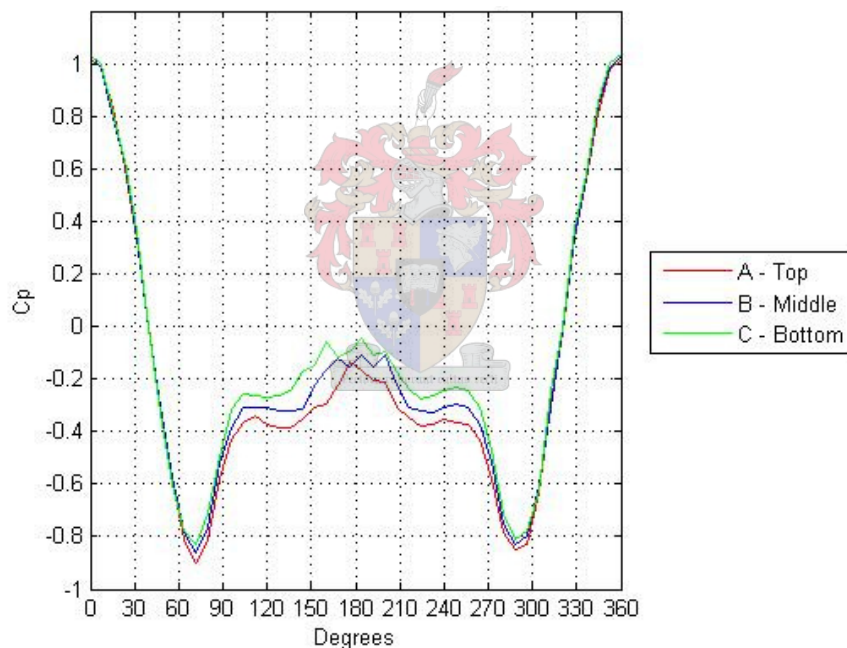


Figure 3.3: The difference in pressure distributions with height for the vertically ribbed cylinders for a velocity of 20m/s.

This phenomenon can be explained as being a result of the 3D flow which occurs due to the model not being an infinitely long cylinder. Both the fact that the floor of the wind tunnel acts as an end plate on the bottom of the cylinder and the fact that a ‘down-flow’ occurs over the top of the chimney contribute to this formation of 3D flow.

SMOOTH CYLINDER:

The smooth cylinder showed similar variation in pressure with gauge height as the vertically ribbed cylinders for wind speeds up to 18 m/s. For wind speeds greater than 18 m/s, the pressure distributions were the same for all three heights around the entire circumference of the cylinder. This is shown in Figure 3.4 and Figure 3.5 respectively.

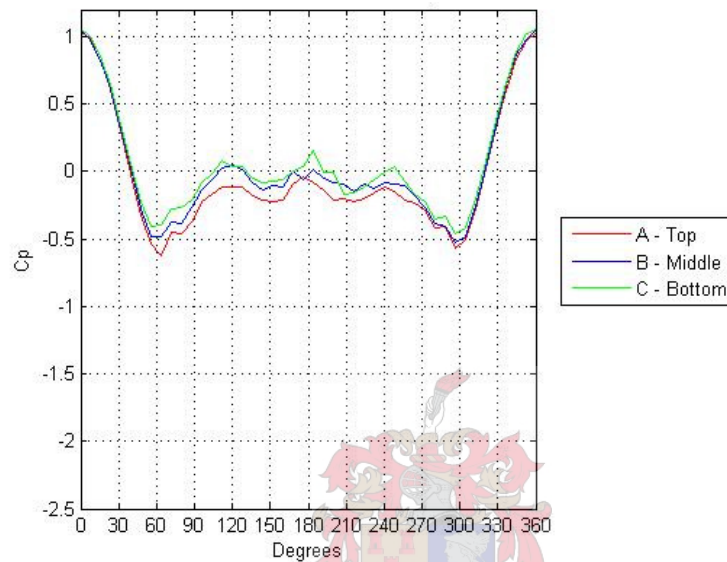


Figure 3.4: The difference in pressure distributions with height for the smooth cylinder for 16m/s.

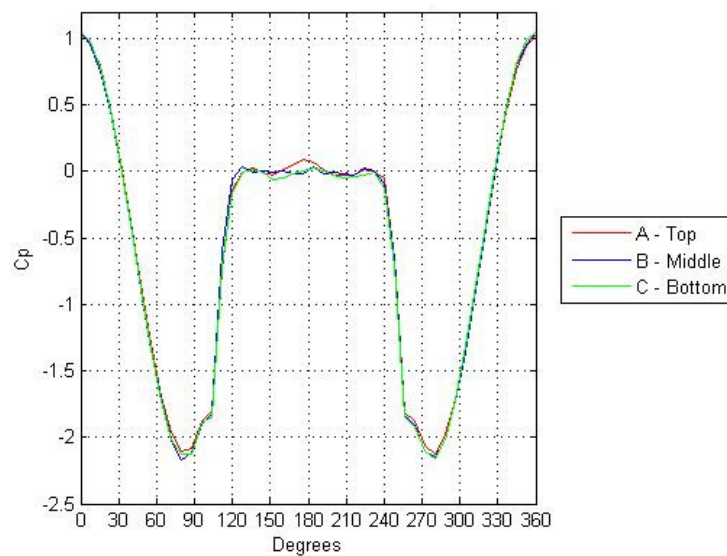


Figure 3.5: The difference in pressure distributions with height for the smooth cylinder for 20m/s.

3.2.2 Effect of varying wind speeds

The effect of varying wind speed (and thus Reynolds number) on the external pressure distribution is now discussed.

CYLINDERS WITH 45 AND 90 VERTICAL RIBS:

The external pressure distribution of both the vertically ribbed cylinders remains constant throughout the variation of wind speeds from 10m/s to 25m/s. This indicates that there is no change in flow regime for the cylinders with vertical ribs.

As mentioned previously, due to the low rpm needed to produce low wind speeds, wind speeds below 10 m/s are not very stable. This is clearly seen for the data sets for the wind speed equal to 5 m/s. These readings will thus not be considered for analysis but are included for verification.

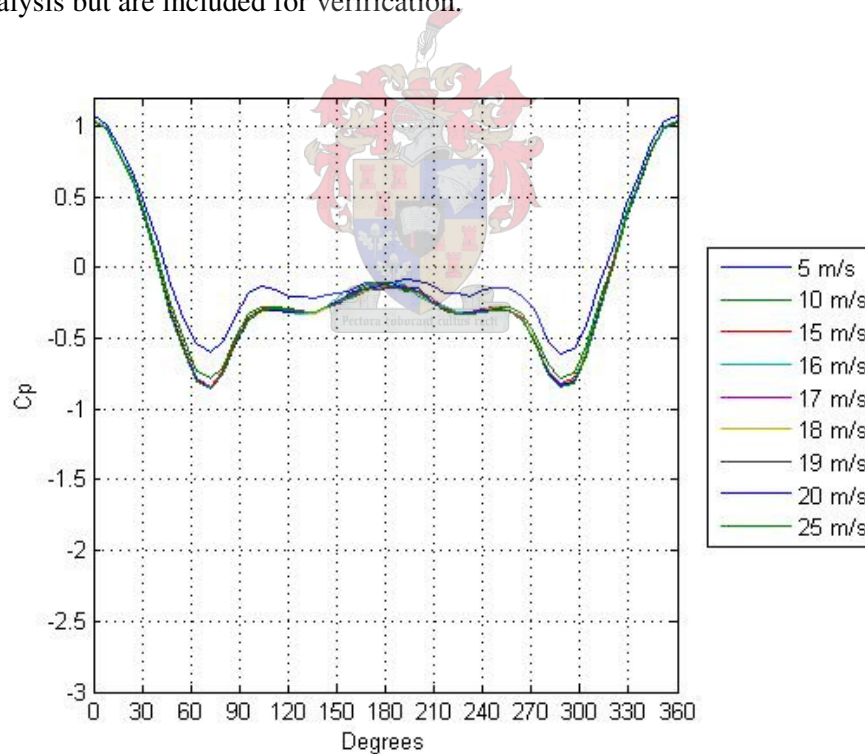


Figure 3.6: External Pressure Coefficients of Cylinder with 45 Vertical Ribs.

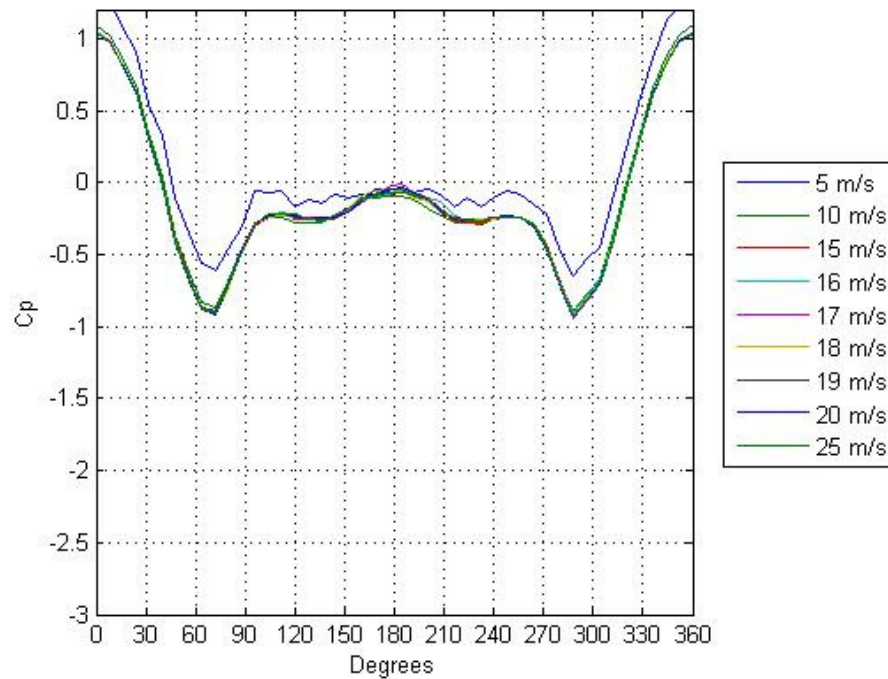
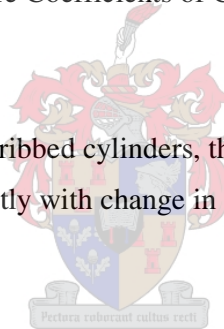


Figure 3.7: External Pressure Coefficients of Cylinder with 90 Vertical Ribs.

SMOOTH CYLINDER:

In contrast to the vertically ribbed cylinders, the external pressure distribution for the smooth cylinder varies greatly with change in wind speed. This can be seen in Figure 3.8.



For wind speeds less than 17m/s (Reynolds numbers less than 3.4×10^5), the external pressure distribution varies very gradually, peaking only to a suction of $C_p = -0.5$ on the sides of the cylinder at an angle of 60° from the approach angle. The distribution is symmetrical about the direction of flow.

For wind speeds of 17m/s and 18m/s (Reynolds numbers 3.4×10^5 and 3.6×10^5), it is found that the external pressure coefficient makes a sudden one sided jump to a suction of $C_p = -2.5$. This jump was observed to occur always on the same side of the cylinder. The cylinder was rotated 180° and the jump was then observed to occur on the opposite side of the cylinder. It can thus be concluded that the jump in pressure coefficient is due to an imperfection in the model.

This observation leads to a very interesting phenomenon of smooth cylinders. At critical Reynolds numbers (in this case $Re = 3.4 \times 10^5$ and 3.6×10^5), the flow

around a smooth cylinder is extremely sensitive to any imperfections. The slightest of imperfections can cause the boundary layer of flow on the one side of the cylinder to trip (thus becoming turbulent) before the other side. This results in an unsymmetrical pressure distribution around the cylinder with a much greater local suction forming on the one side of the cylinder.

Imperfections on a cylindrical tower would no doubt be unavoidable in most methods of construction. This unsymmetrical pressure distribution is thus a significant result which should be considered as influencing the possible failure modes of a cylindrical structure.

For wind speeds greater than 18m/s (Reynolds number greater than 3.6×10^5), the external pressure distribution once again becomes symmetrical. The pressure coefficient peaks at either side of the cylinder to a suction of $C_p = -2.1$ at an angle of 80° from the approach angle. The separation point has thus moved towards the rear of the cylinder as expected. The pressure recovery at the rear of the cylinder has also increased to a pressure coefficient of almost zero.

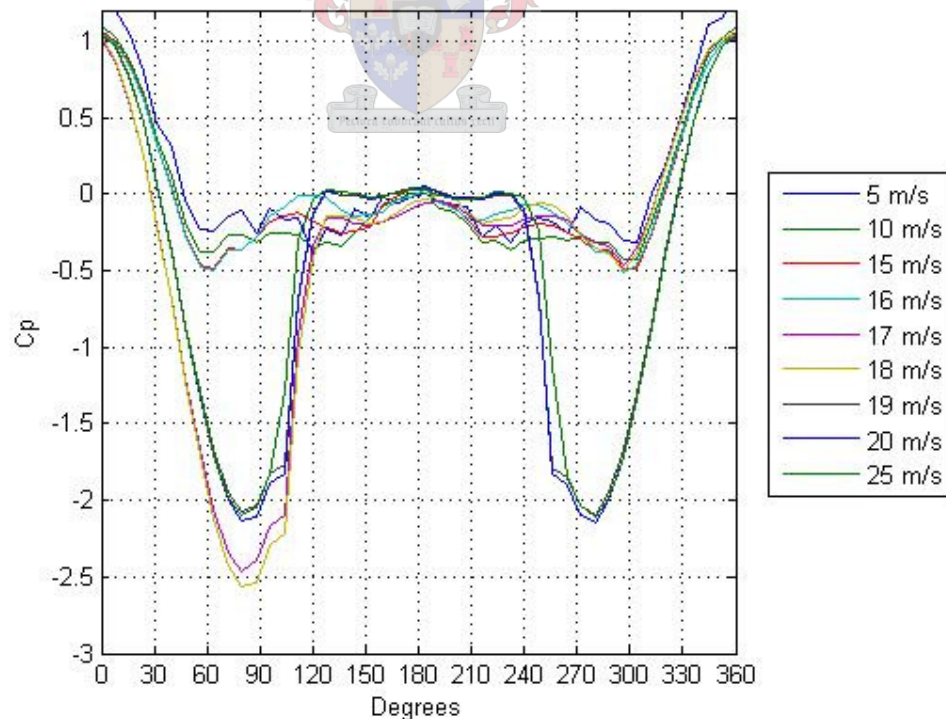


Figure 3.8: External Pressure Coefficients of the Smooth Cylinder.

3.2.3 Conclusion: Smooth vs Vertical Ribs

From the above results for the variation of external pressure distribution around a cylinder with increasing wind speed (and thus Reynolds number), it can be seen that the vertically ribbed cylinders experience a much more stable pressure distribution than the smooth cylinder.

Although the pressure distribution develops suction peaks at lower wind speeds (where these are almost completely absent for the smooth cylinder for wind speeds lower than 17m/s), the pressure distribution remains constant throughout the range of wind speeds.

The vertically ribbed cylinders also always experience a symmetrical pressure distribution. This is not true of the smooth cylinder (with slight imperfections) for wind speeds of 17m/s and 18m/s.

At higher wind speeds, the vertically ribbed cylinders experience less suction on the sides of the cylinder than the smooth cylinder. The pressure coefficient for the vertically ribbed cylinders peaks only to a value of $C_p = -1$ in comparison to the pressure coefficient of the smooth cylinder peaking to a value of $C_p = -2.1$.

3.3 Drag Calculations from Experimental Results

The drag coefficient C_D can be computed (approximately) from the external pressure coefficients around the cylinder. This is done using the experimental external pressure distribution results.

3.3.1 Calculation of Drag Coefficient

The total drag on a body is made up of pressure drag and friction drag. In the case of a smooth cylinder, the friction drag contribution is such a small percentage of the

total drag that it can be considered negligible. The drag on the cylinder can thus be assumed to be only as a result of pressure drag. This pressure drag can be calculated by integrating the external pressure distribution along the entire circumference of the cylinder as follows:

$$C_d = 0.5 \int_0^{2\pi} C_p \cos \theta \, d\theta \quad (3.1)$$

The same formula is applied to the vertically ribbed cylinders. Note that in this case, the computed drag coefficients are only rough indications, due to the positioning of pressure measurements sampling points in the valleys between the ribs and ignoring the rib geometry in the drag computation in equation (3.1). In Chapter 4 drag force measurements on smooth and ribbed models are reported, from which more accurate experimental drag coefficients are computed for ribbed models.

The results of the calculations using Equation 3.1 are shown in Figure 3.9.

3.3.2 Effect of Vertical Ribs on Drag

The drag coefficient for both cylinders with vertical ribs is lower than the drag coefficient for the smooth cylinder below the critical Reynolds number, but higher than that of the smooth cylinder above the critical Reynolds number.

What is very interesting to note, is the drag coefficient for the cylinders with vertical ribs remains almost constant throughout the entire Reynolds number range tested. This indicates that there is no change in flow regime for the cylinders with vertical ribs. The drag coefficient for the cylinder with 45 vertical ribs varies between 0.56 and 0.59 and the drag coefficient for the cylinder with 90 vertical ribs varies between 0.47 and 0.55 for the entire Reynolds number range that was tested.

The impact of the results with regard to the stability of a structure is twofold. Due to the drag coefficient not decreasing at higher Reynolds numbers, the total drag force on such a structure will be greater than the drag force on a smooth cylindrical

structure. The drag coefficient does not vary suddenly and hence removes the cylinder from the critical area (around the critical Reynolds number) of force fluctuations. This is often a great threat to structural stability.

From these calculations, it seems that the cylinder with 90 vertical ribs has a consistently lower drag coefficient. Optimisation studies in this regard would have to be carried out.

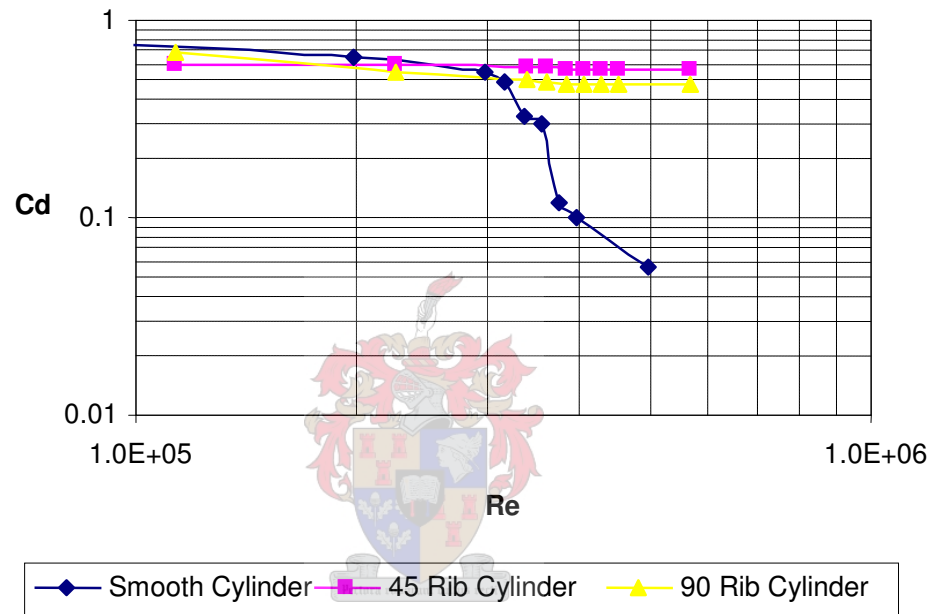


Figure 3.9: Calculated Drag Coefficients for the three Cylinders

3.4 Conclusion

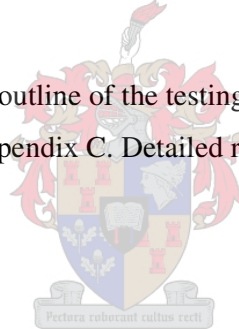
Both cylinders with vertical ribs showed more stable behaviour compared to the smooth cylinder. This can be seen in the constant pressure distribution for varying wind speeds for the vertically ribbed cylinders in comparison to the greatly fluctuating pressure distribution of the smooth cylinder. The drag coefficient for the vertically ribbed cylinders also remained almost constant while that of the smooth cylinder displayed the typical drop and rise in drag coefficient.

4. DRAG COEFFICIENTS – WIND TUNNEL TESTING: UNIVERSITY OF STELLENBOSCH

The aim of the experiment is to investigate the effect of vertical ribs on the pushover force on a circular cylinder. This is to be done by comparing the drag force exerted on a cylinder by means of experimentally measuring the drag coefficient.

4.1 Experimental Setup

This section gives only a brief outline of the testing procedure. For a detailed report of testing methods, please see Appendix C. Detailed results of the tests can be found in Appendix D.



4.1.1 Wind Tunnel Testing Facility

The Wind Tunnel at the Department of Mechanical Engineering of the University of Stellenbosch was used. The wind tunnel is a suction wind tunnel. Wind speeds up to 90 m/s can be generated with reasonable accuracy using the available apparatus. The dimensions of the wind tunnel are given in Table 4.1.

Table 4.1: Dimensions of the Wind Tunnel

Inlet:	Initial Inlet Area	10.600	m ²
	Nozzle Inlet Area	12.300	m ²
Test Section:	Height	1.000	m
	Width	1.425	m
	Length	1.900	m
	Cross Section Area	1.425	m ²
Diffuser:	Length	15.350	m
Fan:	Diameter	2.700	m
	Motor	373	kW

The general layout of the wind tunnel is depicted in Figure 4.1.

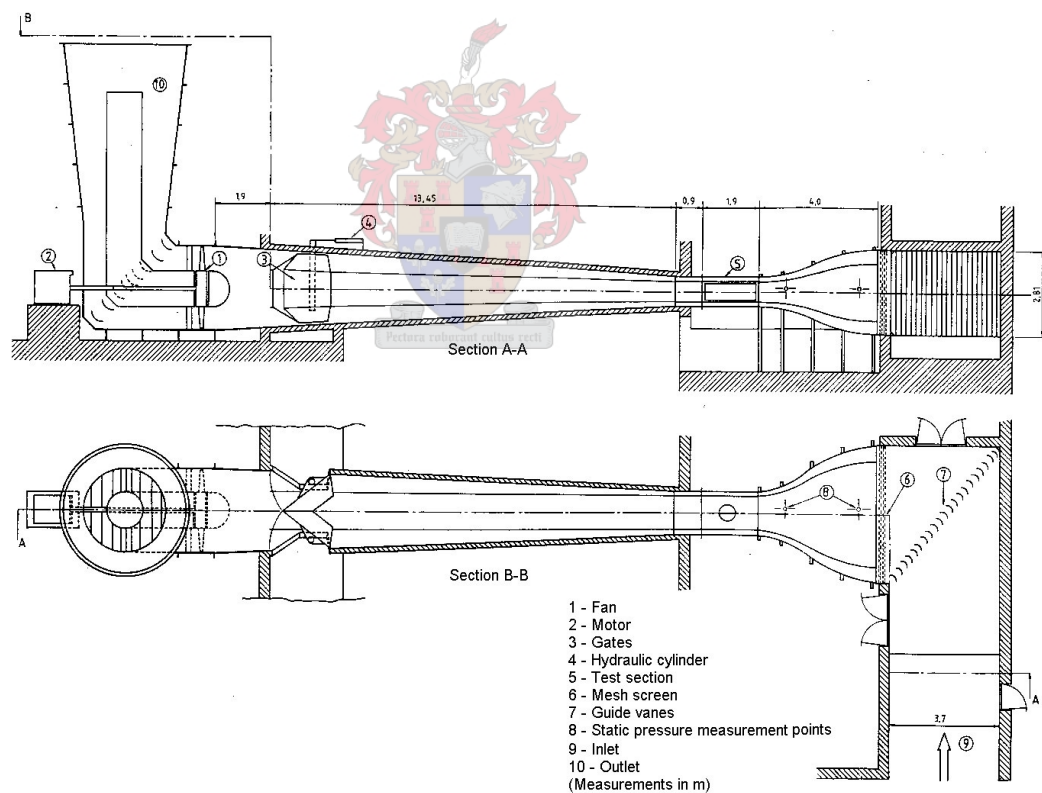


Figure 4.1: General Layout of the Wind Tunnel (Du Buisson, J.J. 1988).

Certain restrictions are placed on the size and position of a model placed in the wind tunnel. These are the 50 mm boundary layer that develops above the test section floor and the blockage area ratio (Largest projected area / Test section area) of 7.5% that may not be exceeded, to avoid a blockage effect.

4.1.2 Models

Three different chimney models were used. All models were 285 mm in length (high). 110 mm diameter PVC pipe was used for all three models. Corrugated aluminium sheeting was wrapped around two of the models in order to create vertical ribs. The sizes of the vertical ribs were in part influenced by the feasibility of model construction.

The first model was that of a smooth circular cylinder with outer diameter of 110 mm. The aspect ratio ($AR = \text{height} / \text{diameter}$) of the smooth cylinder was $285 / 110 = 2.59$.

The second model was that of a cylinder with 47 small vertical ribs. The ribs extended 5 mm from the PVC pipe, making the cylinder's outer diameter 120 mm. This gave an l/d ratio (where $l = \text{depth of vertical rib}$ and $d = \text{diameter of cylinder}$) of $5 / 110 = 0.045$.

The third model was that of a cylinder with 23 large vertical ribs. The ribs extended 10 mm from the PVC pipe, making the cylinder's outer diameter 130 mm. This gave an l/d ratio (where $l = \text{depth of vertical rib}$ and $d = \text{diameter of cylinder}$) of $10 / 110 = 0.09$.

The three models are shown schematically in Figure 4.2.

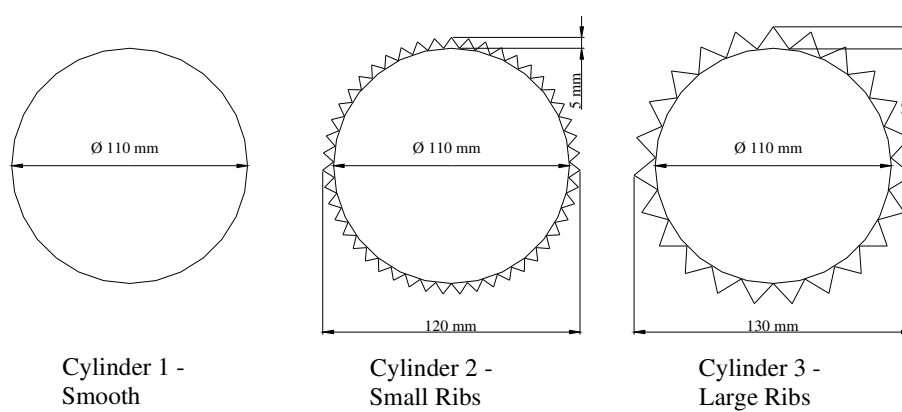


Figure 4.2: Three cylinder models of height 285 mm used for this test.

4.1.3 Test Setup

The model is attached to a one directional load cell balance. The load cell balance is designed so as to read the total drag force exerted on the cylinder in the horizontal direction. Details of how the load cell balance operates can be found in Appendix C.

4.1.4 Data Acquisition

The mV/V reading from the load cell is fed through a Spider 8 data acquisition apparatus to a Computer. The computer program Catman 4.5 is used to convert this mV reading into a force (N) reading. This force (F_d) reading is then used to calculate the respective drag coefficient (C_d).

$$C_d = F_d / (0.5 \times \rho \times v^2 \times A) \quad (4.1)$$

Where ρ = density of air
 v = wind speed
 A = frontal area of cylinder

4.1.5 Limitations

At wind speeds lower than 10 m/s, the doors of the wind tunnel are unstable. Thus any data obtained at wind speeds lower than 10 m/s is included only to verify this fact.

The Reynolds number range that could be tested is $7.5 \times 10^4 < Re < 6.5 \times 10^5$. This unfortunately does not extend into the transcritical flow regime.

4.2 Results: Smooth Cylinder

4.2.1 The Influence of Aspect Ratio

The aspect ratio of a smooth cylindrical cylinder is defined as the height of the cylinder over the diameter. The smooth cylinder that was tested thus has an aspect ratio of $285 / 110 = 2.59$.

This aspect ratio is used to characterise cylinders of finite length (height). Flow around such finite cylinders behaves differently to flow around an infinitely long circular cylinder. There are many differences in these flow patterns, but the most visible and significant is the 'downflow' which can be observed in the top section of the wake behind the cylinder.

The complexity of flow around a finite cylinder is a study subject of its own, which does not fall within the scope of this study. It should however be noted that due to this phenomenon, the drag coefficient for finite smooth circular cylinders differs from that of an infinitely long smooth circular cylinder. The drag coefficient for finite smooth circular cylinders, particularly with aspect ratios less than 3, has been noted to be lower than that of an infinite smooth circular cylinder (Summer et al 2004).

The behaviour of the drag coefficient of an infinitely long smooth circular cylinder is well known and has been included in this text as Figure 4.3 for reference purpose.

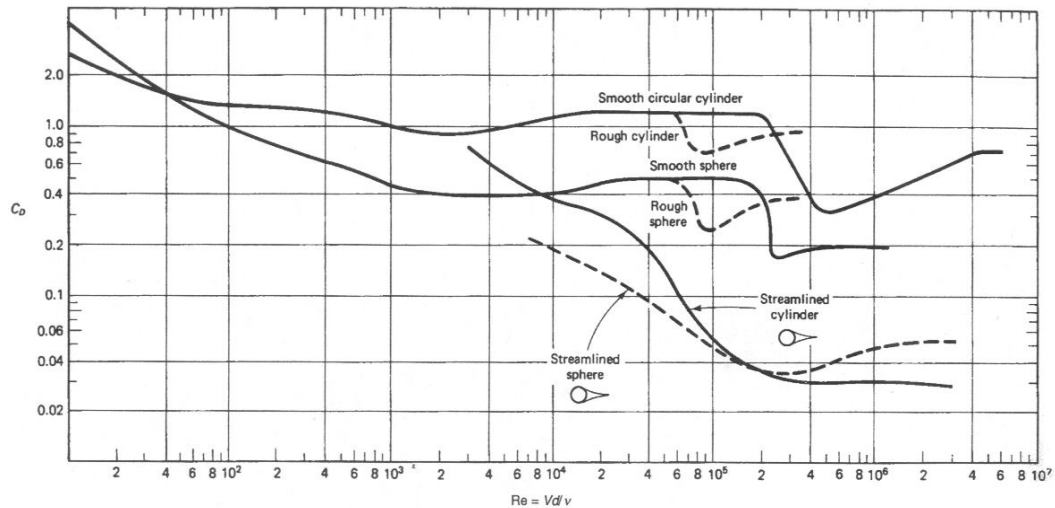
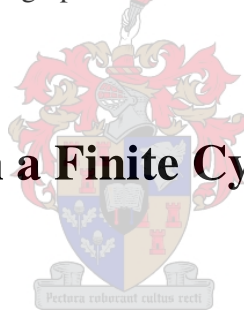


Figure 4.3: Drag Coefficient graph for flow around a Cylinder. (Potter and Wiggert, 2002)

4.2.2 Drag on a Finite Cylinder of Aspect Ratio 2.59



The drag coefficients for the smooth cylinder of aspect ratio 2.59 are computed from the total drag forces measured in this research and are shown as a function of Reynolds number in Figure 4.4. As expected, the drag coefficient for the test cylinder is consistently lower than that of the infinite cylinder from literature. The shape of the curve is also very typical where the drag coefficient is initially at a constant high value before dropping suddenly and then increasing again gradually to a value less than the initial high value.

The drop in drag coefficient occurs earlier than expected with the lowest drag coefficient of approximately 0.4 occurring at $Re = 3.2 \times 10^5$. The point at which this sudden drop in drag coefficient is observed is known as the critical Reynolds number and is in the region of $Re = 5 \times 10^5$ for an infinite, smooth circular cylinder in uniform flow. As observed in Figure 4.3, the critical Reynolds number is reduced

with increased surface roughness. So, the explanation of this difference in critical Reynolds number may be due to small imperfections on the model which give the cylinder a slight uneven roughness which would result in a lower critical Reynolds number.

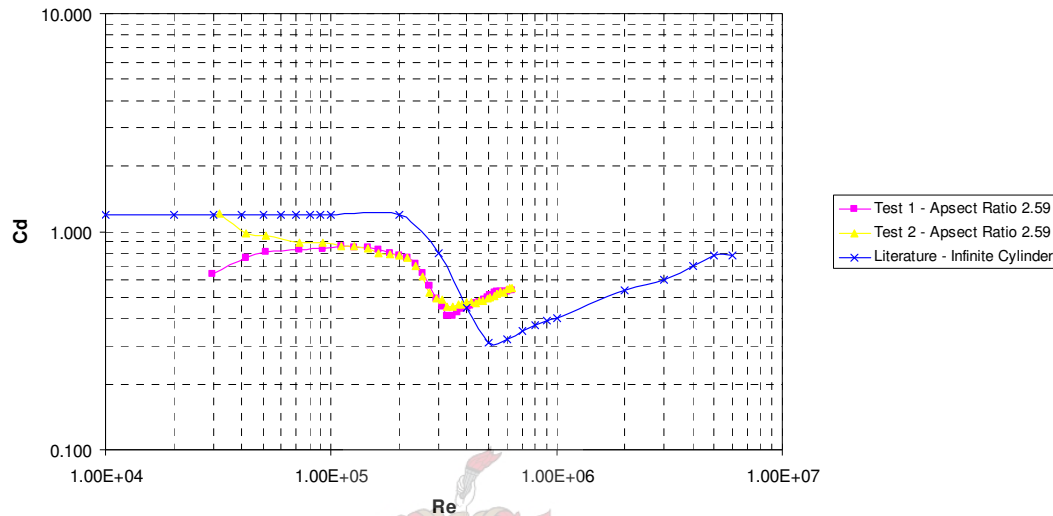


Figure 4.4: Drag Coefficient graph for Test Cylinder 1, Smooth.

4.3 Results: Cylinder with Small vertical Ribs

The drag coefficients for the cylinder with small vertical ribs are computed from the total drag forces measured in this research and are shown as a function of Reynolds number in Figure 4.5. The drag coefficient for the cylinder with small vertical ribs is lower than the drag coefficient for the smooth cylinder below the critical Reynolds number, but higher than that of the smooth cylinder above the critical Reynolds number.

What is very interesting to note however, is the fact that the drag coefficient for the cylinder with small vertical ribs remains almost constant throughout the entire Reynolds number range tested. This indicates that there is no change in flow regime for the cylinder with small vertical ribs. The drag coefficient varies between 0.7 and 0.8 for the entire Reynolds number range tested.

In comparison to the results of the cylinder with larger vertical ribs, the smaller ribbed cylinder has a drag coefficient of approximately 0.1 less than that of the larger ribbed cylinder. The characteristic of a drag coefficient which remains constant is shared.

As argued for the vertically ribbed models discussed in Chapter 3, the impact of the results with regard to the stability of a structure is twofold. Due to the drag coefficient not decreasing at higher Reynolds numbers, the total drag force on such a structure will be greater than on a smooth cylindrical structure. The drag coefficient does not vary suddenly and hence removes the cylinder from the critical area (around the critical Reynolds number) of force fluctuations. This is often a great threat to structural stability.

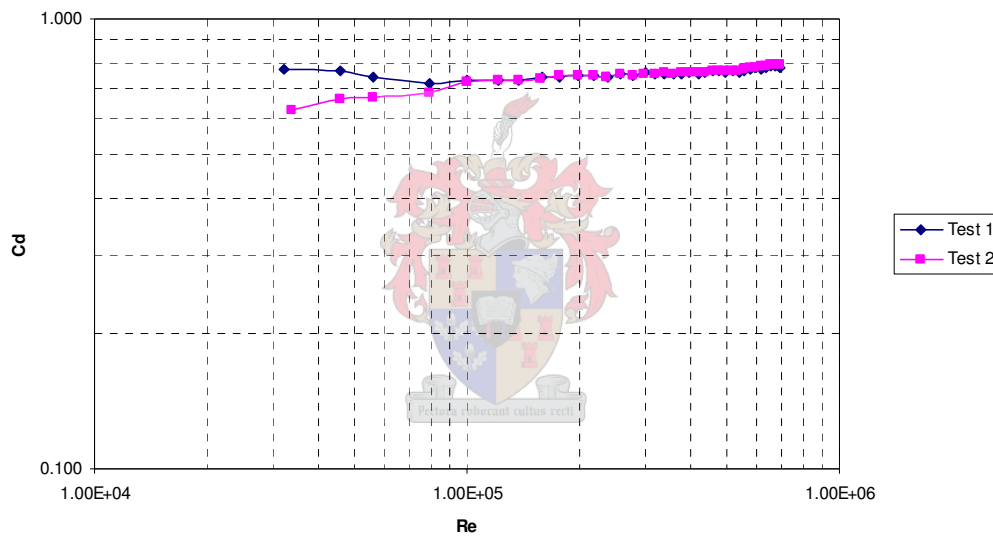


Figure 4.5: Drag Coefficient graph for Test Cylinder 2, Small Vertical Ribs.

4.4 Results: Cylinder with Large vertical Ribs

The drag coefficients for the cylinder with large vertical ribs are computed from the total drag forces measured in this research and are shown as a function of Reynolds number in Figure 4.6. The drag coefficient for the cylinder with large vertical ribs is lower than the drag coefficient for the smooth cylinder below the critical Reynolds number, but higher than that of the smooth cylinder above the critical Reynolds number.

What is very interesting to note, however, is the fact that the drag coefficient for the cylinder with large vertical ribs remains almost constant throughout the entire Reynolds number range tested. This indicates that there is no change in flow regime for the cylinder with large vertical ribs. The drag coefficient varies between 0.8 and 0.9 for the entire Reynolds number range tested.

The larger ribbed cylinder has a drag coefficient of approximately 0.1 greater than that of the smaller ribbed cylinder. The characteristic of a drag coefficient which remains constant is shared. An optimisation study on the rib size is recommended.

As discussed in section 4.3, the impact of these results with regard to the stability of a structure is twofold.

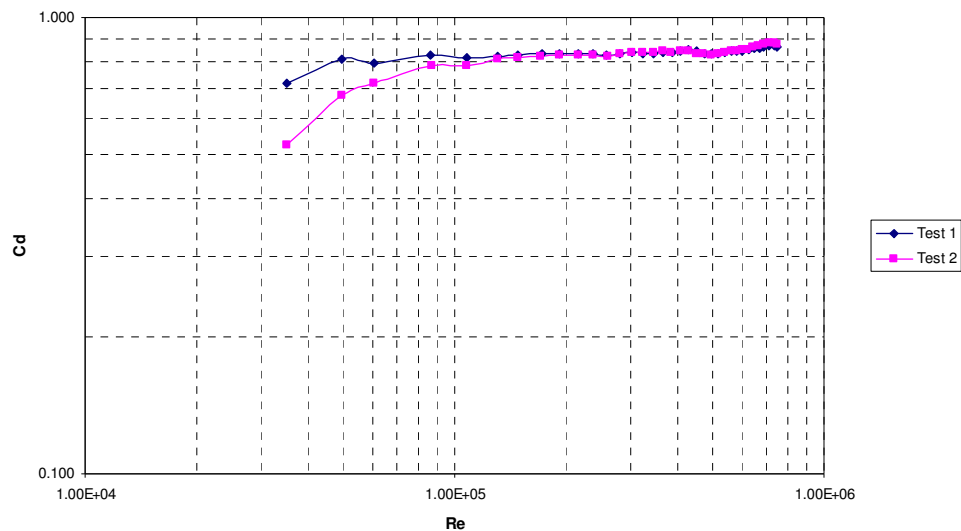


Figure 4.6: Drag Coefficient graph for Test Cylinder 3, Large Vertical Ribs.

4.5 Conclusions

The impact of the above results with regard to the stability of a structure is twofold. Due to the drag coefficient not decreasing at higher Reynolds numbers, the total drag force on such a structure will be greater than on a smooth cylindrical structure. The drag coefficient does not vary suddenly and hence removes the cylinder from the critical area (around the critical Reynolds number) of force fluctuations. This is often a great threat to structural stability.

The effect of these two impacts will need to be studied in greater detail in order to validate the structural use of such vertical ribs. From these tests it can be seen that the smaller vertical rib would appear to be more favourable than the larger vertical rib. An optimisation study on the rib size is recommended.



5. COMPUTATIONAL FLUID DYNAMICS

Computational Fluid Dynamics (CFD) is used to model flow around a smooth cylinder and vertically ribbed cylinders. The experimental results serve to validate the numerical result. The analysis is then extended to obtain results for those conditions which could not be tested experimentally. The FLUENT (2004) Release 6.2.16 software program together with the supplied documentation was used for the CFD analysis.

5.1 Introduction and Input Parameters

GAMBIT (2004) Release 2.3.16 was used as a pre-processor to generate the model and mesh the flow field around the cylinder in two dimensions. The cylinder models were created 300 mm in diameter and the test section was modelled as 6 m wide by 10 m long. Three models were created: a smooth cylinder as well as cylinders with 45 and 90 vertical ribs, simulating the physical models used in wind tunnel tests described in Chapter 3.1.2. The cylinders were placed as shown in Figure 5.1. The distance from the wind tunnel walls allow conditions of free flow to be simulated and the wake area is long enough to allow full wake development.

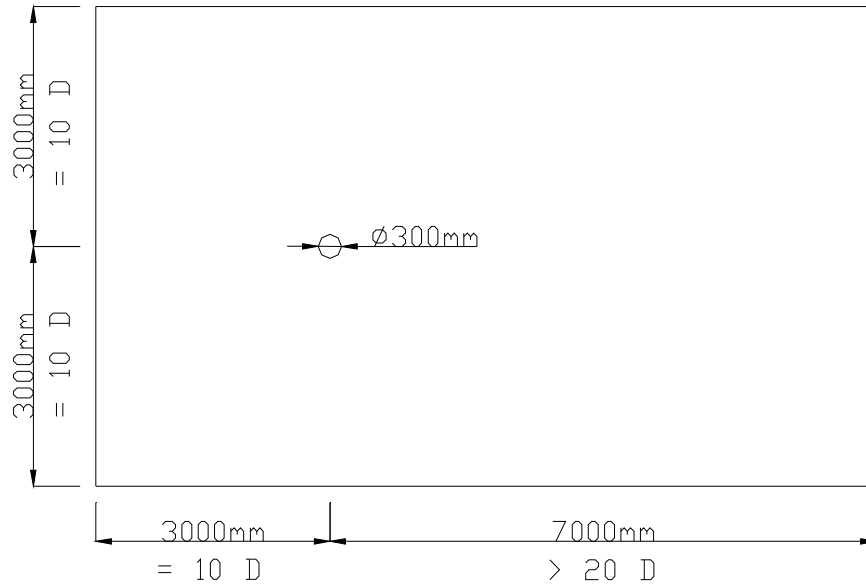
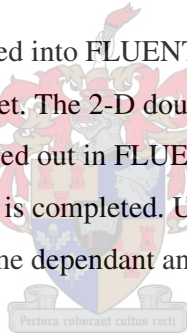


Figure 5.1: The cylinder model and air flow domain as created in GAMBIT.

The meshed models were imported into FLUENT where the physical properties and initial conditions for testing are set. The 2-D double precision solver was used. The steady state CFD analysis is carried out in FLUENT until convergence is obtained and the required number of iterations is completed. Unsteady (transient) state analyses are also performed so as to obtain time dependant animations.



5.1.1 GAMBIT – The Meshed Models

Refinement of the meshing close to the cylinder wall and in the wake region was ensured by means of sizing functions. The starting cell size was 1 mm with a growth rate of 1.1 to a maximum cell size of 100 mm. A combination of the Quad map and Quad Pave meshing schemes was used. The mesh fineness was also checked by means of FLUENT's Yplus value once the mesh was imported to FLUENT. The Yplus value controls the acceptable distance between the cell centroid and the wall for wall-adjacent cells.

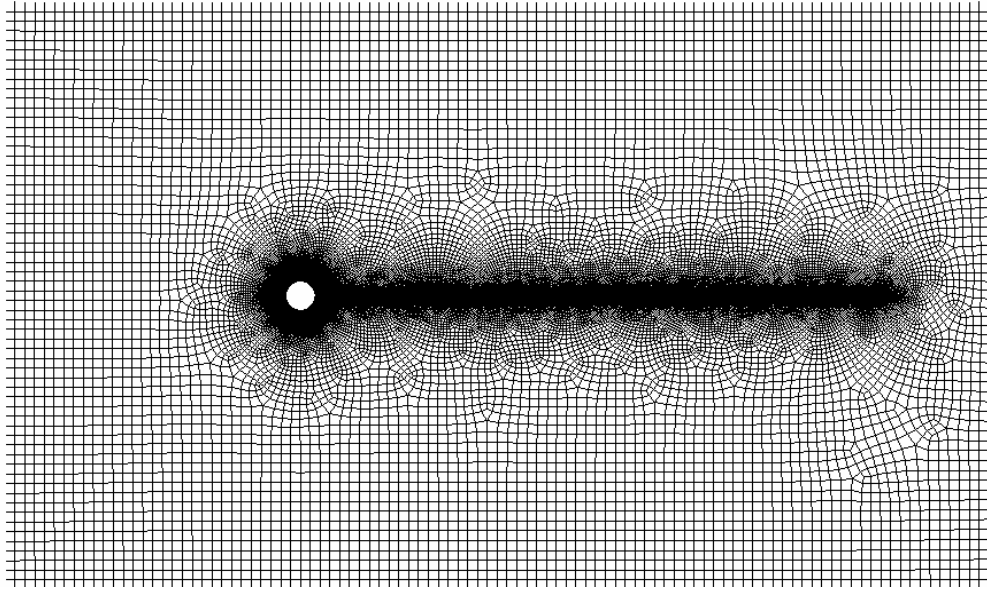


Figure 5.2: The meshed flow domain for the smooth cylinder.

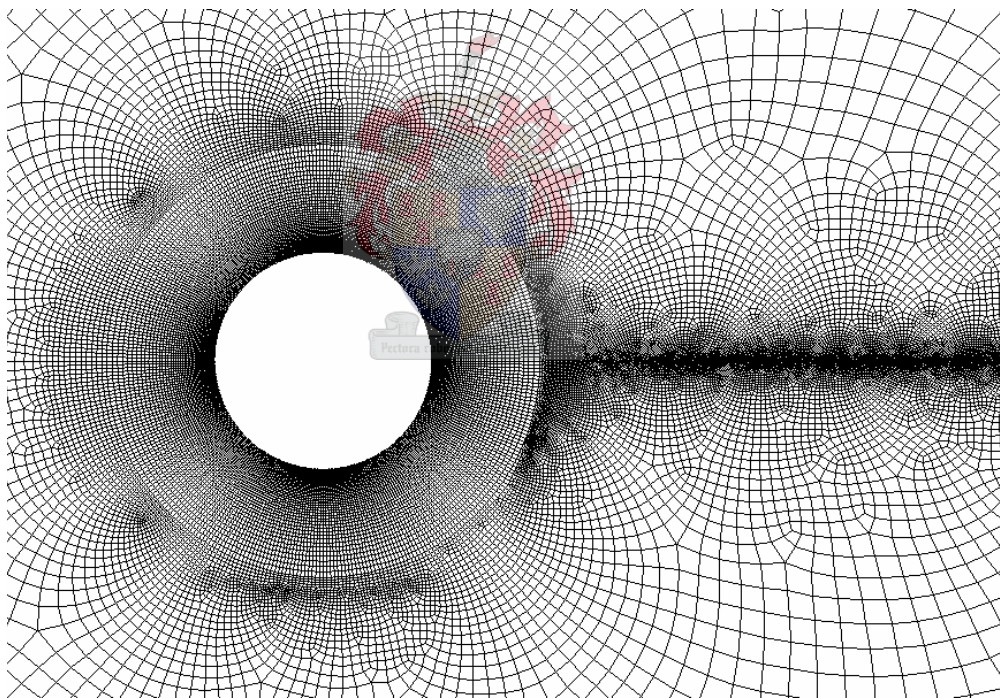


Figure 5.3: The meshed flow domain for the smooth cylinder zoomed.

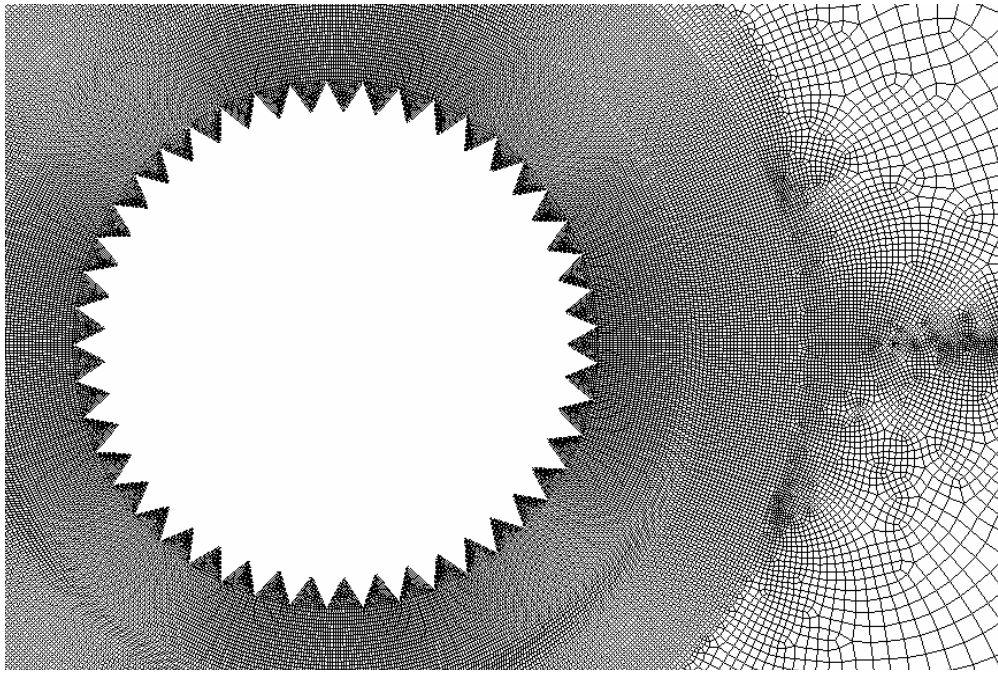


Figure 5.4: The meshed flow domain for the cylinder with 45 vertical ribs zoomed.

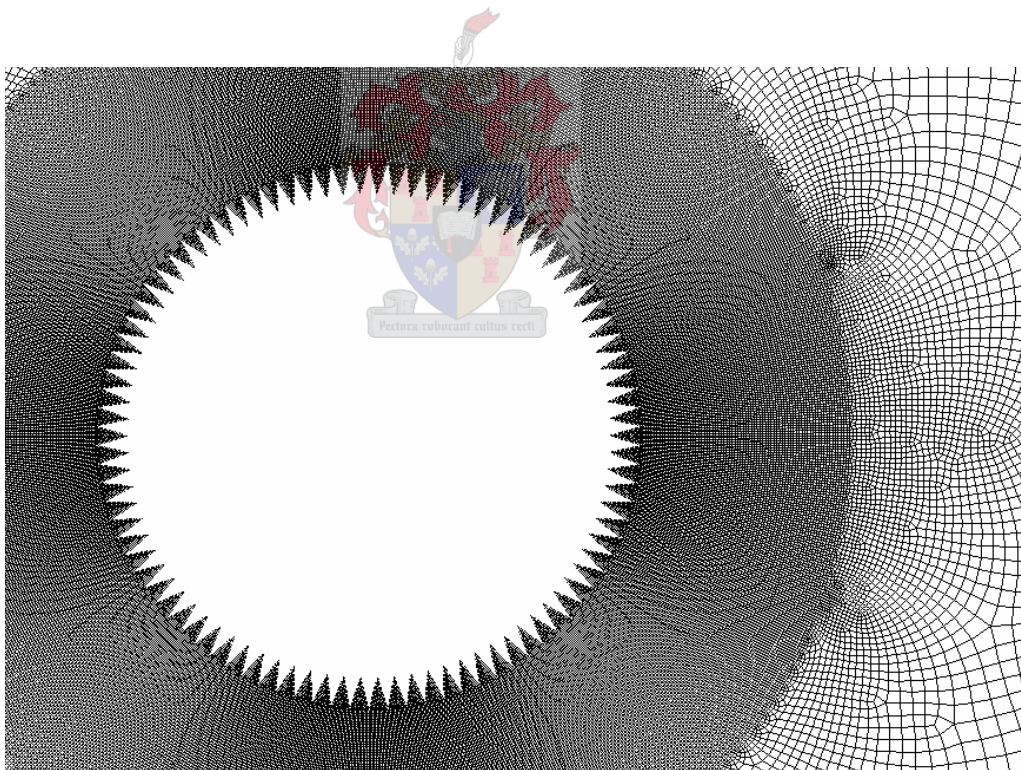


Figure 5.5: The meshed flow domain for the cylinder with 90 vertical ribs zoomed.

The various zones are also defined in GAMBIT. The wind tunnel walls and the cylinder model are set as “Wall”. The wind tunnel inlet is set as “Pressure Inlet” and the wind tunnel outlet is set as “Pressure Outlet”. It was decided to make use of the

pressure inlet and outlet rather than the velocity inlet and outlet. Thus, a constant pressure is defined for the inlet and outlet. This is a better representation of the velocity profile which develops in an experimental wind tunnel setup.

The FLUENT 5/6 solver was selected in GAMBIT and the mesh was then exported as a 2-D mesh to be imported by FLUENT.

5.1.2 FLUENT - Conditions

Both steady state and unsteady state CFD analyses were run in order to obtain the appropriate results. The segregated 2-D double precision solver was used together with the Spalart-Allmaras viscous model. The Spalart-Allmaras turbulence model was chosen according to the FLUENT users guide as this model is best for external flow at high Reynolds numbers and has near wall boundary layer treatment.

The physical properties of air such as density (1.225 kg/m^3) and viscosity ($\mu = 1.7894 \times 10^{-5} \text{ kg/m-s}$) are defined as the default interior material. Operating conditions are those of atmospheric pressure (101,325 kPa). The inlet boundary condition is set as a pressure inlet by defining the total gauge pressure which is representative of the free flow velocity. This varied according to the simulated Reynolds number, for instance 245 Pa is the inlet pressure for an inlet free flow velocity of 20 m/s, coinciding with a Reynolds number of $\text{Re} = 3.97 \times 10^5$. The turbulence is defined by means of turbulence intensity and hydraulic diameter. The outlet boundary condition is set as a pressure outlet and defined similarly.

For the Steady State Solution, the flow and modified turbulent viscosity equations are solved by means of the “SIMPLE” (Semi-Implicit Method for Pressure Linked Equations) algorithm for pressure-velocity coupling. The discretization of pressure is set to “PRESTO!” (Pressure Staggering Option), while the momentum and modified turbulent viscosity discretization are set to “Second Order Upwind”.

For the Unsteady State Solution, the flow and modified turbulent viscosity equations are solved by means of the “PISO” (Pressure Implicit with Splitting of Operators)

algorithm for pressure-velocity coupling. The discretization of pressure is set to “PRESTO!” (Pressure Staggering Option), while the momentum and modified turbulent viscosity discretization are set to “Second Order Upwind”. The time step size for the Unsteady State Solution was set to the recommended value of the average cell size divided by the flow speed.

The solution is initialized by the initial values being computed from the wind tunnel inlet. The residuals of the differential equations are monitored and the convergence tolerance for all residuals is set as 10^{-4} . The drag force on the cylinder model is also monitored. The reference values are computed from the wind tunnel inlet. The area and length for the calculation of the drag coefficient are both set to the cylinder diameter.

The case and data files are stored and the analysis runs until convergence has occurred and the necessary number of iterations has been performed. The accuracy of the solution with regard to mesh refinement and turbulence model are checked. The solution is also checked by means of known values of the drag coefficient from literature.

5.1.3 Limitations

The Spalart-Allmaras model is not able to predict correct flow behaviour for all Reynolds numbers. The CFD analysis was thus only performed for Reynolds numbers between 10^5 and 10^6 . It is also not possible to predict transcritical flow behaviour with the currently available turbulence models.

Due to time constraints, not all analyses could be run in the Unsteady State in order to investigate vortex shedding in greater detail. This may be done in a later study.

5.2 Drag on a Smooth Cylinder

Drag on a smooth cylinder is a well known area of study. The drag coefficient graph for a smooth cylinder is widely reported in literature and an example is shown in Chapter 4, Figure 4.3.

This drag coefficient graph is however not an accurate guide for the real world as it is a representation of ideal flow conditions. The result of this idealization will be discussed below.

5.2.1 Theoretical Conditions

The conditions for which the well known drag coefficient graph from literature is applicable are not those conditions which a real life structure would be exposed to.

Theoretical conditions relate to ideal flow with zero turbulence. The cylinder is flawlessly smooth and of infinite length such that flow around the cylinder is entirely two dimensional. The differences between these conditions and those in real life are shown in Figure 5.6.

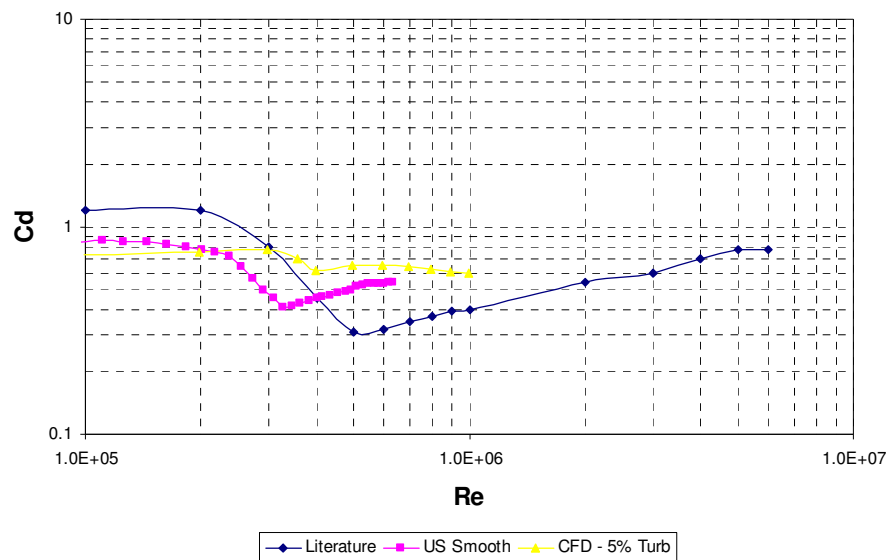


Figure 5.6: Drag Coefficient comparison between Literature and Real Life.

5.2.2 Real Life Conditions

A cylindrical structure exposed to wind conditions will not experience the ideal theoretical conditions described above. Firstly, the air flow around the structure will contain a varying percentage of turbulence. It is also not practical to construct a perfectly smooth cylindrical structure. The structure would thus have a slight roughness and possibly small imperfections. The cylindrical structure will experience three dimensional flow effects due to its aspect ratio (discussed in Chapter 4.2.1).

For this reason, the model of a smooth cylinder was analysed in FLUENT with 5% turbulence intensity. The model is still considered to be perfectly smooth and only 2-D flow is considered. The results of the CFD analysis can be seen in Figure 5.6. In Figure 5.7 they are compared with the results of the drag tests performed at the University of Stellenbosch as well as the numerically calculated drag from the pressure distribution experiments in Japan.

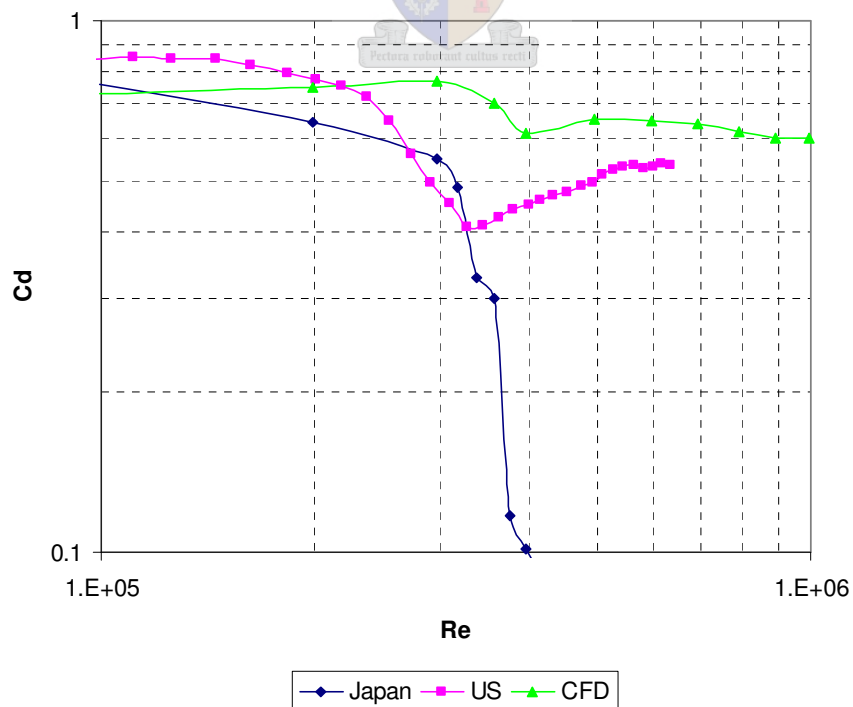


Figure 5.7: Comparison of Drag coefficients

Although the above drag coefficient graphs do not coincide completely, they all reach their minimum point between 3×10^5 and 4×10^5 . This drop in drag coefficient occurs at lower Reynolds number than the theoretical curve which has its minimum at 5×10^5 .

The numerically calculated drag coefficient from the Japan experiments gives a good indication of where the minimum drag coefficient occurs, but can not be considered to be exact.

The experimentally determined drag coefficient from the US wind tunnel tests represents the real drag which the cylinder experiences. The drop in drag coefficient occurs earlier than the theoretical drag (see Figure 5.6) due to the aspect ratio of the cylinder, slight imperfections of roughness on the model and turbulence in the air flow.

The CFD simulation is able to model the turbulence in the air, which moves the drop in drag coefficient to a lower Reynolds number than that of theoretical flow. It does not however take into account aspect ratio or model imperfections. The minimum drag coefficient is thus observed at a slightly higher Reynolds number than that of the experimental data.

What this section aims to show is that there is no single drag coefficient graph which can be applied to a cylindrical structure in real life. Varying conditions over which there may be no control – such as wind turbulence and construction imperfections – result in different drag coefficient graphs for each situation.

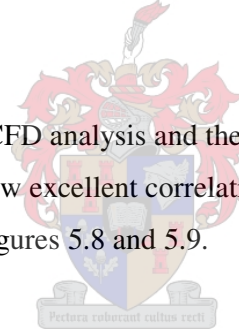
What is known is the general shape of the drag coefficient graph. It will drop to a minimum and then increase again to a steady value slightly less than before the drop. The Reynolds number at which this drop in drag coefficient occurs, as well as the amount by which it drops, can not be determined exactly.

5.3 Drag on vertically Ribbed Cylinders

CFD analysis for vertically ribbed cylinders was performed on two cylinder models with 45 and 90 vertical ribs respectively. The same conditions as in the Japan wind tunnel tests were simulated.

Once again it should be noted that the numerically calculated drag coefficient for the Japan wind tunnel tests are only an approximation. This is due to the integration method for a smooth cylinder being applied to a vertically ribbed cylinder as well as the fact that the external pressure measurement points were all between the vertical ribs on the cylinder surface. The numerical approximation method does however give a correct comparison between the vertically ribbed cylinders showing the cylinder with 90 vertical ribs to have a lower drag coefficient than that of the cylinder with 45 vertical ribs.

The comparison between the CFD analysis and the drag tests performed at the University of Stellenbosch show excellent correlation for both the vertically ribbed models. This can be seen in Figures 5.8 and 5.9.



It should once again be pointed out that the drag coefficient of the vertically ribbed cylinders remains constant with varying wind speeds (and thus varying Reynolds number). An extra point at $Re = 2 \times 10^6$ was also analysed by CFD and the drag coefficient still remained constant at this Reynolds number. This favourable outcome differs from the drag coefficient graph of a smooth cylinder which displays a drop and rise in drag coefficient with varying Reynolds number.

The CFD results show that the cylinder with 90 vertical ribs has a lower drag coefficient of 0.79 than the cylinder with 45 vertical ribs which has a drag coefficient of 0.88. This is consistent with the University of Stellenbosch experimental results.

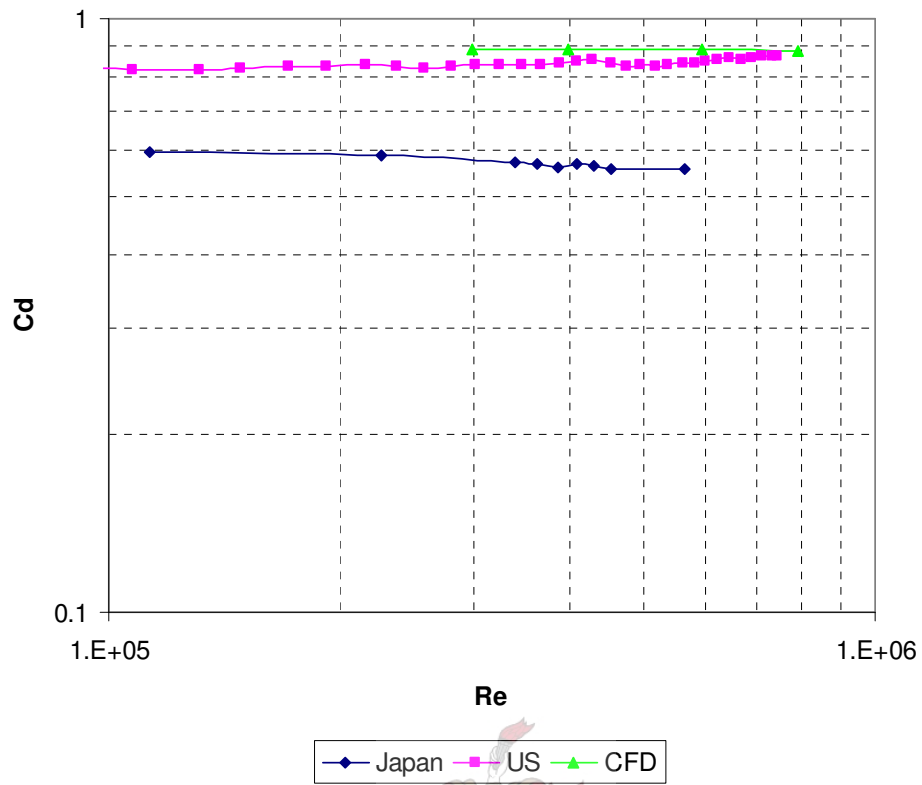


Figure 5.8: Drag Coefficient graph for Cylinder with 45 Vertical Ribs.

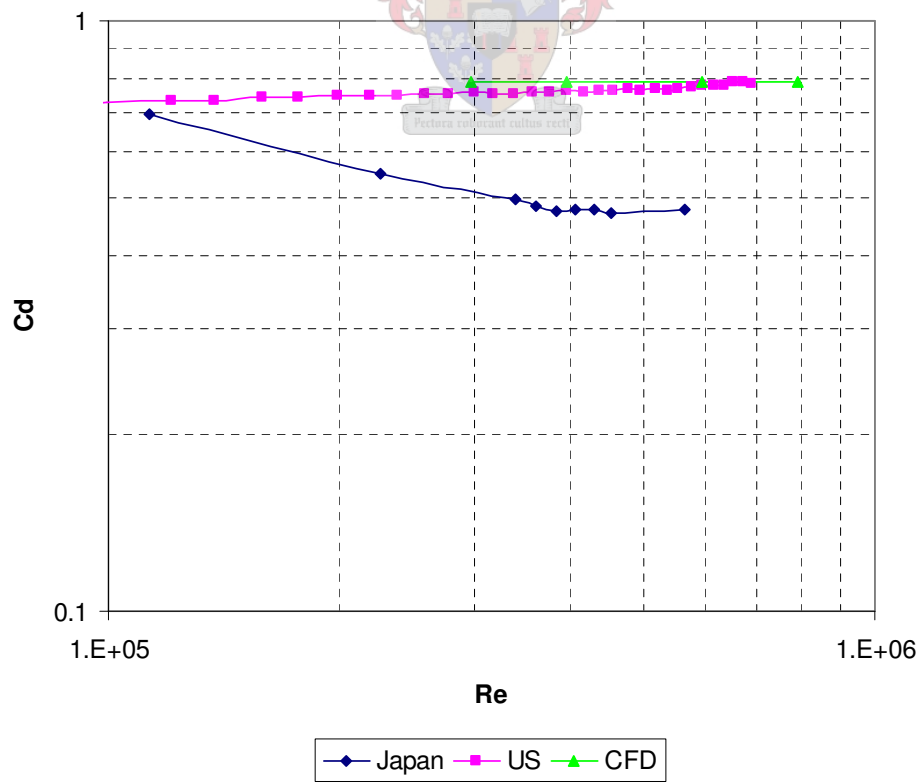


Figure 5.9: Drag Coefficient graph for Cylinder with 90 Vertical Ribs.

5.4 External Pressure Distributions

The external pressure coefficients obtained from the CFD analysis correlate well with the experimental external pressure coefficients from the Japan wind tunnel testing. Thus, the result from the wind tunnel testing in Japan regarding the effect of vertical ribs on external pressure coefficients is confirmed here by CFD analysis. This is shown in Figure 5.10 and 5.11. The difference in drag coefficient at the back of the cylinder is due to the effects of three-dimensional flow, and thus aspect ratio, not being accounted for in the two-dimensional CFD analysis.

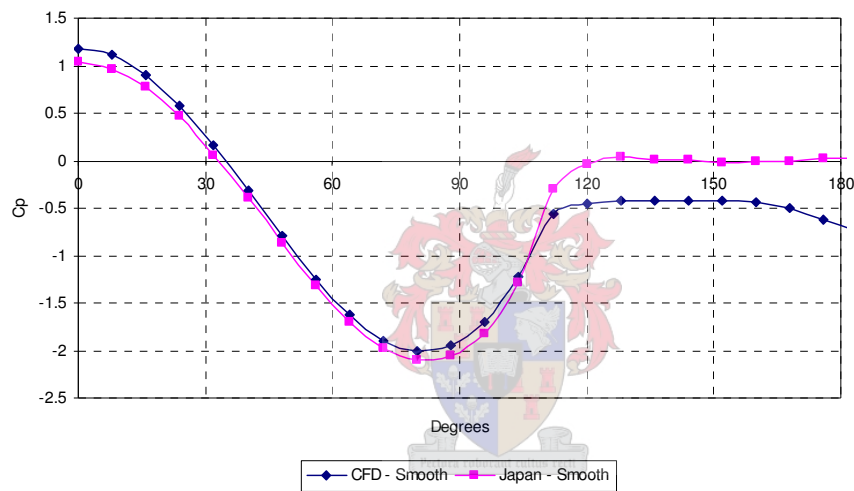


Figure 5.10: External Pressure Coefficients for the Smooth Cylinder for 30m/s.

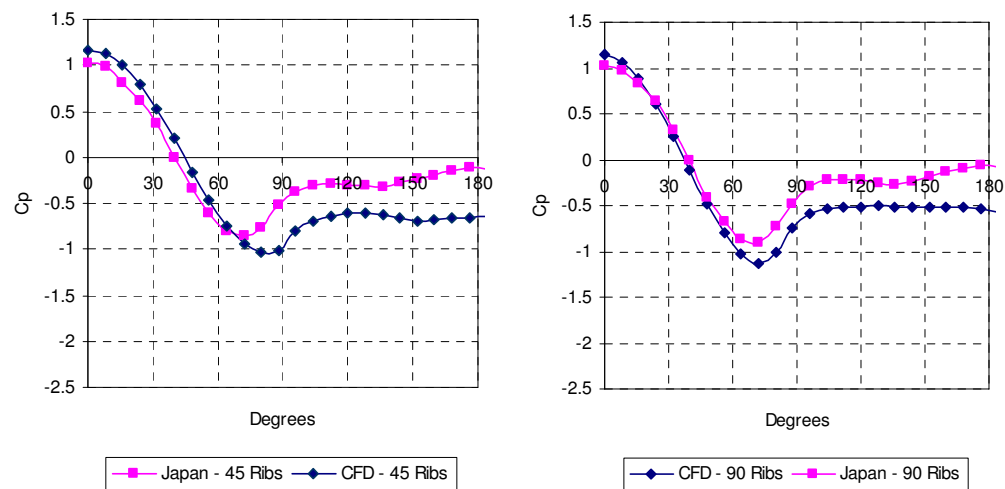


Figure 5.11: External Pressure Coefficients for the Ribbed Cylinders for 30m/s.

The measured pressure coefficients from Japan were determined only at the cylinder wall between the vertical ribs. The CFD analysis however, gives the pressure distribution along the entire length of the rib. FLUENT plots this as the drag coefficient against the “curve length” as shown in Figure 5.12 by the black graph.

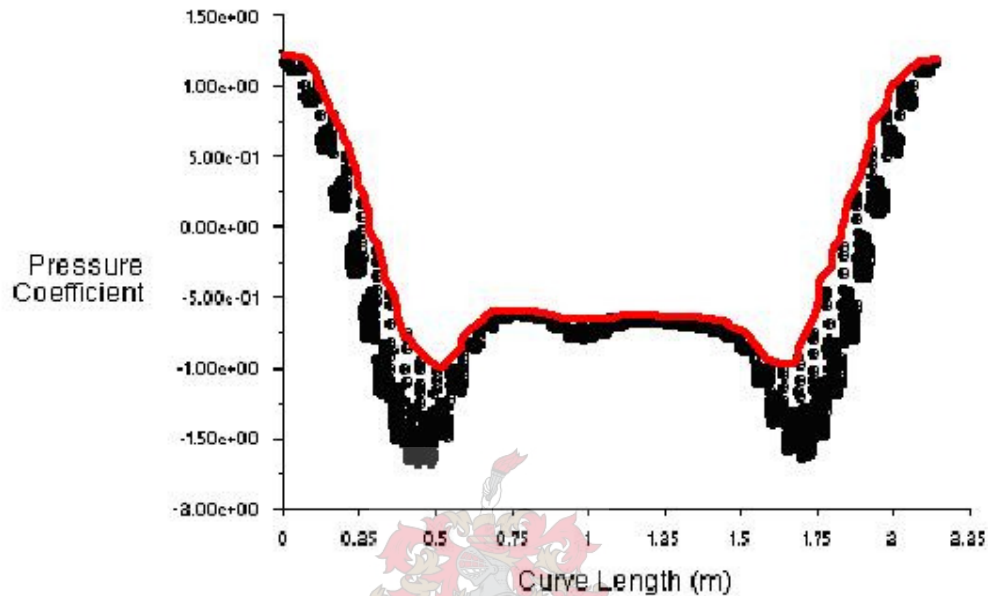


Figure 5.12: External Pressure Coefficients for the Cylinder with 45 Vertical Ribs for a Wind Speed of 30m/s as generated by FLUENT.

The external pressure coefficients can also be displayed as contours as shown in Figure 5.13. These contours show that the external pressure coefficients between the vertical ribs correspond to the lesser suction values. The drawn in red line in Figure 5.12 corresponds to the values at the cylinder wall and is thus used as a comparison against the Japan experimental data in Figure 5.11.

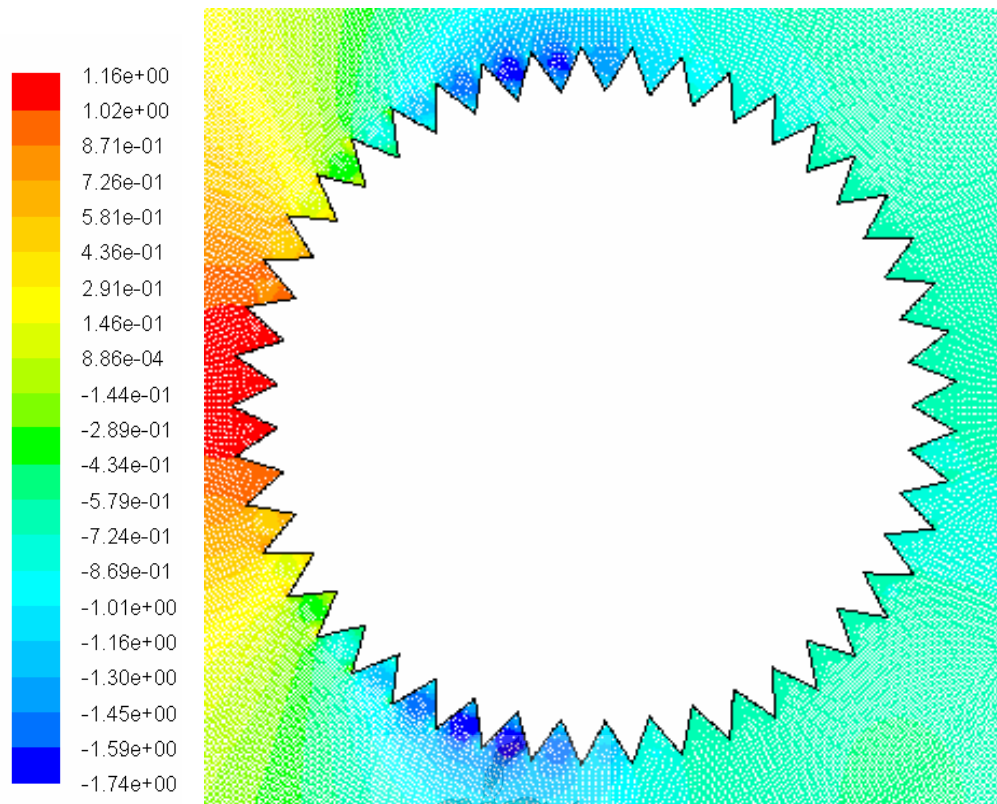


Figure 5.13: External Pressure Coefficients Contours for the Cylinder with 45 Vertical Ribs for a Wind Speed of 30m/s as generated by FLUENT.

It is observed that the greater suction occurs along the length of the vertical rib and not at the tips or valleys of the ribs. This exact pressure distribution together with the structural strength of the vertically ribbed cylinder will need to be studied when investigating the forces that may cause ovalisation of the cylinder.

The vertical ribs reduce the intensity of the negative suction peaks which develop on the sides of the cylinder. This can clearly be seen in Figure 5.14 where the CFD results for the three cylinders are plotted for a wind speed of 30m/s. The average of the pressure distributions of the vertically ribbed cylinders is plotted so as to obtain a single line comparative graph.

The unsymmetrical pressure distribution of the smooth cylinder may be attributed to the boundary layer not being turbulent on both sides before separation occurs. The slight imperfections in the Japan model caused this one sided turbulence at lower wind speeds.

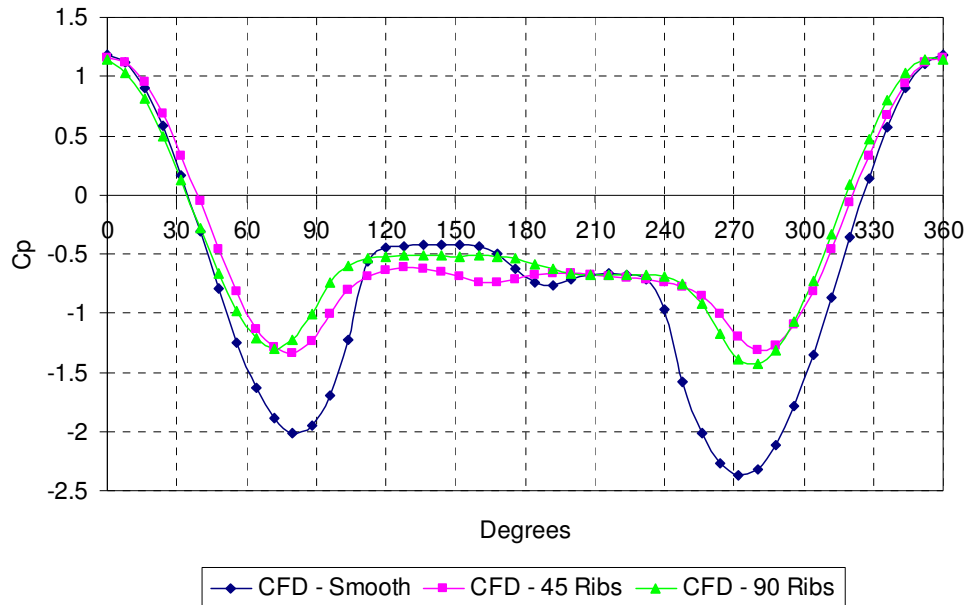


Figure 5.14: External Pressure Coefficients for a Wind Speed of 30m/s.

Also, the external pressure distribution for the vertically ribbed cylinders remains constant over the range of wind speeds (and thus Reynolds number) analysed. This is not true of the smooth cylinder, as the external pressure distribution varies greatly with varying wind speeds.

These are both favourable results as they show that the vertical ribs not only stabilise the external pressure distribution, but also reduce the local pressure forces on the cylinder structure.

The colour plots of the contours of external pressure coefficients for the three models as generated by FLUENT are shown in Figures 5.15, 5.16 and 5.17.

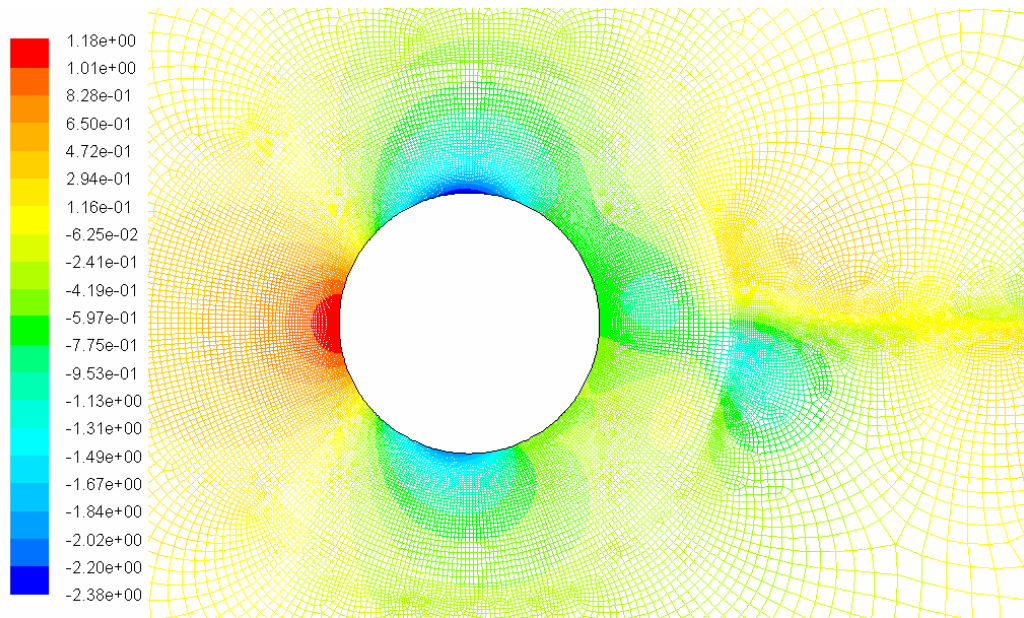


Figure 5.15: Contours of External Pressure Coefficients for the Smooth Cylinder for a Wind Speed of 30m/s.

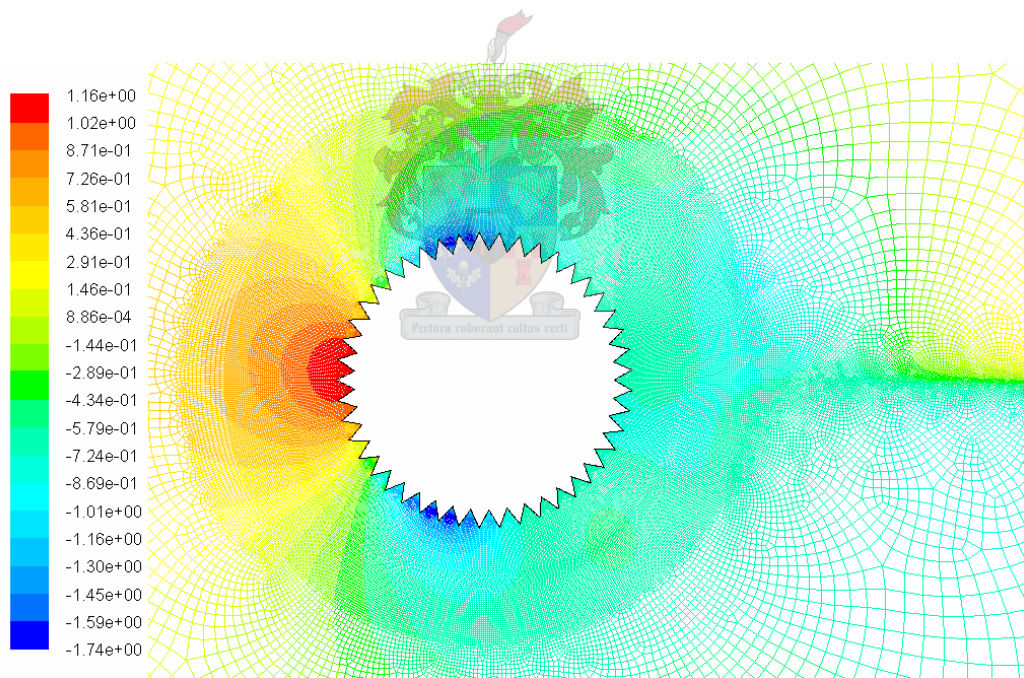


Figure 5.16: Contours of External Pressure Coefficients for the Cylinder with 45 Vertical Ribs for a Wind Speed of 30m/s.

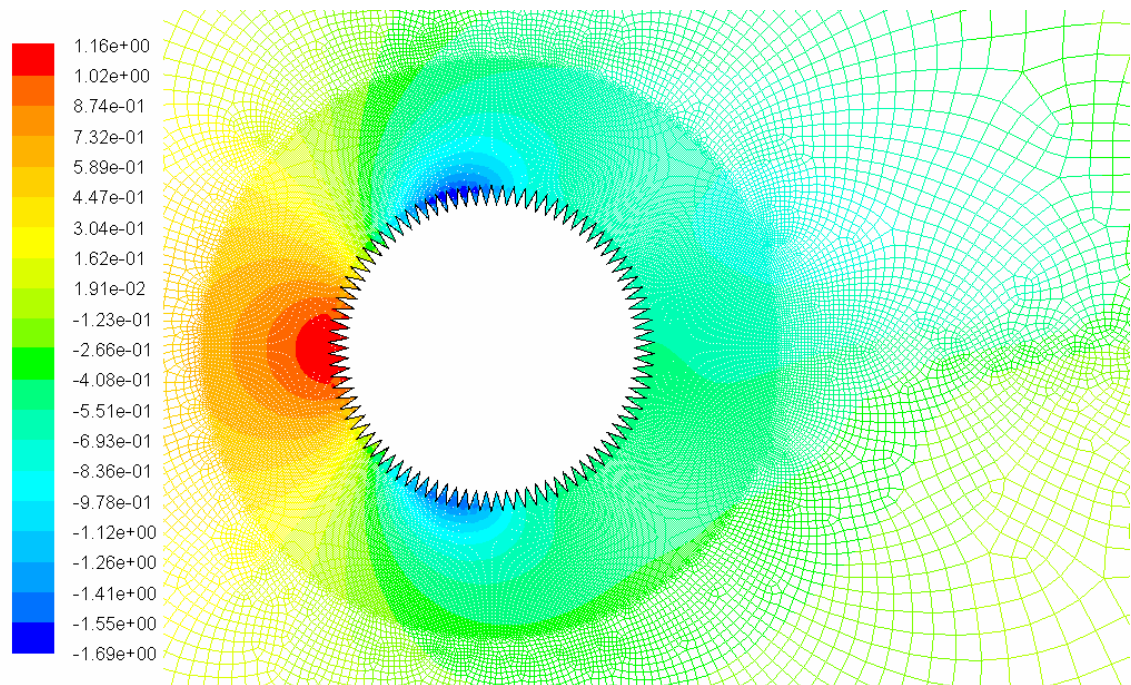


Figure 5.17: Contours of External Pressure Coefficients for the Cylinder with 90 Vertical Ribs for a Wind Speed of 30m/s.

5.5 Conclusions



The results of the CFD analysis are consistent with the experimental pressure distributions (chapter 3.2) and drag coefficients (chapter 3.1.3) as measured in Japan. Once the CFD analysis has been validated over a certain Reynolds number range to confirm that the correct solver is being used, it is an extremely useful tool which can be used efficiently to expand on wind tunnel tests. CFD analysis would for instance be a good way of finding the optimum vertical rib size for tall cylindrical structures. Due to time constraints, this was not part of this study.

The effect of the two impacts of vertical ribs, namely drag coefficient stabilisation and external pressure stabilisation and reduction, will need to be studied in greater detail in order to validate the structural use of such vertical ribs. From these CFD analyses, it would appear that the smaller vertical rib may be more favourable than the larger vertical rib, due to the lower drag. An optimisation study on the rib size is recommended.

6. THE STABILISING ROLE OF VERTICAL RIBS: INTERPRETATION AND DISCUSSION

Vertical ribs influence the structural behaviour of a circular cylinder in numerous ways. Some of these aspects have been tested in the previous chapters and the effects of these results on the structural stability of a tall cylindrical tower are discussed in this chapter.

6.1 Drag Fluctuation

Although it cannot be exactly predicted, it is known that there is a drop and rise in drag coefficient of a smooth cylinder around the critical and super-critical Reynolds numbers. The exact Reynolds number at which this drop occurs as well as the extent of the drop and rise in drag coefficient are extremely sensitive to the conditions of wind flow (the amount of turbulence) and the cylinder properties (smoothness and imperfections). In the case of a tall cylindrical tower, these conditions can not be accurately predicted and may vary with time.

In comparison to the smooth cylinder, the cylinders with vertical ribs show a constant drag coefficient for a large range of Reynolds numbers ($7.3 \times 10^4 < R_e < 6.3 \times 10^5$ tested and $3 \times 10^5 < R_e < 2 \times 10^6$ extrapolated by CFD). This characteristic was common to both vertically ribbed cylinders investigated, although the value of drag coefficient for the size of vertical rib did vary slightly.

It is recalled that the drag force (F_d) on the cylinder is calculated as follows:

$$F_d = 0.5 \times C_d \times \rho \times v^2 \times A \quad (6.1)$$

Where C_d = drag coefficient
 ρ = density of air
 v = wind speed
 A = frontal area of cylinder

The effect of this constant drag coefficient of vertically ribbed cylinders is twofold. Firstly it means that the drag force on the tower can be predicted more accurately as it is only a function of wind speed.

Secondly, the change in drag force with varying Reynolds number of the smooth cylinder leaves two variables changing with time in the drag force equation (the wind speed and the drag coefficient). With sudden changes in wind speed, the variation in drag coefficient results in greater force fluctuations over time on the tower. This could cause along wind oscillation.

Comparatively, the vertically ribbed cylinders have only one variable (wind speed) in the drag force equation (all the other parameters are constant with time). Thus the force fluctuations on the tower will be influenced by the changes in wind speed only. It will not be amplified by a changing drag coefficient. This will reduce the possibility of along wind oscillation.

6.2 Pressure Distribution

The external pressure distribution around a smooth cylinder varies with varying Reynolds number. Above a certain Reynolds number the external pressure distribution is fully developed. However, before it becomes fully developed, any imperfections in the cylinder cause an unsymmetrical external pressure distribution in a small range of Reynolds numbers. This unsymmetrical distribution results in a large local suction on the one side of the cylinder and would need to be investigated as a local load case for the threat of ovalisation of the cylinder. Also, this may lead to lateral vibration with fluctuating wind speed in this range.

In comparison to the smooth cylinder, the vertically ribbed cylinders have a stable external pressure distribution for the entire Reynolds number range tested ($2 \times 10^5 < R_e < 5 \times 10^5$). Thus only one load case of external pressure distribution would need to be considered for vertically ribbed cylinders.

Once the external pressure distribution of the smooth cylinder has developed fully, the suction on the sides of the cylinder reaches a maximum of $C_p = -2.1$. The maximum measured suction on the sides of both the vertically ribbed cylinders is $C_p = -1$. The vertical ribs thus greatly reduce the suction on the sides of the cylinder which in turn reduces the effect of ovalisation. As well as reducing the suction on the sides of the cylinder, the vertical ribs also add structural stability to prevent ovalisation.

6.3 Forces and Moments on the Structure

The dominant force acting on tall towers is the drag force as a result of wind loading. This force is distributed along the height of the tower and results in a moment about the base of the structure. The base design of the tower needs to be able to withstand both the force and moment mentioned above.

Although the drag coefficient of the vertically ribbed cylinders is greater than the drag coefficient of the smooth cylinder at Reynolds numbers greater than the critical Reynolds number, this does not have a significantly negative effect on the forces or moments which the tower base would experience.

It is only over a fairly small Reynolds number range where the drag coefficient of the smooth cylinder is noticeably less than that of the vertically ribbed cylinders. Thereafter, the drag coefficient of a smooth cylinder increases again and reaches a value of $C_d = 0.81$. The vertically ribbed cylinders' drag coefficient is very close to this value, namely 0.83 for the larger vertical ribs and 0.79 for the smaller vertical ribs. This drag coefficient could still be optimised by finding the optimal vertical rib size.

However, for the dimensions of the proposed Solar Chimney, the Chimney will never fall in this critical Reynolds number range. Even for a conservative chimney diameter (D) of 100m and a wind speed (v) of 1m/s, the Reynolds number ($Re = vD/\nu$) is equal to 6.62×10^6 . This means that the drag forces acting on the Solar Chimney for all wind speeds will be calculated using a drag coefficient of 0.81 for a smooth cylinder. The comparison of drag coefficients can be seen in Figure 6.1.

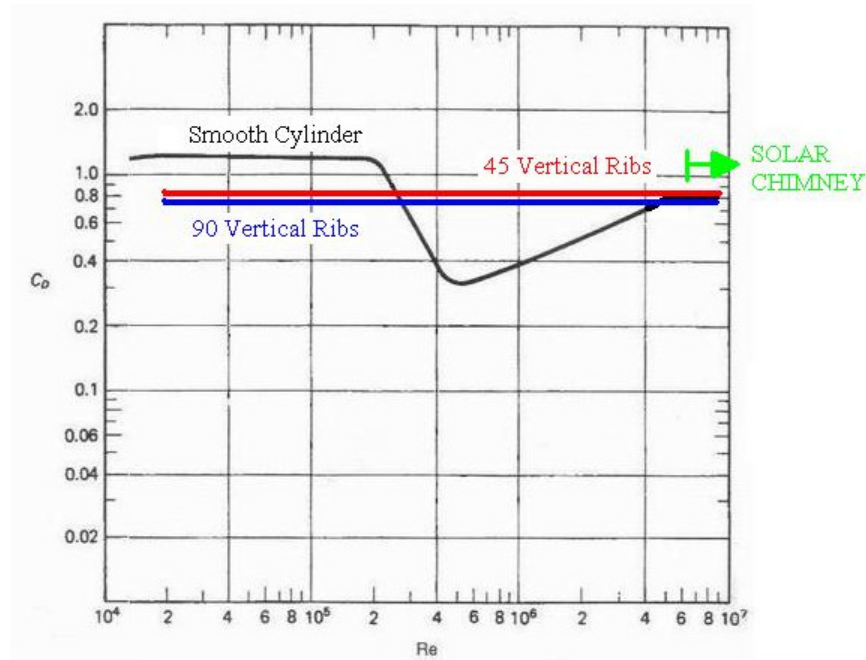


Figure 6.1: Drag Coefficient Comparison for the Solar Chimney. Note that the C_D for the vertically ribbed cylinders has been extrapolated from the computed range (up to $Re = 2 \times 10^6$) for visualization purpose.

Even when using the conservative drag coefficient of 0.83 for the larger vertically ribbed cylinder, the forces and moments at the base of the structure will only be 2.5 % greater than those of the smooth cylinder. By optimising the vertical rib size, (for instance $C_d = 0.79$ for the smaller rib) the drag force could in fact be reduced.

Thus, even though the drag coefficient for the vertically ribbed cylinder may be greater than that of the smooth cylinder over a certain Reynolds number range, the benefits of the stabilising properties of the vertical ribs far outweigh the slight increase in drag force that the tower may experience.

7. CONCLUSIONS

7.1 Stabilised Drag Coefficient

Unlike the drag coefficient graph for a smooth cylinder which displays a drop and rise at some Reynolds number range, the drag coefficient for the vertically ribbed cylinders remains constant for the entire Reynolds number range tested.

7.2 Better Prediction of Drag Force

As a result of the drag coefficient of a vertically ribbed cylinder being constant for all variations of Reynolds number, the drag forces acting on the tower can be predicted more accurately.

The problem that arises for predicting the drag force on a smooth cylinder is that the Reynolds number at which the drop and rise in drag coefficient occurs cannot be exactly determined. This is due to uncontrollable influences such as construction imperfections and wind turbulence which influence the Reynolds number at which the drag coefficient drops and rises.

In contrast, the vertically ribbed cylinder is to a great extent not influenced by these varying circumstances and thus makes drag force predictions much easier.

7.3 Reduction in Along Wind Oscillation Threat

Along wind oscillation could be caused by sudden changes in wind speed, together with the variation in drag coefficient for the smooth cylinder, which may result in great force fluctuations over time on the tower. These two variables (wind speed and drag coefficient) combine to amplify the possible fluctuation in drag force acting on the tower.

Comparatively, the vertically ribbed cylinders have only one variable (wind speed) in the drag force equation (as all the other parameters are constant with time). Thus the force fluctuations on the tower will only be influenced by the changes in wind speed (and not amplified by a changing drag coefficient). This will reduce the possibility of along wind oscillation.

7.4 Comparable Forces and Moments

Although the drag coefficient of the vertically ribbed cylinders is larger than the drag coefficient of the smooth cylinder at Reynolds numbers greater than the critical Reynolds number, this does not have a significantly negative effect on the forces of moments which the tower base would experience.

By using a conservative wind profile and drag coefficient distribution, there is only a 2.5% increase in the force on the tower and moment exerted on the base of the structure. Thus, the benefits of the stabilising properties of the vertical ribs far outweigh the slight increase in drag force that the tower may experience.

7.5 Unsymmetrical External Pressure Distribution Eliminated

Due to the sensitivity of flow around a smooth cylinder, any imperfections in the cylinder cause an unsymmetrical external pressure distribution in the range of the critical Reynolds number. This results in a large local suction forming on the one side of the cylinder while not on the other side.

Such imperfections would be inevitable in the construction of a tower. The presence of vertical ribs removes this sensitivity to imperfections and thus eliminates the unsymmetrical external pressure loading case.

7.6 Stabilised External Pressure Distribution

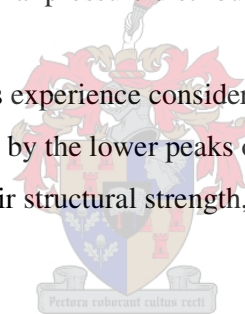
Unlike the external pressure distribution of the smooth cylinder which varies above and below the critical Reynolds number, the external pressure distribution of the vertically ribbed cylinders remains constant throughout the Reynolds number range tested.

Although the pressure distribution varies along the rib profile (from the valley to the tip of the rib), the forces acting on the tower wall need only be calculated for one load case.

7.7 Reduction of Ovalisation Threat

One of the major threats to the stability of tall cylindrical towers is the threat of ovalisation. This occurs due to large suction forces developing on the sides of the cylinder as a result of the external pressure distribution around the cylinder.

The vertically ribbed cylinders experience considerably lower suction on the sides of the cylinder which can be seen by the lower peaks of their external pressure coefficient graphs. This, together with their structural strength, greatly reduces the threat of ovalisation.



7.8 Cross-wind Oscillation Postulation

Cross-wind oscillation is mainly caused by the uneven shedding of vortices from the cylinder. The uneven vortex shedding results in a side-ways punching effect on the cylinder which causes it to oscillate in the cross-wind direction.

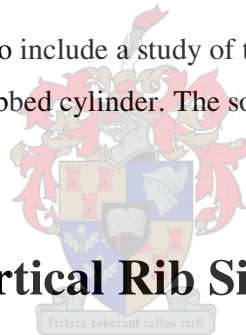
Based on the theoretical studies of the various flow regimes (Chapter 1) and their developments, it is postulated that the lack of uneven vortex shedding in the transcritical flow regime eliminates this threat of cross-wind oscillation as, due to its size, the solar chimney falls entirely into the transcritical flow regime.

8. RECOMMENDATIONS AND PROPOSALS FOR FUTURE STUDIES

8.1 Dynamic Modelling

Three-dimensional dynamic modelling of a proposed vertically ribbed tower should be carried out. The dynamic modelling should include various wind profile distributions with height along the tower as well as fluctuations in wind speed with time. This study would investigate the failure modes of the tower as well as the forces and moments acting on the base of the structure.

Dynamic modelling should also include a study of the threat of ovalisation to confirm the behaviour of a vertically ribbed cylinder. The software program DIANA could be used for this.



8.2 Optimal Vertical Rib Size

The optimal vertical rib size needs to be determined. This can be done by means of Computational Fluid Dynamics analysis of cylinders with various rib sizes. Once the optimal vertical rib size has been identified, based on criteria drag coefficient and external pressure, it can be tested experimentally to confirm its characteristics. From solid mechanics analysis, including dynamic analysis as suggested in Chapter 8.1, the structural stability of this rib choice should also be confirmed.

8.3 Transcritical Flow Regime

The transcritical flow regime remains a generally unexplored area as far as flow around a cylinder is concerned. Ways need to be developed to be able to perform experimental tests into this flow regime in order to verify the postulations that have been made.

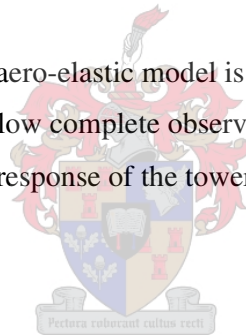
Possible ways of gaining knowledge of the transcritical flow regime are by means of measurement apparatus on large real life structures. This is an expensive method, but has proved useful in previous studies.

8.4 Flow Visualisation

Flow visualisation by means of experimental testing as well as CFD modelling can be very useful for the investigation of vortex shedding. This would help to contribute towards the study of cross-wind oscillation.

8.5 Aero-elastic Model Testing

Finally, it is suggested that an aero-elastic model is tested experimentally in order to confirm all other results and allow complete observation of the structure's behaviour. This would include the global response of the tower as well as the local effects of ovalisation.



9. REFERENCES

9.1 Papers

Achenbach, E., (1971). Influence of surface roughness on the cross-flow around a circular cylinder, *Journal of Fluid Mechanics*. Volume 46, p321-p335.

Achenbach, E. and Heinecke, E., (1981). On vortex shedding from smooth and rough cylinders in the range of Reynolds numbers 6×10^3 to 5×10^6 , *Journal of Fluid Mechanics*. Volume 109, p239-p251

Alberti, L.T., (2004). *Wind Effects on the Solar Chimney*. BEng Final year project report, University of Stellenbosch.

Benim, A.C. and Zinser, W., (1986). A segregated formulation of Navier-Stokes equations with finite elements, *Computer Methods in Applied Mechanics and Engineering*. Volume 57, p223-p237.

Du Buisson, J.J., (1988). *The effectiveness of commercially available components used to decrease the aerodynamic drag force on heavy motor vehicles*. MEng Report, University of Stellenbosch

Halse, K.H., (1997). *On vortex shedding and prediction of vortex-induced vibrations of circular cylinders*. MTA-rapport 1997:117, Ch. 2.

Niemann, H.-J. and Hölscher, N., (1990). A review of recent experiments on the flow past circular cylinders, *Journal of Wind Engineering and Industrial Aerodynamics*. Volume 33, p197-p209.

Schewe, G., (1983). On the force fluctuations acting on a circular cylinder in crossflow from subcritical up to transcritical Reynolds numbers, *Journal of Fluid Mechanics*. Volume 133, p265-p285

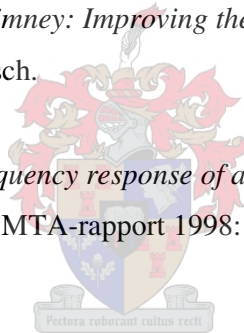
Schlaich, J. et al, (2004). Sustainable Electricity Generation with Solar Updraft Towers, *Structural Engineering International*. Volume 3/2004, p225.

Summer, D. et al, (2004). Wake structure of a finite circular cylinder of small aspect ratio. *Experiments in Fluids*. Volume 37, p720 – p730.

Tamura, Y., (2002). *Recent Topics in Wind Engineering Focusing on Monitoring Techniques*. An International Conference with the theme ADVANCES IN BUILDINGTECHNOLOGY (ABT2002), Hong Kong, 4 - 6 December 2002

Van Dyk, C., (2001). *Solar Chimney: Improving the Concept*. BEng Final year project report, University of Stellenbosch.

Vikestad, K., (1998). *Multi-frequency response of a cylinder subjected to vortex shedding and support motions*. MTA-rapport 1998:120, p15-p17



9.2 Books

Houghton, E.L. and Carruthers, N.B., (1976). *Wind forces on buildings and structures*. John Wiley & Sons, New York. p32, p70.

Potter, M.C. and Wiggert, D.C., (2002). *Mechanics of Fluids*. Prentice Hall. 3rd Edition. Ch. 5 & Ch. 8.

Sachs, P., (1978). *Wind Forces in Engineering*. Pergamon Press, Oxford. 2nd Edition, p45, p51, p61, p70, p109, p129, p283.

9.3 Internet Resources

Talley, S. and Mungal, G, (2002). *Flow around cactus-shaped cylinders*.
ctr.stanford.edu/ResBriefs02/talley.pdf

FLUENT (2004) Release 6.2.16 online documentation (www.fluentusers.com)

GAMBIT (2004) Release 2.3.16 online documentation (www.fluentusers.com)

www.engineeringtoolbox.com/

www.wordiq.com/definition

APPENDIX A: DETAILED REPORT OF WIND TUNNEL TESTING: SHIMIZU CORPORATION, TOKYO, JAPAN

A.1 The Wind Tunnel

Wind tunnel tests were performed in the closed circuit wind tunnel at the Shimizu Corporation, Institute of Technology in Tokyo, Japan. A photo of a model of the wind tunnel can be seen in Figure A1.1.

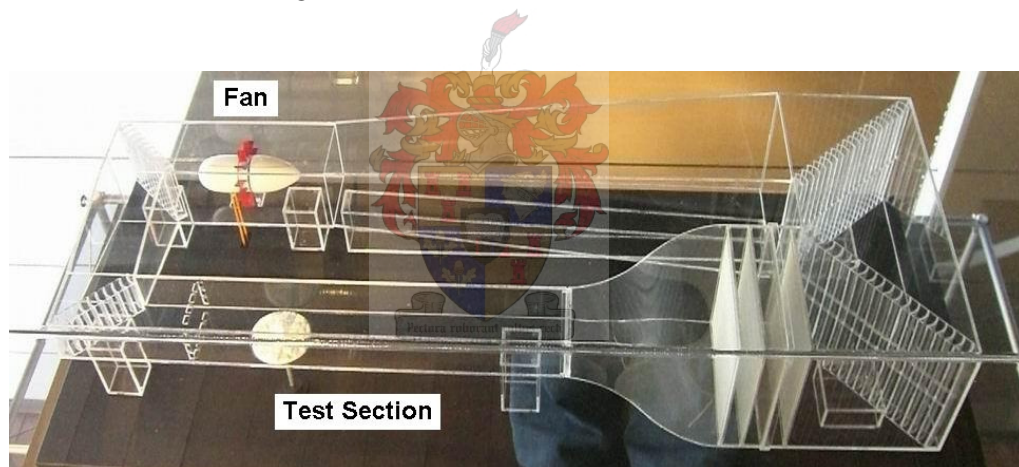


Figure A1.1: The Model of the Closed Circuit Wind Tunnel, Shimizu Corporation, Tokyo, Japan.

Maximum wind speeds of 35 m/s can be generated in the wind tunnel by the 4m diameter fan which can be seen in Figure A1.2. Small vibrations of the model were however observed at wind speeds above 25m/s resulting in the maximum tested wind speed being 25m/s.

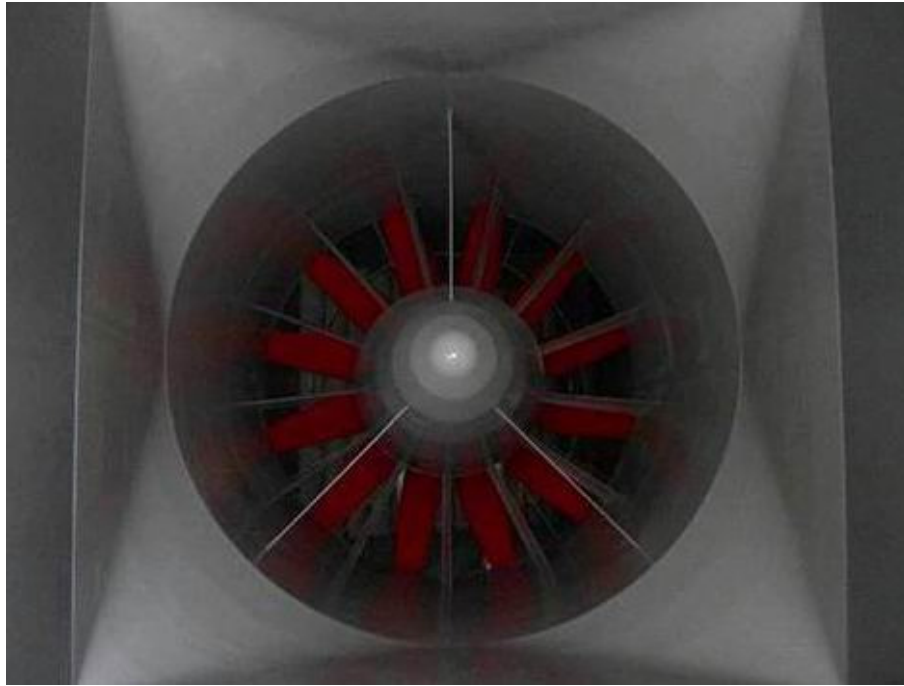


Figure A1.2: The 4m Diameter Wind Tunnel Fan.

The air moves through guide vanes when changing direction at the corners of the wind tunnel. The size of these guide vanes can be seen as someone steps through them in Figure A1.3.



Figure A1.3: The Guide Vanes in the Corners of the Wind Tunnel

Once the air is travelling in the direction of the test section, any turbulence in the air is broken up by the air passes through four sheets of mesh before reaching the test section. The positioning of these mesh sheets can be seen in Figure A1.1. The mesh is shown in Figure A1.4.



Figure A1.4: The Mesh which breaks up any Turbulence in the Wind Tunnel.

The testing section has size 3.5m width x 20m length x 2.5m height. The model size was thus determined in order to ensure a blockage ratio of less than 5%. The blockage ratio for the models was 4%.

The 20m length of the test section can be used to model ground profiles so as to develop a wind profile for a built up city for instance. For these tests, the length of the test section was left smooth.

The main part of the test section has a turntable to allow rotation of the model. This section has viewing panes on both sides. A photo from inside the test section looking out of the viewing pane can be seen in Figure A1.5.



Figure A1.5: A Photo from inside the Test Section.

A.2 The Models

Three different chimney models were used. All models were 1000 mm in length (height) and closed at the top end to reduce 3D flow effects. 300 mm diameter Perspex pipe was used for all three models. V-shaped Perspex strips were added around two of the models in order to create vertical ribs.

The first model was that of a smooth circular cylinder with outer diameter of 300 mm. The aspect ratio ($AR = \text{height} / \text{diameter}$) of the smooth cylinder was $1000/300 = 3.33$. Pressure taps were placed every 8° around the circumference of the cylinder. There were three rows of these pressure taps at heights of 400 mm, 500 mm and 600 mm from the base. This can be seen in Figure A2.1 and A2.2.



Figure A2.1: The Smooth Cylinder Model with Pressure Taps in the Closed Circuit Wind Tunnel.

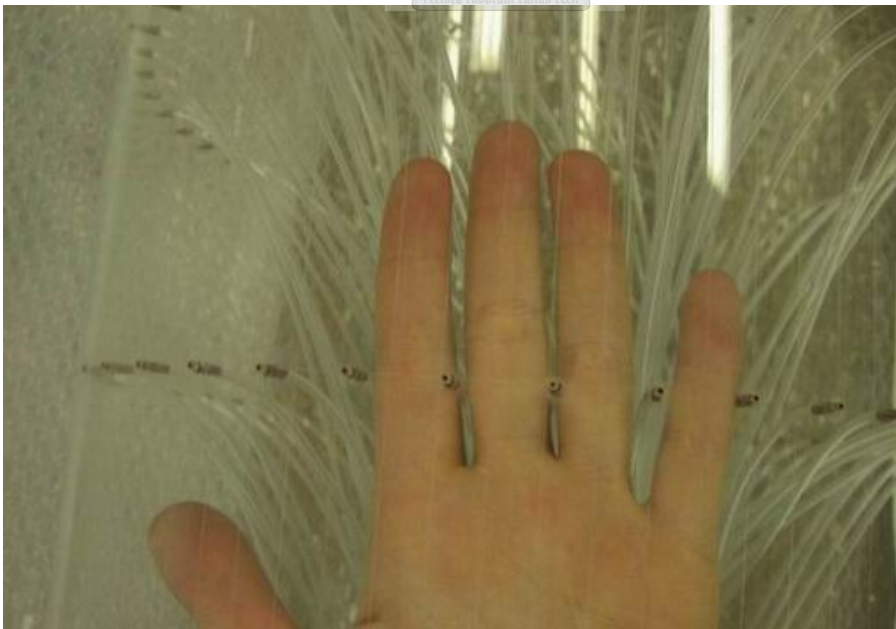


Figure A2.2: The Pressure Taps

The second model was that of a cylinder with 45 vertical ribs (one vertical rib every 8°). The ribs extended 21 mm from the circular pipe, making the cylinder outer diameter 342 mm. The l/d ratio of the model (where l = depth of vertical rib and d = diameter of cylinder) was thus $21/300 = 0.07$. Pressure taps were placed every 8° around the circumference of the cylinder between the vertical ribs (on the circular cylinder wall). There were three rows of these pressure taps at heights of 400 mm, 500 mm and 600 mm from the base. A photo of the model can be seen in Figure A2.3.

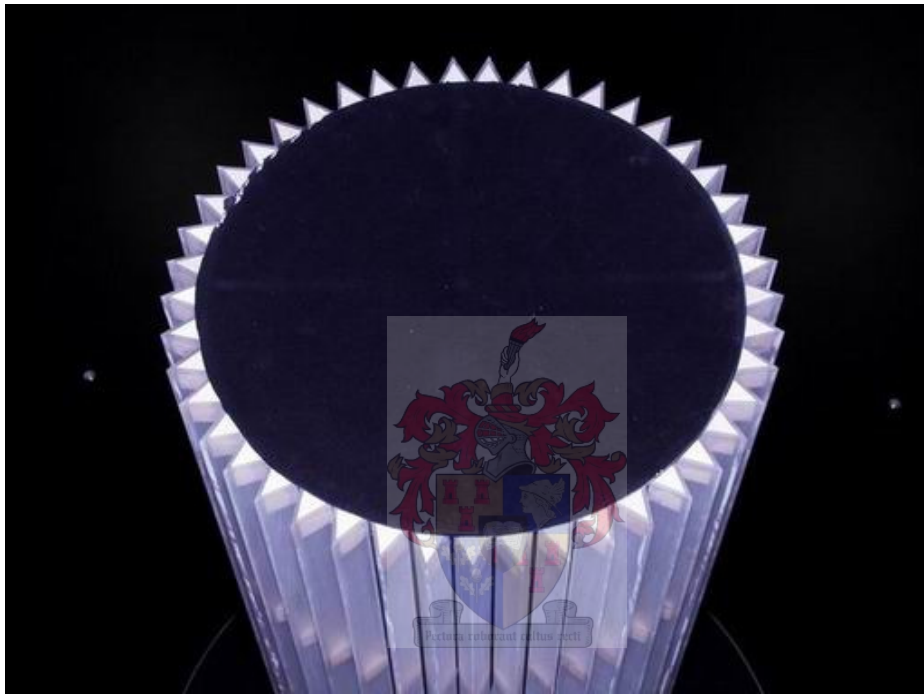


Figure A2.3: The Cylinder Model with 45 Vertical Ribs.

The third model was that of a cylinder with 90 vertical ribs (one vertical rib every 4°). The ribs extended 21 mm from the circular pipe, making the cylinder outer diameter 342 mm. The l/d ratio of the model was thus $21/300 = 0.07$. Pressure taps were placed every 8° around the circumference of the cylinder between every second vertical rib (on the circular cylinder wall). There were three rows of these pressure taps at heights of 400 mm, 500 mm and 600 mm from the base.

The three models are shown schematically in Figure A2.4.

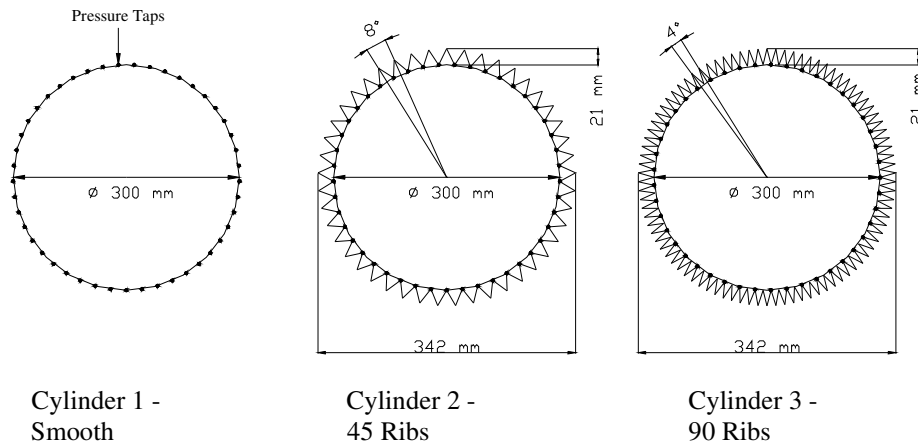


Figure A2.4: Three Cylinder Models of Height 1000 mm used for this test.

A.3 Data Acquisition

Each pressure tap was connected to the measurement apparatus which is in turn connected to a computer system which receives the measurements and processes them. The wind tunnel wind speeds are also controlled by a computer system which sets the revolutions per minute which the fan must turn to produce a certain wind speed. This touch screen can be seen in Figure A3.1.

All data acquisition is done by means of the computer system connected to the wind tunnel and measurement apparatus. The external pressure distributions are obtained in the form of data files which are then analysed with the help of Matlab. Matlab programs were written to produce both graphs for the external pressure distributions as well as for calculating the drag coefficients.



Figure A3.1: The Touch Screen which controls the Wind Tunnel Fan.

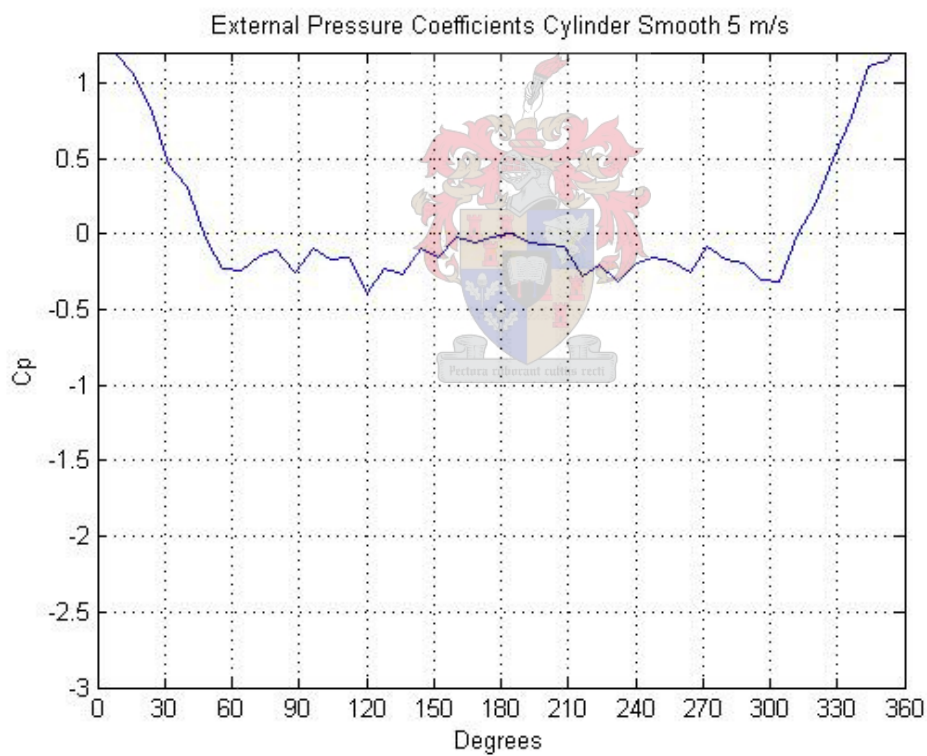
A.4 Limitations

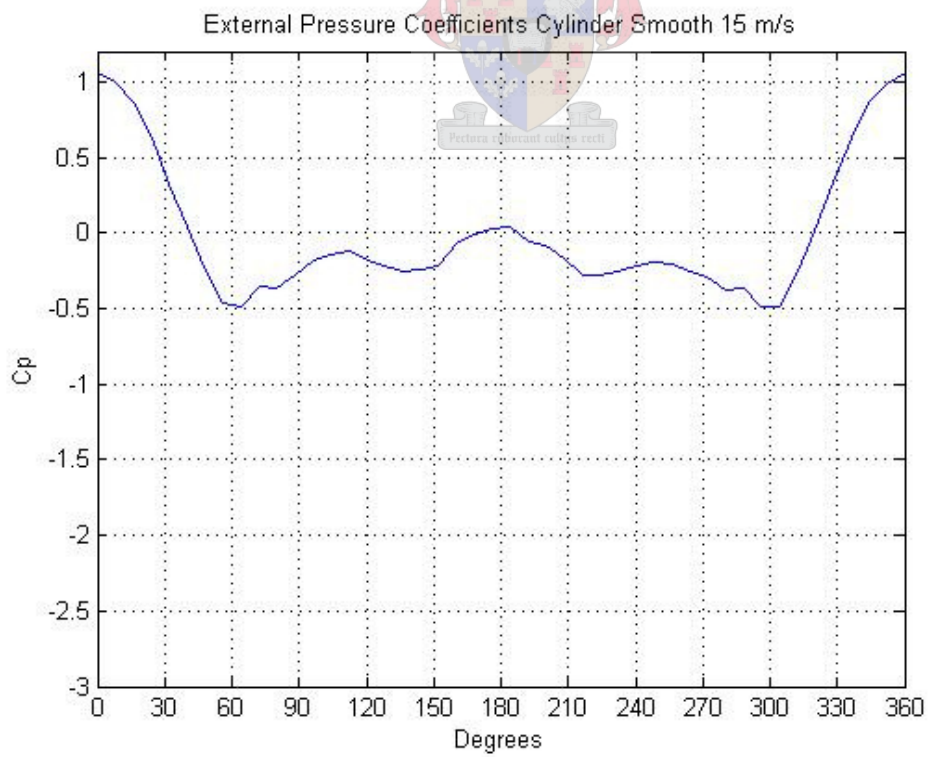
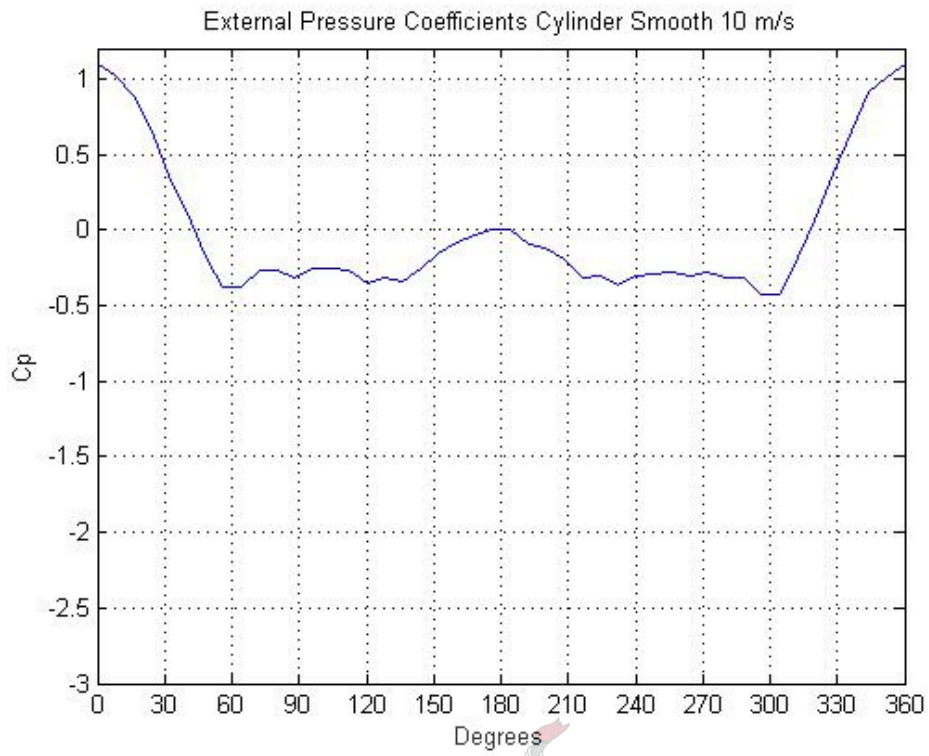
Due to the low rpm needed to produce low wind speeds, wind speeds below 10 m/s are not very stable. This is clearly seen for the data sets for the wind speed equal to 5 m/s. These readings will thus not be considered for analysis.

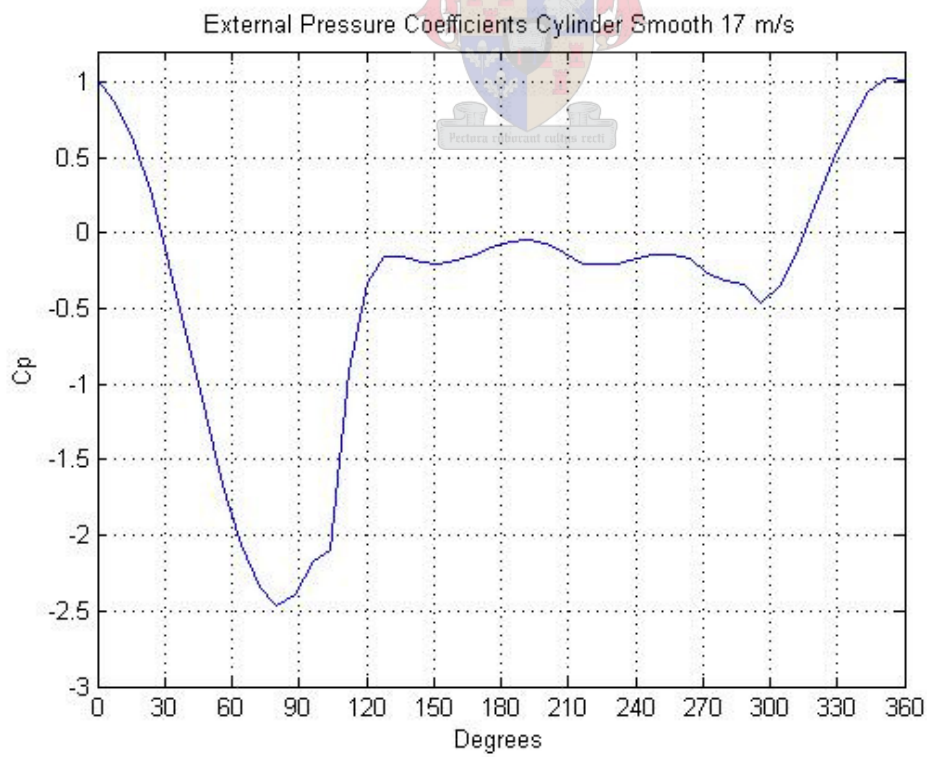
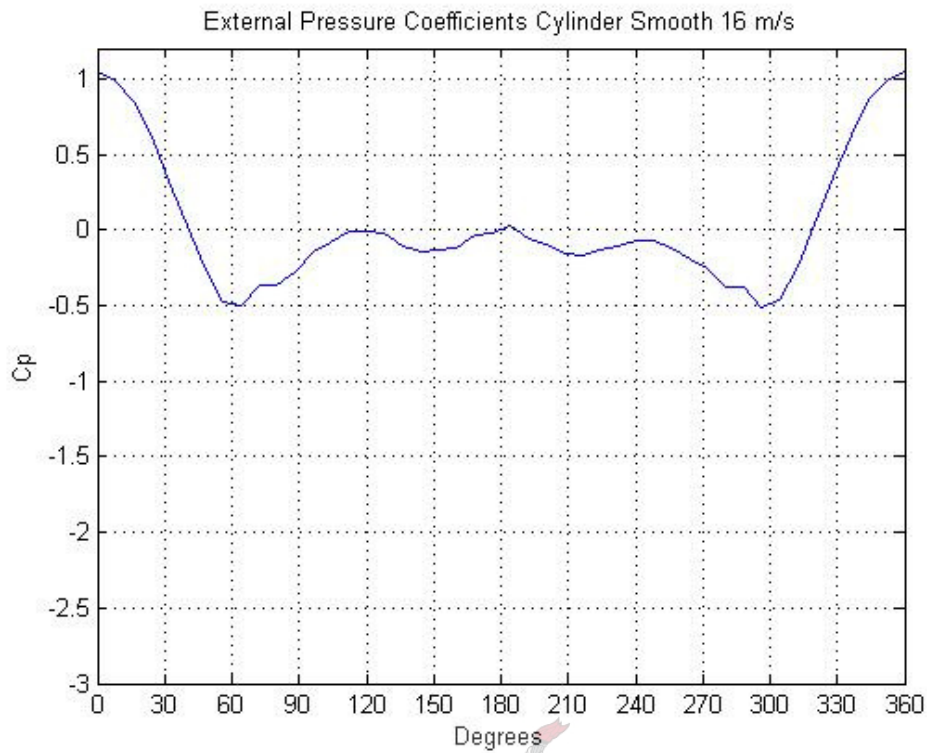
At wind speeds higher than 25 m/s the model begins to vibrate and accurate pressure readings can thus not be taken. The Reynolds number range that was able to be tested is thus $9.9 \times 10^4 < Re < 5.6 \times 10^5$. This unfortunately does not extend into the transcritical flow regime.

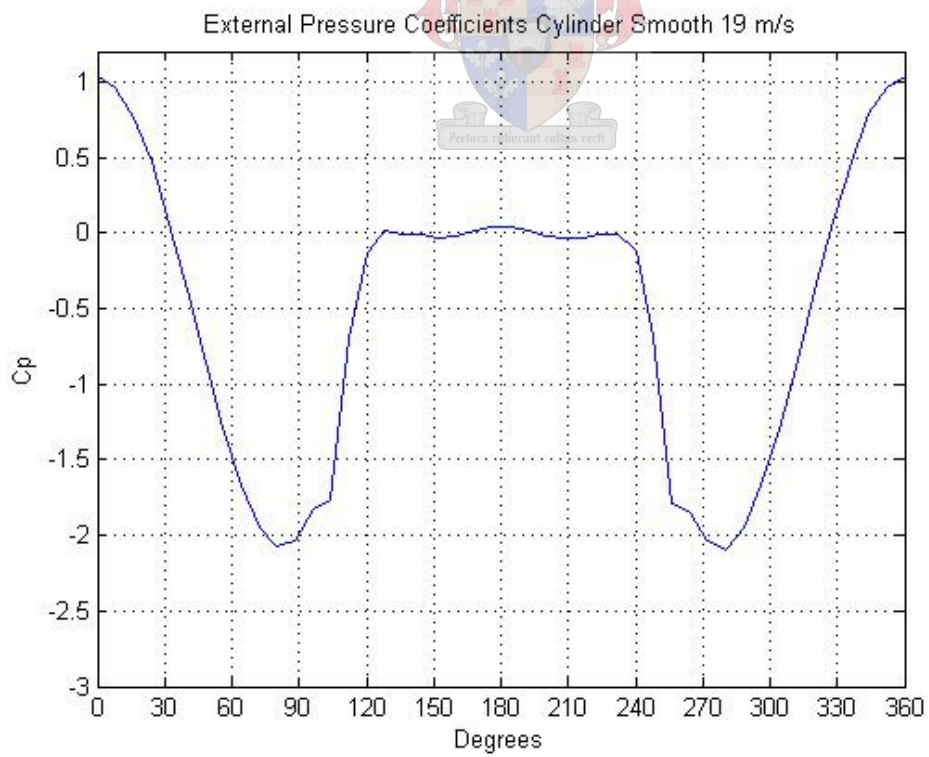
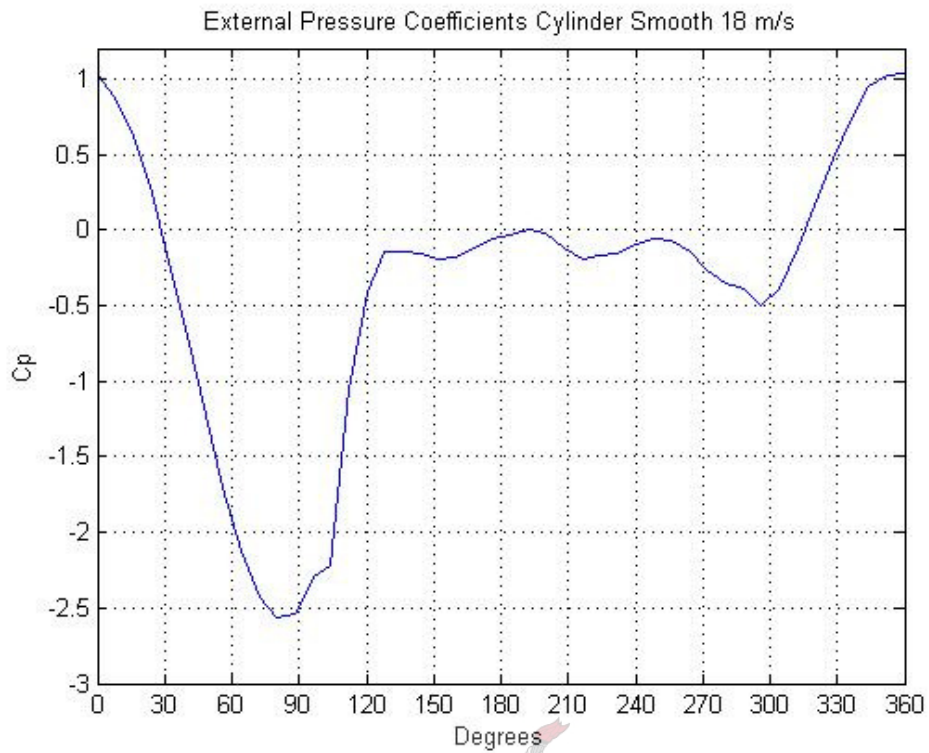
APPENDIX B: WIND TUNNEL TEST RESULTS: SHIMIZU CORPORATION, TOKYO, JAPAN

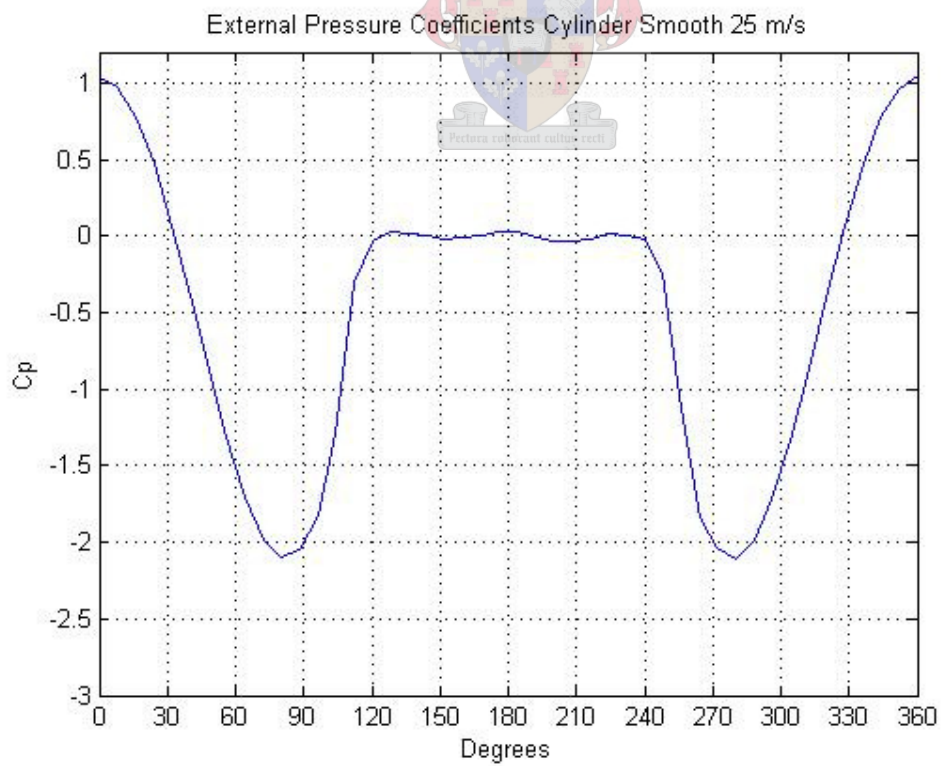
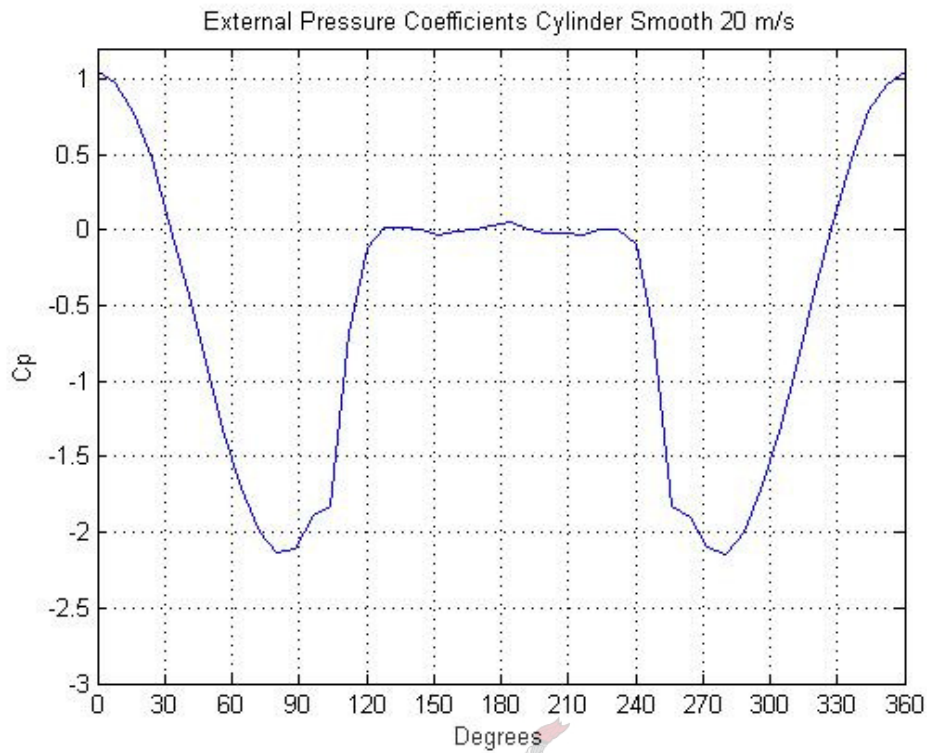
B.1 External Pressure Coefficients for the Smooth Cylinder for all Wind Speeds



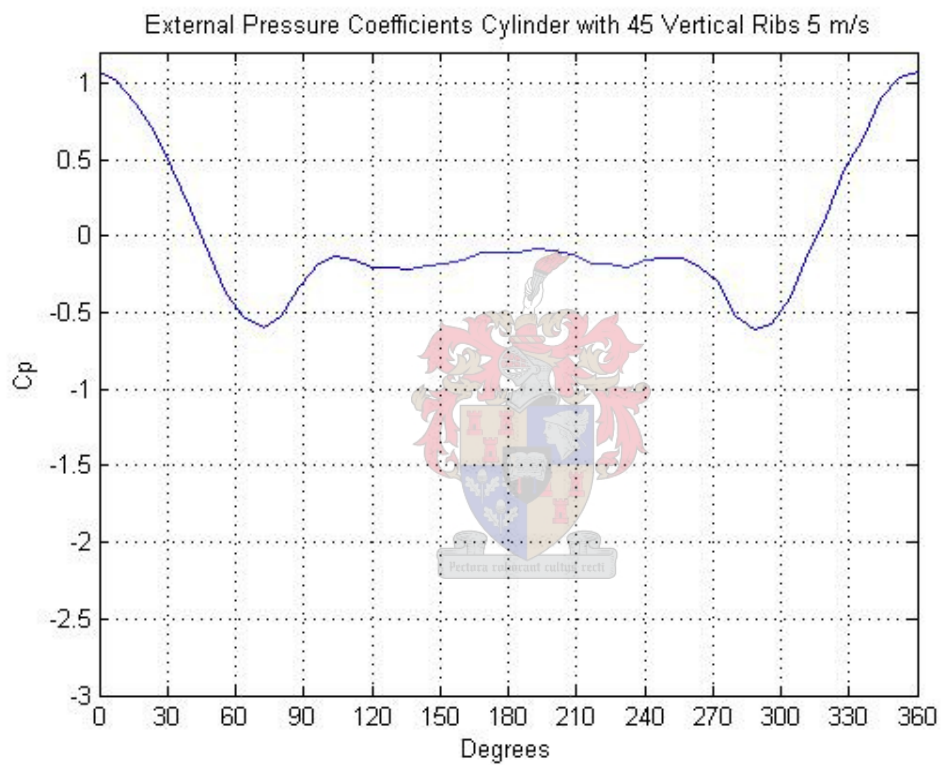


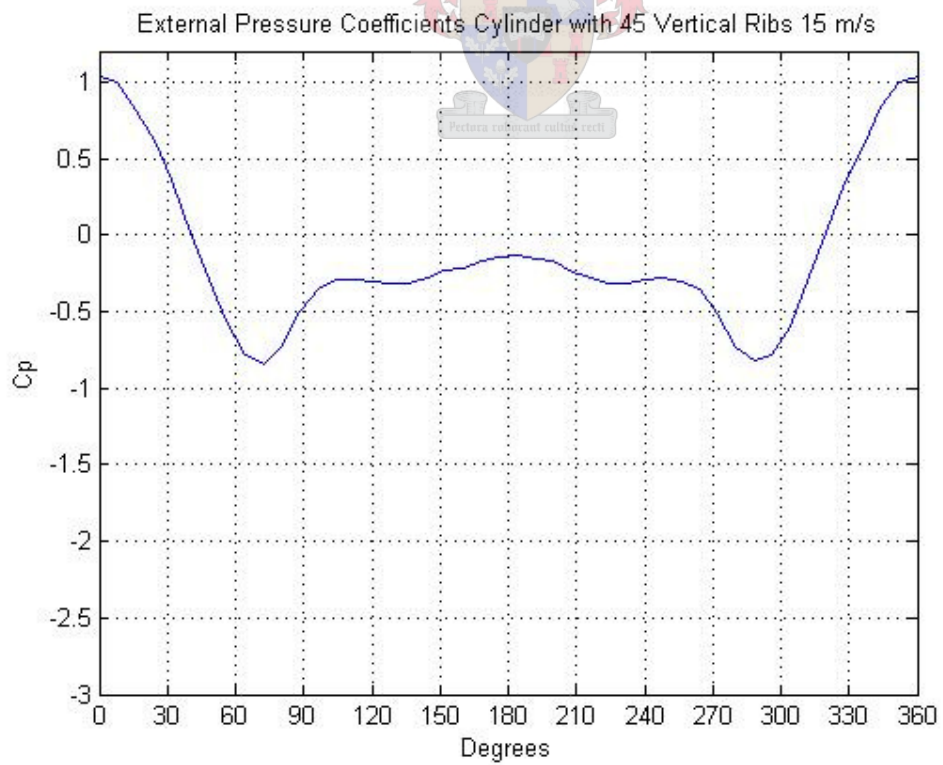
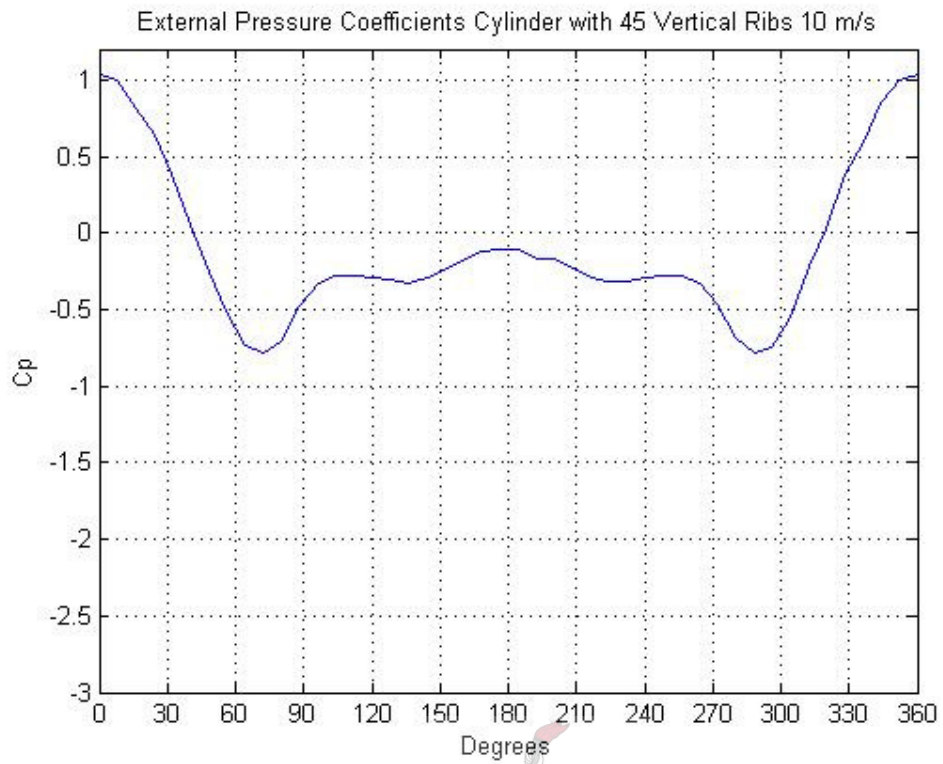


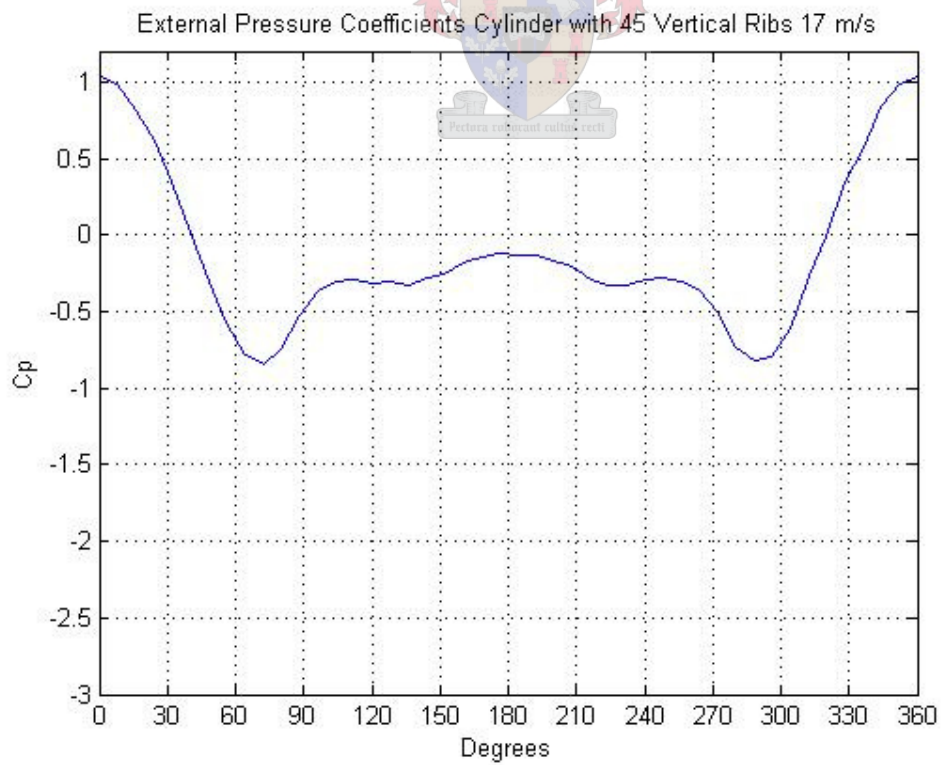
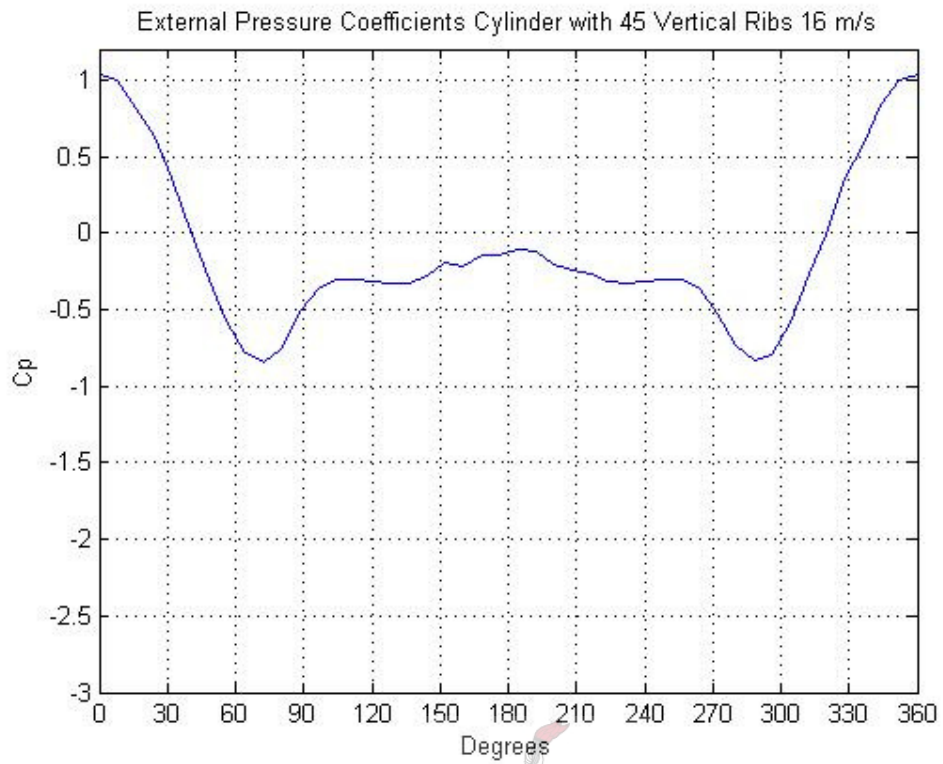


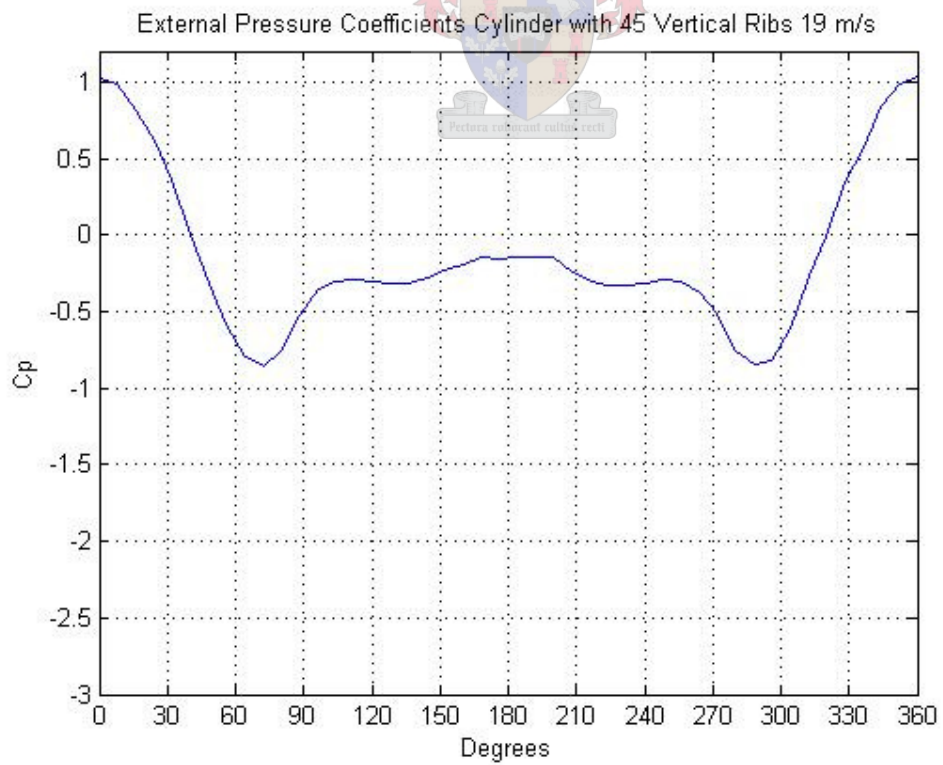
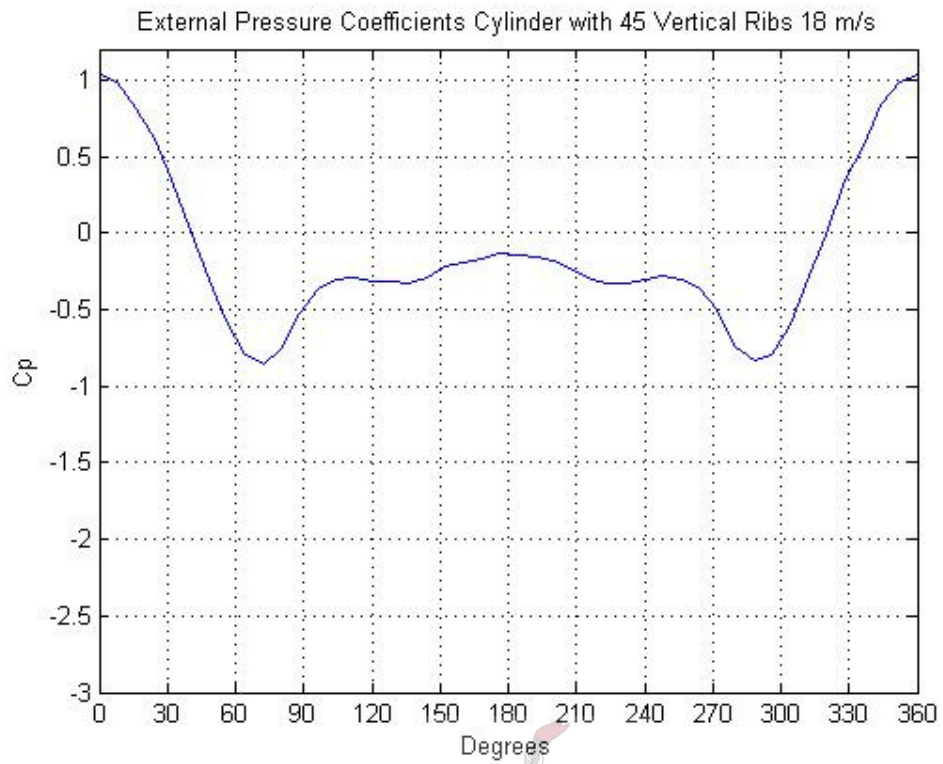


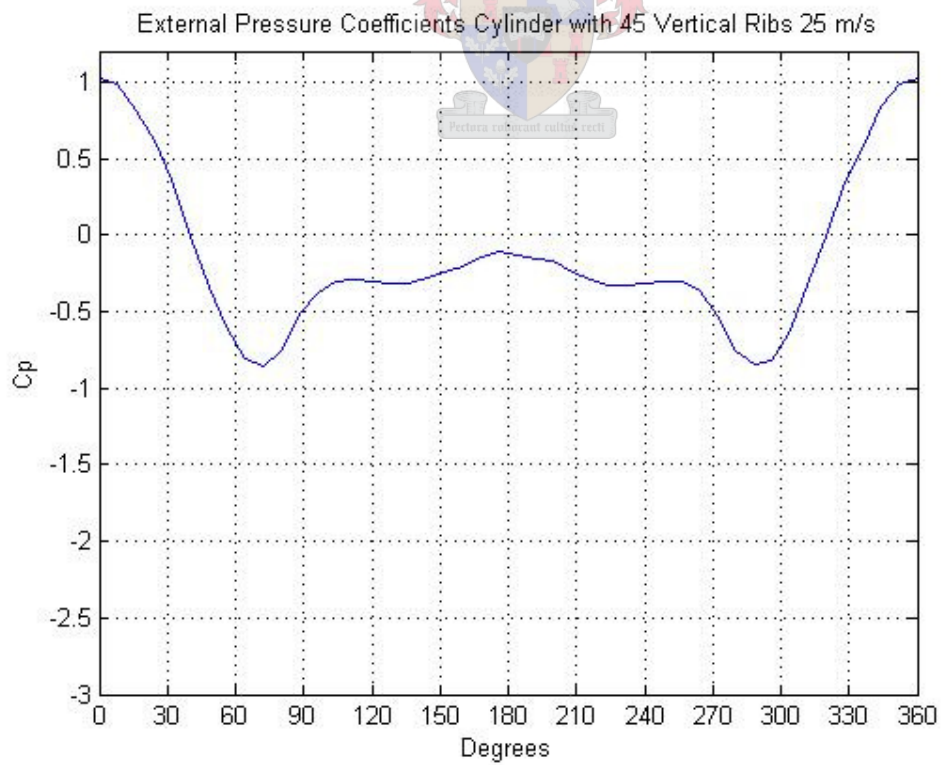
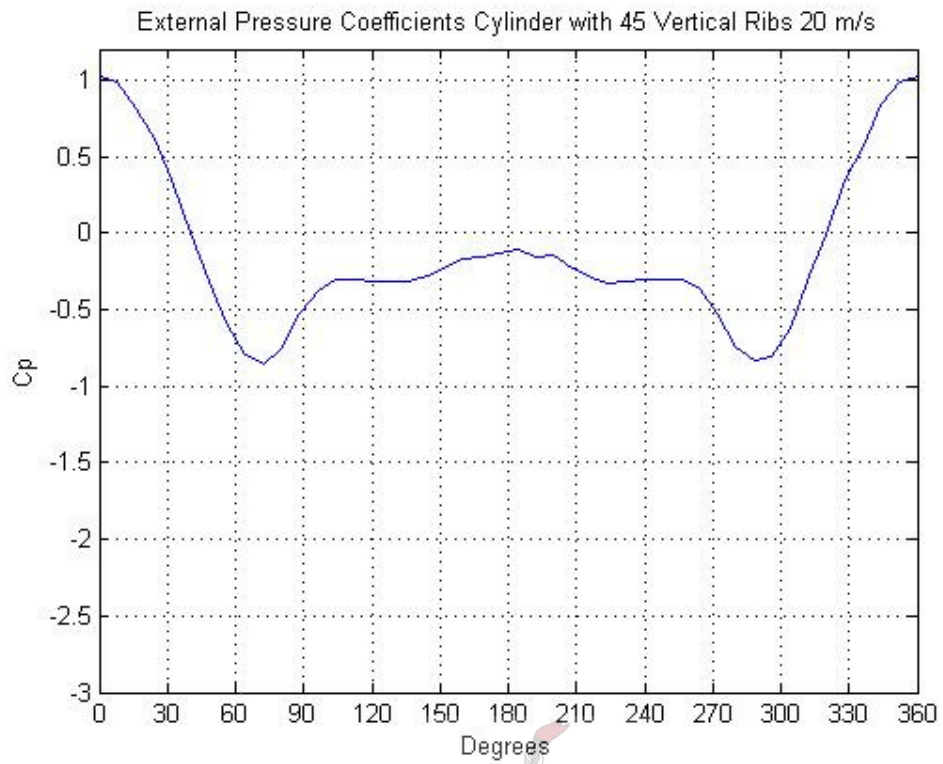
B.2 External Pressure Coefficients for the Cylinder with 45 Vertical Ribs for all Wind Speeds



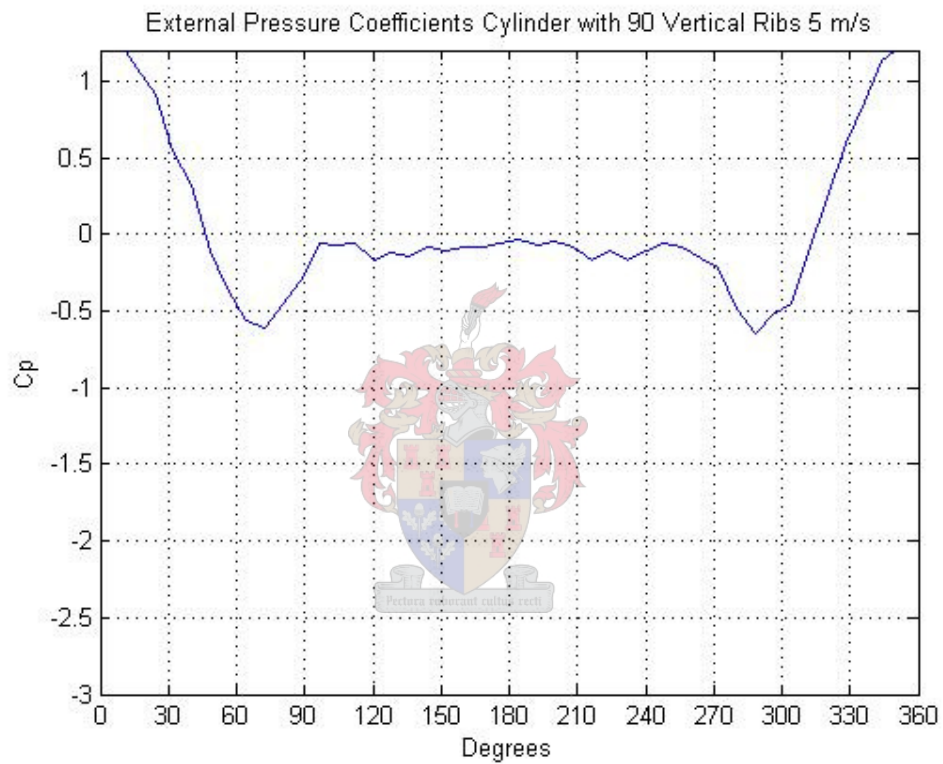


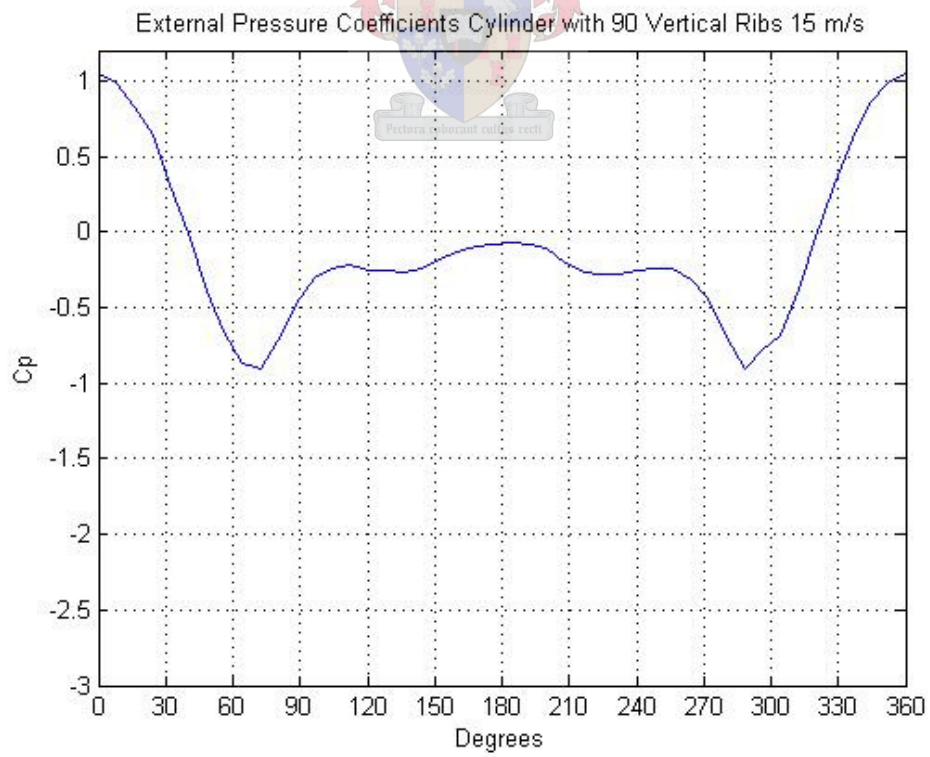
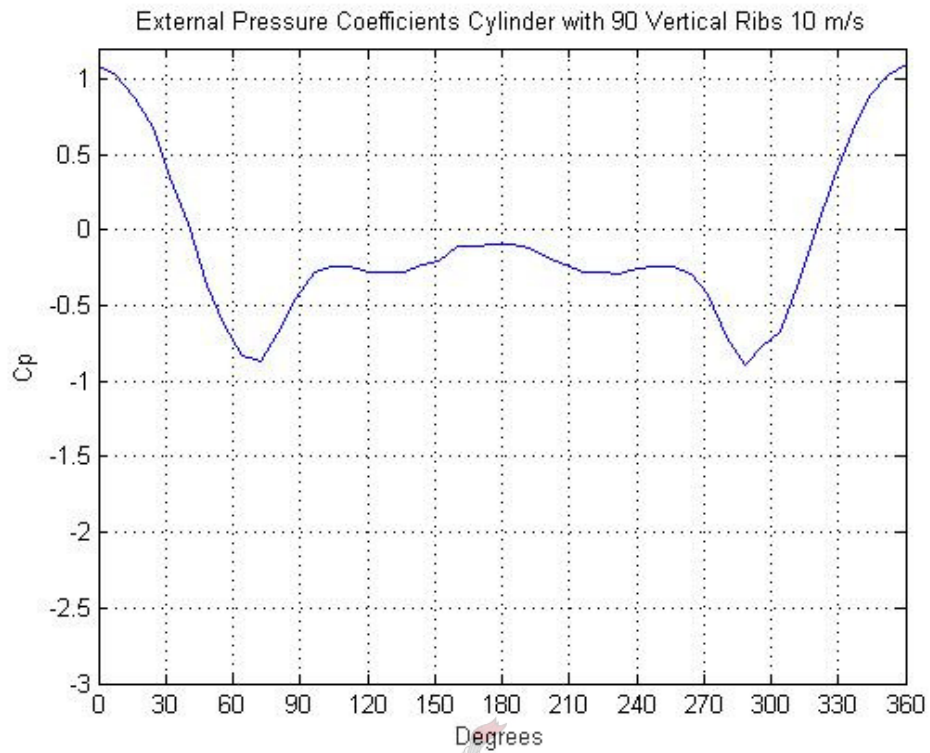


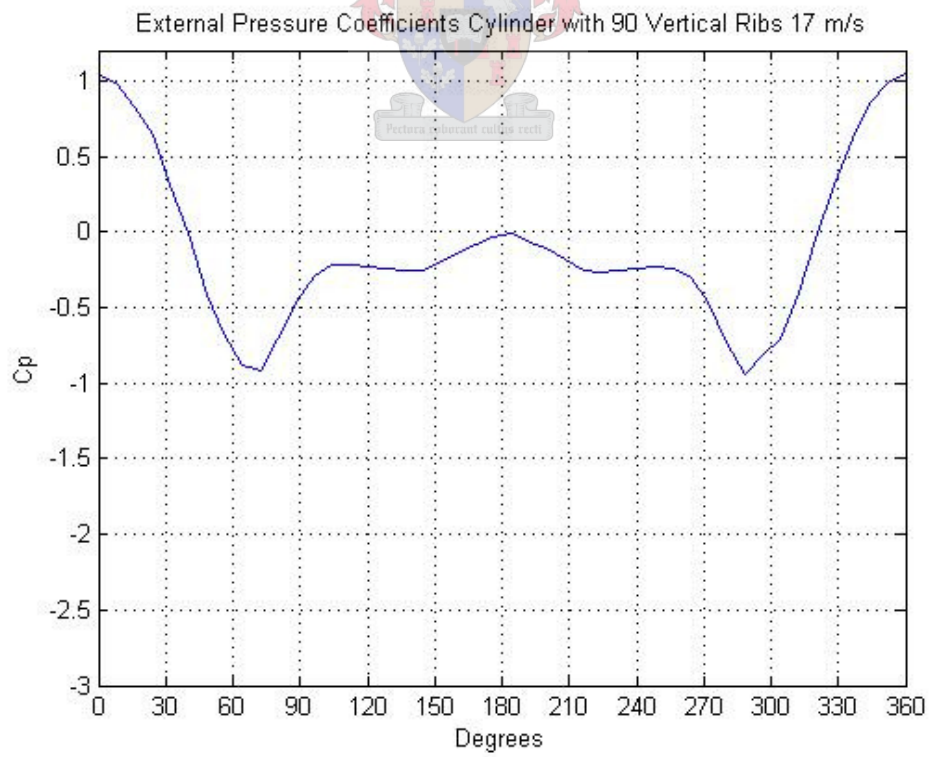
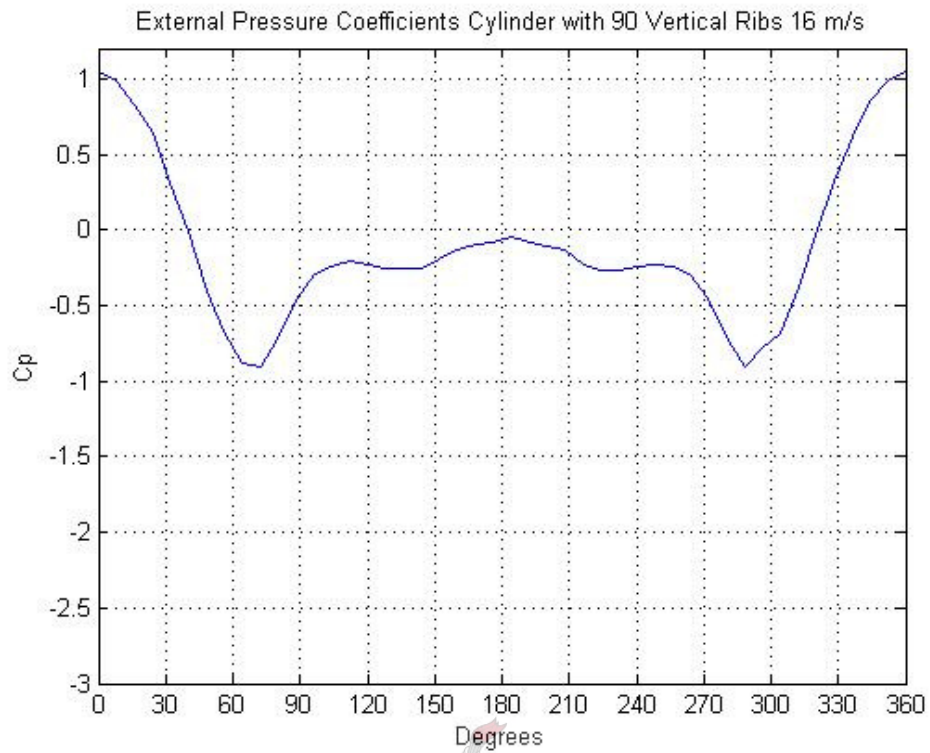


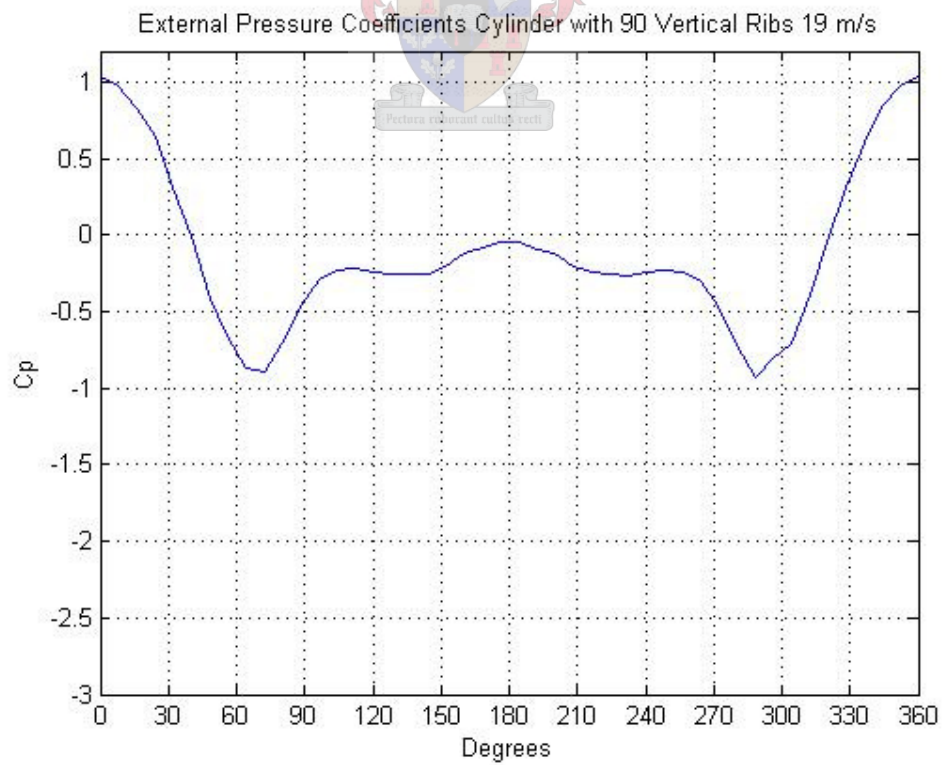
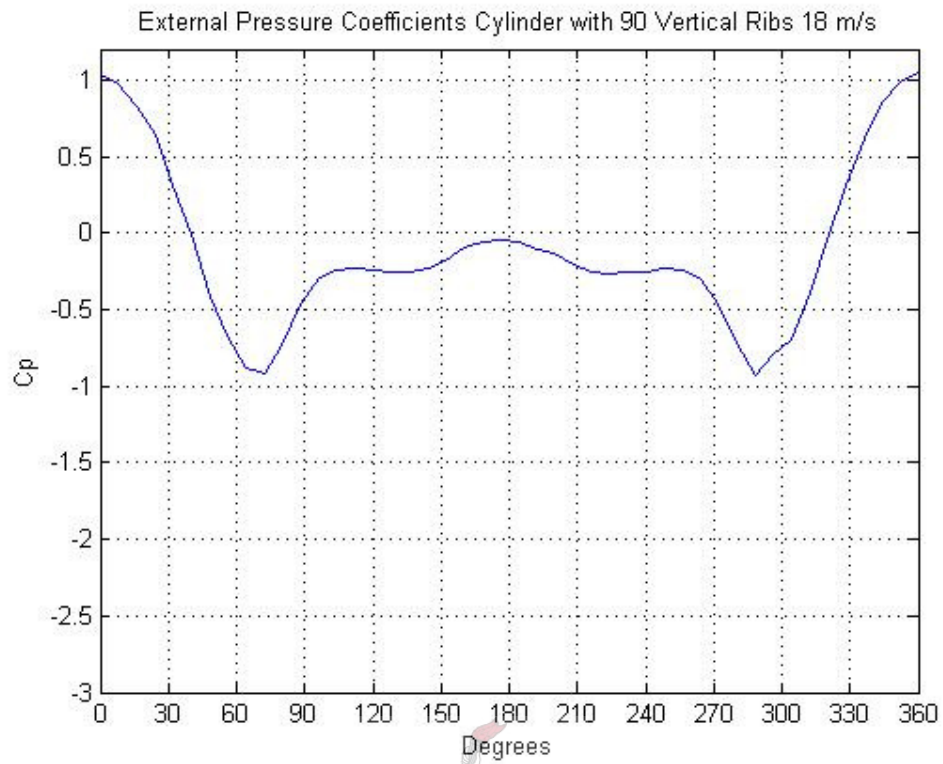


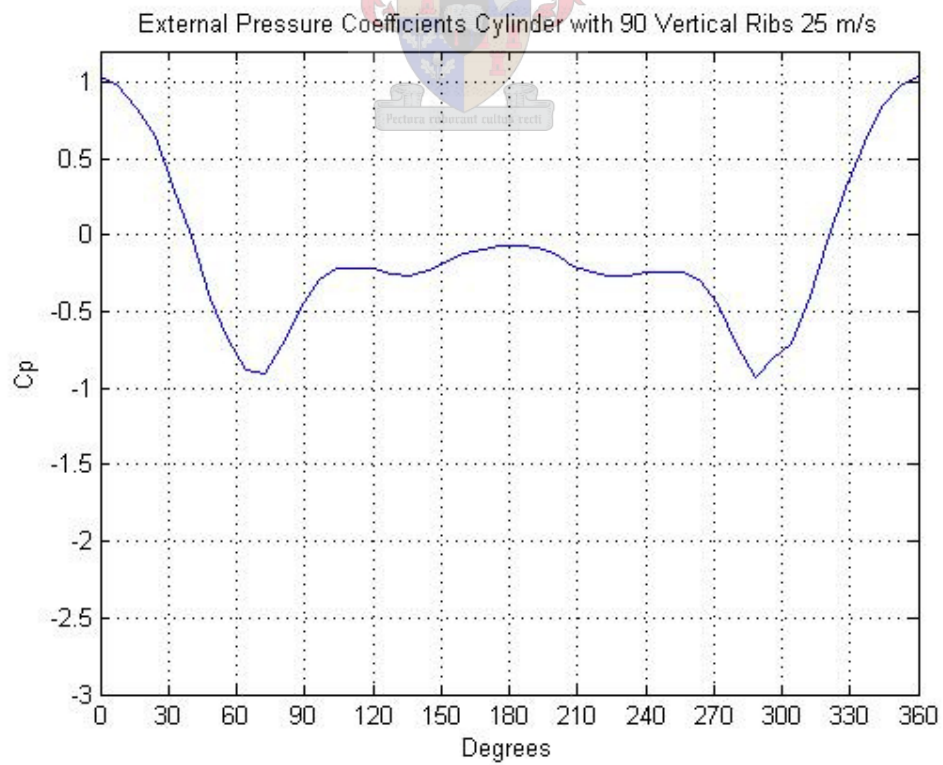
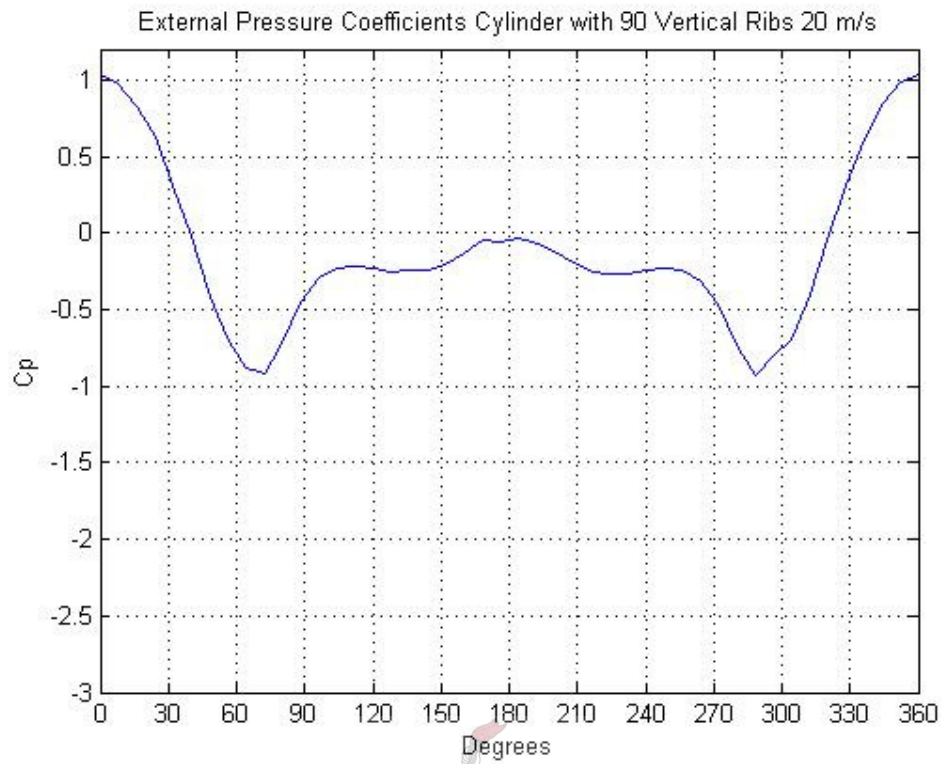
B.3 External Pressure Coefficients for the Cylinder with 90 Vertical Ribs for all Wind Speeds











APPENDIX C: DETAILED REPORT OF WIND TUNNEL TESTING: UNIVERSITY OF STELLENBOSCH

C.1 The Wind Tunnel

The Wind Tunnel at the Department of Mechanical Engineering of the University of Stellenbosch was used. This suction Wind Tunnel was chosen above the smaller blowing Wind Tunnel due to the size of its test section and the range of velocities (up to 100 m/s) which can be generated.

The initial inlet of the Wind Tunnel has an area 13.3 m^2 which has recently been decreased to an area of 10.6 m^2 due to the construction of a wooden ramp. This can be seen in Figure C1.1.



Figure C1.1: Initial Inlet with Wooden Ramp

Air flow is turned through 90 degrees by means of aluminum guide vanes upstream of the inlet. These guide vanes can be seen in the background of Figure C1.1 and in closer detail in Figure C1.2.



Figure C1.2: Guide Vains Turn wind flow by 90 degrees

Air then flows through a mesh screen (Figure C1.3) which serves to break up any boundary layers and ensure uniform flow into the nozzle section of the Wind Tunnel. The mesh also prevents any foreign objects from entering the test section. The nozzle section from the exterior is shown in Figure C1.4. The inlet of the nozzle has an area of 12.3 m^2 and a compression ratio of 9.4.



Figure C1.3: Mesh to Ensure Uniform Flow

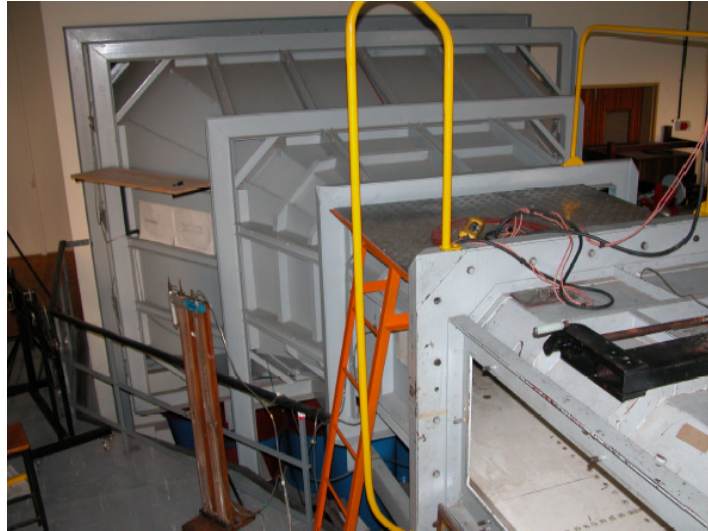


Figure C1.4: Exterior View of the Nozzle and Part of the Test Section

The test section has a height of 1 m, width of 1.425 m and length of 1.9 m and can be seen in Figure C1.5.



Figure C1.5: Test Section

The diffuser diverges at an angle of 6.02 degrees vertically and 4.46 degrees horizontally over a length of 15.35 m. This can be seen in Figure C1.6.



Figure C1.6: Diffuser Section of Length 15.35 m

The axial fan (Figure C1.7) of diameter 2.7 m is connected to a 373 kW motor that operates at a constant speed. The wind speeds generated in the test section are regulated by opening and closing the gates in front of the fan. These gates can be seen in the background of Figure C1.6. A second diffuser is situated vertically downstream of the fan.



Figure C1.7: 2.7 m Diameter Suction Fan

A boundary layer is present in the test section. The boundary layer test was done using a pitot tube connected to a Betz manometer. Readings were taken from 20 mm above the

floor of the test section in increments of 10 mm. The cross wind speed used for this test was 60 m/s. Two tests were conducted and an average of these was taken. The results are shown graphically in Figure C1.8 and it can be seen that the boundary layer in the test section is approximately 50 mm high. The end of the boundary layer is taken as the point where the measured velocity is 99% of the free stream velocity.

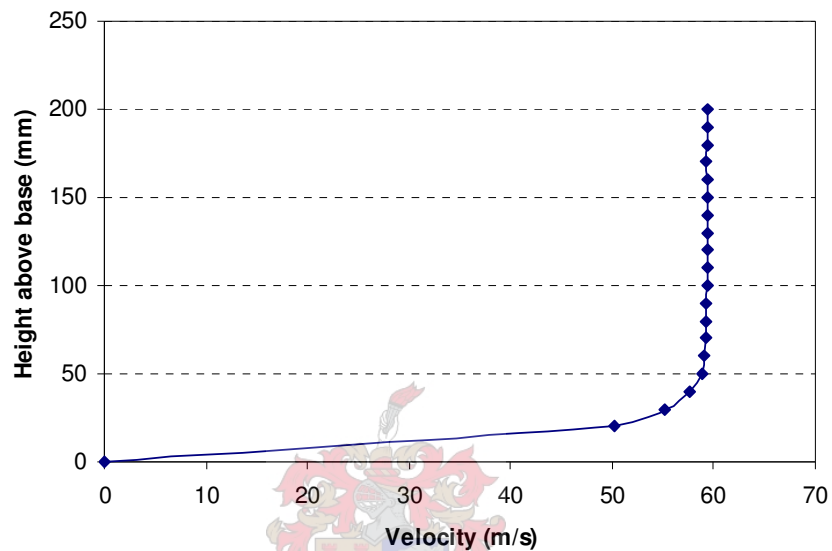


Figure C1.8: Wind Tunnel Test Section Velocity Profile

The general layout of the wind tunnel is depicted in Figure C1.9.

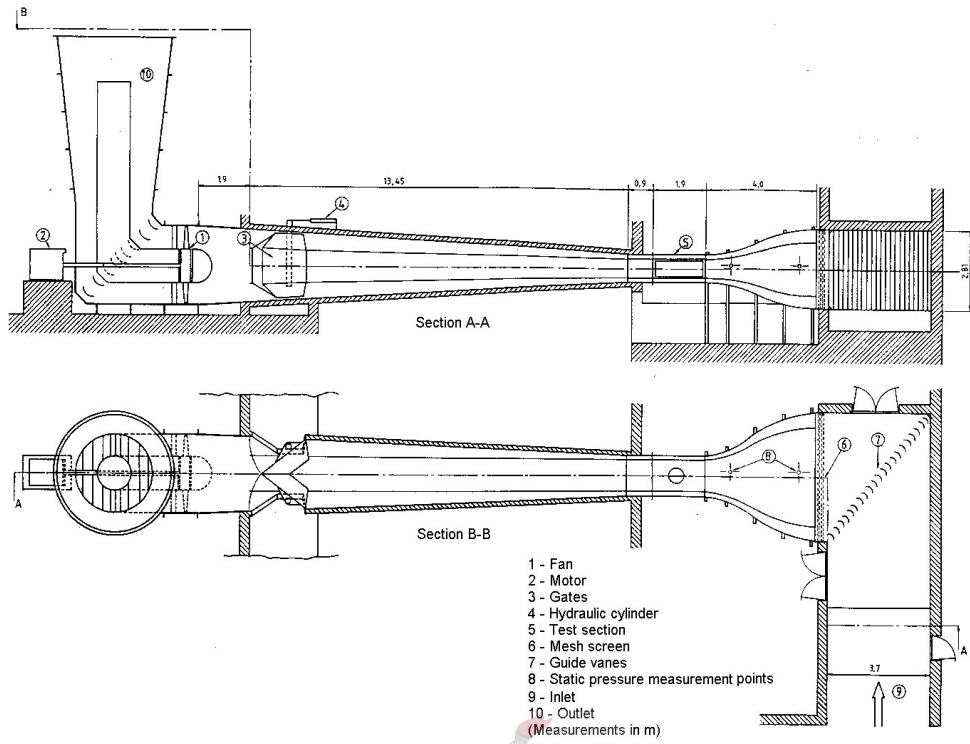
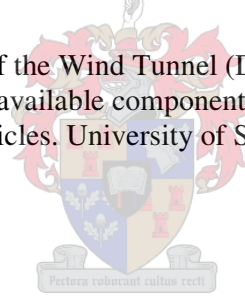


Figure C1.9: General Layout of the Wind Tunnel (Du Buisson, J.J. (1988). The effectiveness of commercially available components used to decrease the aerodynamic drag force on heavy motor vehicles. University of Stellenbosch)



C.2 Load Cell Balance

A one directional load cell balance was used in order to measure the total drag force acting on the cylinders. The load cell balance can be seen schematically in Figure C2.1.

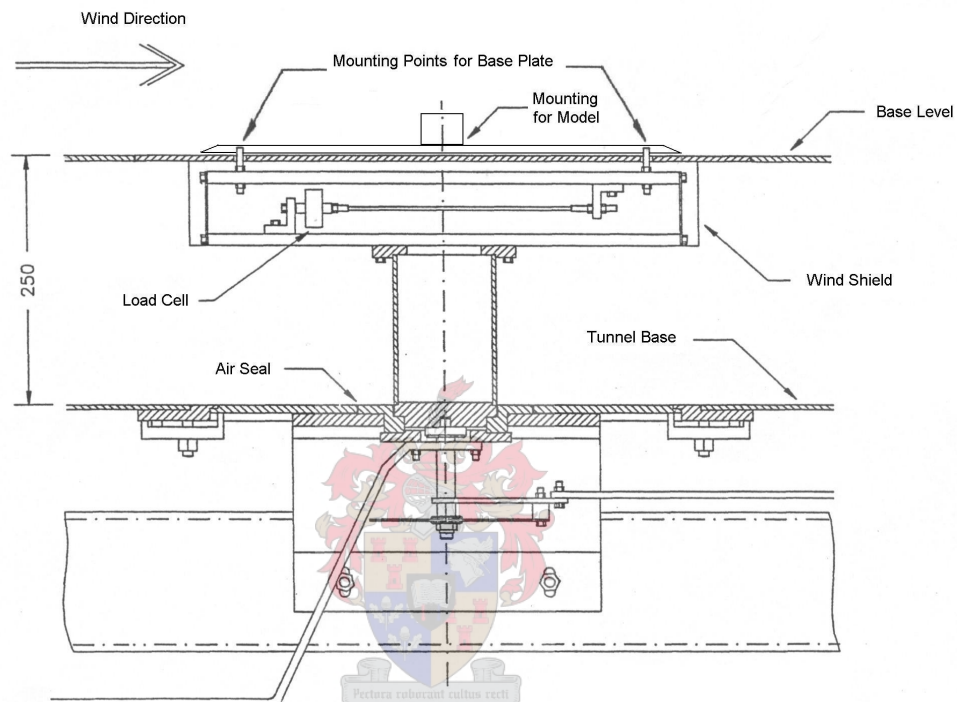


Figure C2.1: Load Cell Balance

The balance is isolated from the test section so that no vibrations from the test section can be transferred to the balance. The balance only detects force in the direction of the wind and can measure a total force of up to 300 N. Only the model is subjected to the free stream wind while the entire balance is shielded.

The load cell was calibrated by applying a series of incremental known forces to the load cell. The calibration value of the balance is 150.927 N per 1 mV/V. The linearity of this is shown in Figure C2.2.

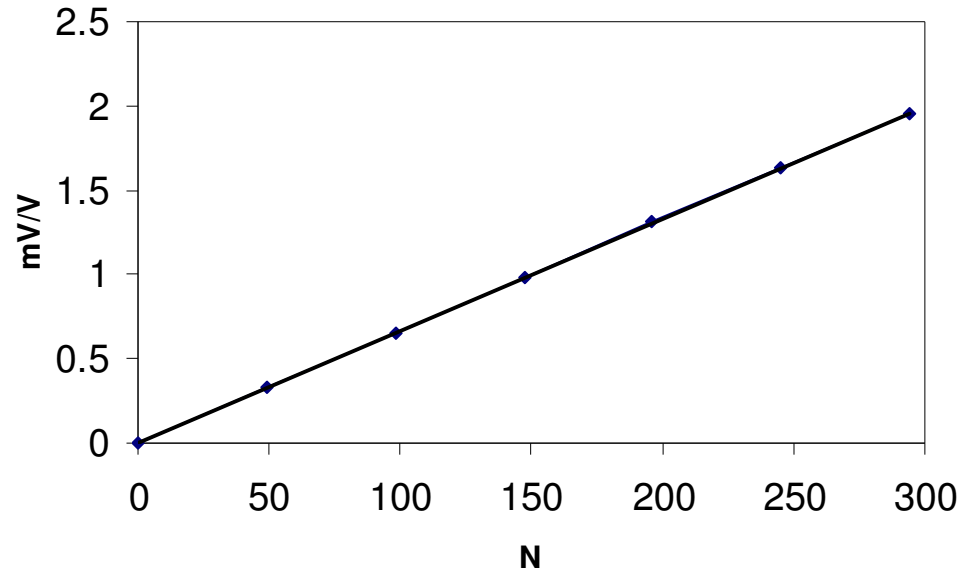
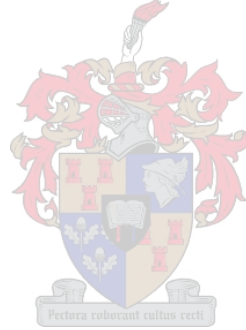


Figure C2.2: Linearity of the Load Cell Balance



C.3 Data Acquisition

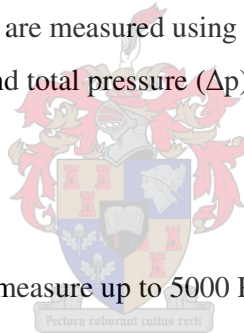
The mV/V reading from the load cell is fed through a Spider 8 data acquisition apparatus to the Computer. The computer program Catman 4.5 is used to convert this mV reading into a force (N) reading using the calibration value. This force (F_d) reading is then used to calculate the respective drag coefficient (C_d).

$$C_d = \frac{F_d}{0.5 \rho v^2 A}$$

with ρ = density of air
 v = wind speed
 A = frontal area of cylinder

The respective wind speeds (v) are measured using a Betz manometer by means of the difference between the static and total pressure (Δp) in the wind tunnel test section.

$$\Delta p = 0.5 \times \rho \times v^2$$



The Betz manometer can only measure up to 5000 Pa which is equivalent to 90 m/s windspeed.

The air temperature (T) is measured for each test and the respective air density (ρ) is used for the calculations.

$$T = 19^\circ\text{C} \quad : \quad \rho = 1.209 \text{ kg/m}^3$$

$$T = 20^\circ\text{C} \quad : \quad \rho = 1.205 \text{ kg/m}^3$$

The drag coefficient is then plotted against Reynolds number (R_e).

$$R_e = \frac{vD}{\nu}$$

with v = crosswind velocity
 D = diameter of cylinder
 ν = kinematic viscosity of air

APPENDIX D: WIND TUNNEL TEST

RESULTS: UNIVERSITY OF STELLENBOSCH

D.1 Cylinder 1: Smooth

Table D.1.1: Drag Coefficient Results for Cylinder 1: Smooth

<u>TEST 1:</u>					<u>TEST 2:</u>				
<u>Wind Tunnel Properties:</u>					<u>Wind Tunnel Properties:</u>				
(20°C)					(19°C)				
Air density (ρ):	1.205	kg/m ³			Air density (ρ):	1.209	kg/m ³		
Kinematic viscosity (ν):	1.51E-05	m ² /s			Kinematic viscosity (ν):	1.51E-05	m ² /s		
<u>Smooth Cylinder:</u>					<u>Smooth Cylinder:</u>				
Diameter:	0.11	m			Diameter:	0.11	m		
Height:	0.285	m			Height:	0.285	m		
Fontal Area:	0.0314	m ²			Fontal Area:	0.0314	m ²		
v	delta	F_d	C_d	Re	v	delta	F_d	C_d	Re
m/s	Pa	N			m/s	Pa	N		
4.07	10	0.185	0.590	2.97E+04	4.07	10	0.200	0.638	2.96E+04
6.04	22	0.525	0.761	4.40E+04	5.75	20	0.475	0.758	4.19E+04
7.06	30	0.730	0.776	5.14E+04	7.04	30	0.760	0.808	5.13E+04
9.98	60	1.550	0.824	7.26E+04	9.96	60	1.550	0.824	7.25E+04
12.49	94	2.480	0.842	9.09E+04	12.54	95	2.500	0.839	9.13E+04
15.24	140	3.780	0.861	1.11E+05	15.22	140	3.750	0.854	1.11E+05
17.28	180	4.850	0.859	1.26E+05	17.26	180	4.800	0.851	1.26E+05
19.96	240	6.500	0.864	1.45E+05	19.93	240	6.400	0.851	1.45E+05
22.31	300	8.150	0.867	1.62E+05	22.28	300	7.750	0.824	1.62E+05
25.11	380	10.300	0.865	1.83E+05	25.07	380	9.500	0.797	1.83E+05
27.93	470	12.650	0.859	2.03E+05	27.59	460	11.200	0.777	2.01E+05
29.94	540	14.500	0.857	2.18E+05	29.89	540	12.800	0.756	2.18E+05
32.59	640	17.000	0.847	2.37E+05	32.54	640	14.400	0.718	2.37E+05
35.05	740	19.400	0.836	2.55E+05	34.99	740	15.000	0.647	2.55E+05
37.78	860	22.000	0.816	2.75E+05	37.50	850	15.000	0.563	2.73E+05
40.12	970	18.750	0.617	2.92E+05	40.06	970	15.100	0.497	2.92E+05
42.53	1090	20.100	0.588	3.10E+05	42.46	1090	15.500	0.454	3.09E+05
44.81	1210	22.000	0.580	3.26E+05	44.92	1220	15.650	0.409	3.27E+05
47.51	1360	24.000	0.563	3.46E+05	47.43	1360	17.600	0.413	3.45E+05
49.90	1500	16.500	0.351	3.63E+05	49.81	1500	20.000	0.425	3.63E+05
52.65	1670	18.500	0.353	3.83E+05	52.40	1660	23.000	0.442	3.81E+05
55.11	1830	20.800	0.363	4.01E+05	55.17	1840	26.000	0.451	4.02E+05
57.47	1990	23.500	0.377	4.18E+05	57.01	1965	28.400	0.461	4.15E+05

v m/s	Δp Pa	F_d N	C_d	Re	v m/s	Δp Pa	F_d N	C_d	Re
60.01	2170	25.900	0.381	4.37E+05	59.64	2150	31.600	0.469	4.34E+05
62.45	2350	28.500	0.387	4.55E+05	62.22	2340	35.000	0.477	4.53E+05
65.06	2550	31.000	0.388	4.74E+05	65.33	2580	39.500	0.488	4.76E+05
67.56	2750	37.000	0.429	4.92E+05	67.57	2760	43.000	0.497	4.92E+05
69.97	2950	40.000	0.433	5.09E+05	69.74	2940	47.300	0.513	5.08E+05
72.54	3170	44.500	0.448	5.28E+05	72.42	3170	52.000	0.523	5.27E+05
75.01	3390	48.500	0.456	5.46E+05	74.66	3370	56.000	0.530	5.44E+05
77.51	3620	52.000	0.458	5.64E+05	77.60	3640	61.000	0.535	5.65E+05
80.04	3860	58.250	0.481	5.83E+05	79.91	3860	64.000	0.529	5.82E+05
82.49	4100	63.000	0.490	6.01E+05	82.46	4110	68.500	0.532	6.00E+05
85.26	4380	70.500	0.513	6.21E+05	84.63	4330	73.000	0.538	6.16E+05
87.19	4580	75.000	0.522	6.35E+05	87.04	4580	77.000	0.536	6.34E+05

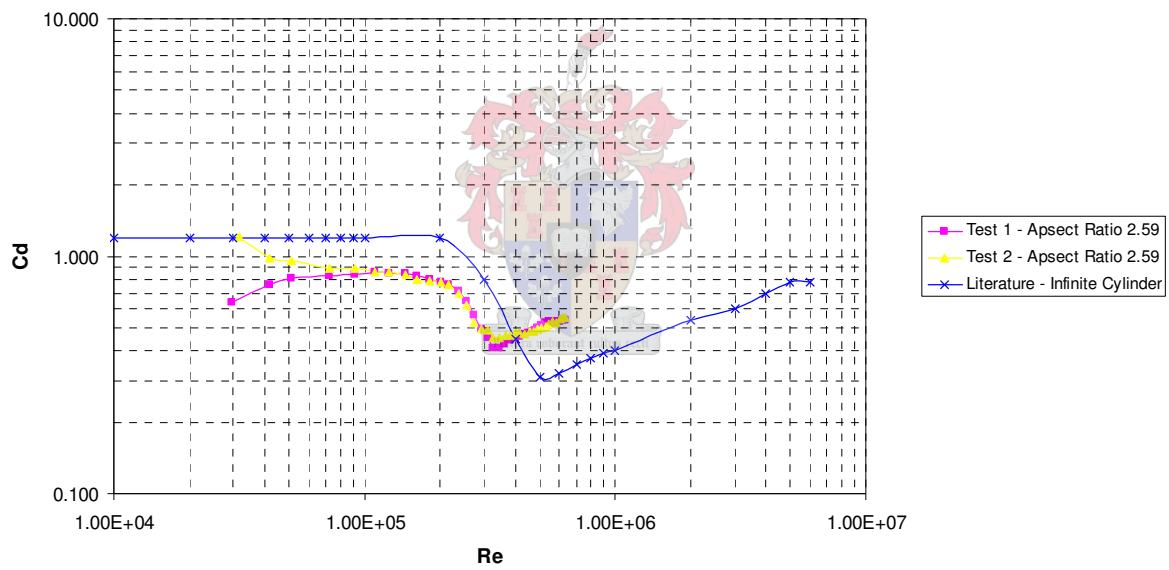


Figure D.1.1: Drag Coefficient of a Smooth Cylinder of Aspect Ratio 2.59

D.2 Cylinder 2: Small Vertical Ribs

Table D.1.2: Drag Coefficient Results for Cylinder 2: Small Vertical Ribs

TEST 1:					TEST 2:				
Wind Tunnel Properties:					Wind Tunnel Properties:				
(20°C)					(19°C)				
Air density (ρ):	1.205 kg/m ³				Air density (ρ):	1.209 kg/m ³			
Kinematic viscosity (ν):	1.51E-05 m ² /s				Kinematic viscosity (ν):	1.51E-05 m ² /s			
Smooth Cylinder:					Smooth Cylinder:				
Diameter:	0.12 m				Diameter:	0.12 m			
Height:	0.285 m				Height:	0.285 m			
Fontal Area:	0.0342 m ²				Fontal Area:	0.0342 m ²			
v	δ	F_d	C_d	Re	v	δ	F_d	C_d	Re
m/s	Pa	N			m/s	Pa	N		
4.07	10	0.265	0.775	3.24E+04	4.27	11	0.235	0.625	3.39E+04
5.76	20	0.525	0.768	4.58E+04	5.75	20	0.455	0.665	4.57E+04
7.06	30	0.760	0.741	5.60E+04	7.04	30	0.685	0.668	5.59E+04
9.98	60	1.475	0.719	7.93E+04	9.96	60	1.400	0.682	7.91E+04
12.56	95	2.370	0.729	9.97E+04	12.54	95	2.350	0.723	9.96E+04
15.24	140	3.500	0.731	1.21E+05	15.22	140	3.490	0.729	1.21E+05
17.28	180	4.500	0.731	1.37E+05	17.26	180	4.500	0.731	1.37E+05
19.96	240	6.100	0.743	1.59E+05	19.93	240	6.050	0.737	1.58E+05
22.31	300	7.600	0.741	1.77E+05	22.28	300	7.650	0.746	1.77E+05
25.11	380	9.700	0.746	1.99E+05	25.07	380	9.750	0.750	1.99E+05
27.63	460	11.750	0.747	2.19E+05	27.59	460	11.750	0.747	2.19E+05
29.94	540	13.750	0.745	2.38E+05	29.89	540	13.750	0.745	2.37E+05
32.59	640	16.500	0.754	2.59E+05	32.54	640	16.500	0.754	2.58E+05
35.05	740	19.000	0.751	2.78E+05	34.99	740	19.000	0.751	2.78E+05
37.78	860	22.300	0.758	3.00E+05	37.50	850	22.000	0.757	2.98E+05
40.12	970	25.000	0.754	3.19E+05	40.06	970	25.000	0.754	3.18E+05
42.53	1090	28.100	0.754	3.38E+05	42.66	1100	28.500	0.758	3.39E+05
45.00	1220	31.500	0.755	3.57E+05	44.92	1220	31.500	0.755	3.57E+05
47.51	1360	35.200	0.757	3.77E+05	47.43	1360	35.500	0.763	3.77E+05
49.90	1500	39.000	0.760	3.96E+05	49.81	1500	39.100	0.762	3.96E+05
52.49	1660	43.000	0.757	4.17E+05	52.40	1660	43.300	0.763	4.16E+05
54.96	1820	47.500	0.763	4.36E+05	54.87	1820	47.500	0.763	4.36E+05
57.47	1990	52.000	0.764	4.56E+05	57.38	1990	52.000	0.764	4.56E+05
60.01	2170	56.800	0.765	4.77E+05	59.91	2170	57.000	0.768	4.76E+05
62.32	2340	61.000	0.762	4.95E+05	62.35	2350	61.500	0.765	4.95E+05
65.06	2550	67.000	0.768	5.17E+05	64.95	2550	67.000	0.768	5.16E+05
67.56	2750	71.500	0.760	5.37E+05	67.45	2750	72.000	0.766	5.36E+05
69.85	2940	77.000	0.766	5.55E+05	69.86	2950	78.000	0.773	5.55E+05
72.76	3190	84.000	0.770	5.78E+05	72.42	3170	84.300	0.778	5.75E+05
75.01	3390	90.000	0.776	5.96E+05	74.89	3390	90.500	0.781	5.95E+05
77.51	3620	96.000	0.775	6.16E+05	77.38	3620	97.000	0.783	6.15E+05
80.04	3860	102.500	0.776	6.36E+05	79.91	3860	104.000	0.788	6.35E+05
82.29	4080	110.000	0.788	6.54E+05	82.36	4100	111.000	0.792	6.54E+05

v m/s	Δp Pa	F_d N	C_d	Re	v m/s	Δp Pa	F_d N	C_d	Re
84.73	4325	116.500	0.788	6.73E+05	84.83	4350	118.000	0.793	6.74E+05
87.19	4580	122.500	0.782	6.92E+05	87.23	4600	125.000	0.795	6.93E+05

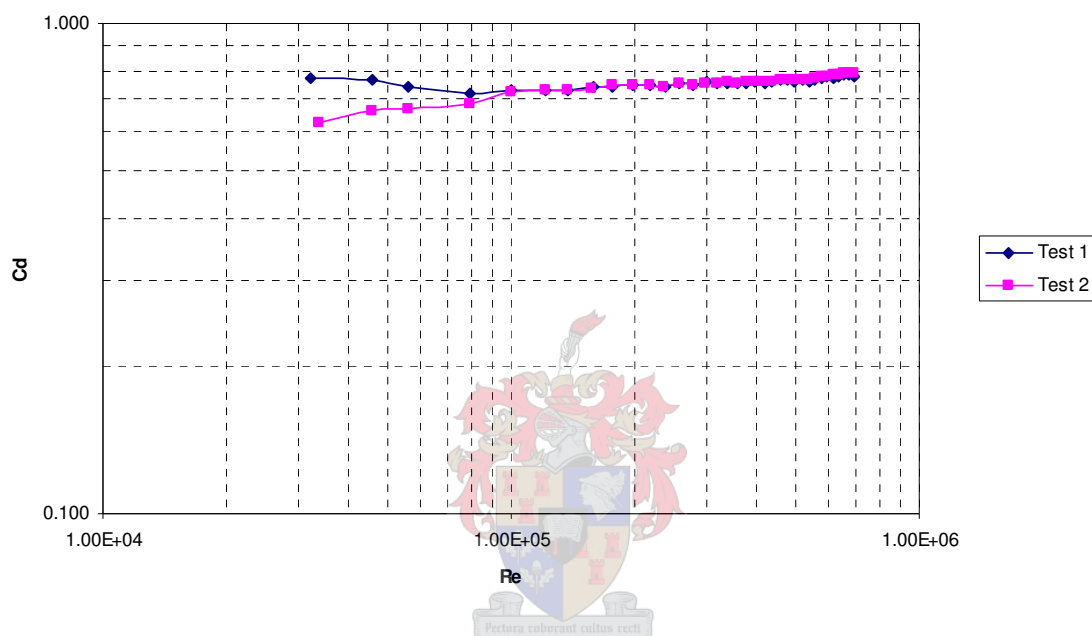


Figure D.1.2: Drag Coefficient of a Cylinder with Small Vertical Ribs

D.3 Cylinder 3: Large Vertical Rib

Table D.1.3: Drag Coefficient Results for Cylinder 3: Large Vertical Rib

TEST 1:					TEST 2:				
Wind Tunnel					Wind Tunnel				
Properties:					Properties:				
(20 °C)					(19 °C)				
Air density (ρ):	1.205 kg/m ³				Air density (ρ):	1.209 kg/m ³			
Kinematic viscosity (ν):	1.51E-05 m ² /s				Kinematic viscosity (ν):	1.51E-05 m ² /s			
Smooth Cylinder:					Smooth Cylinder:				
Diameter:	0.13 m				Diameter:	0.13 m			
Height:	0.285 m				Height:	0.285 m			
Fontal Area:	0.03705 m ²				Fontal Area:	0.03705 m ²			
v	delta	Fd	Cd	Re	v	delta	Fd	Cd	Re
m/s	p	N			m/s	Pa	N		
4.07	10	0.265	0.715	3.51E+04	4.07	10	0.195	0.526	3.50E+04
5.76	20	0.600	0.810	4.96E+04	5.75	20	0.500	0.675	4.95E+04
7.06	30	0.880	0.792	6.07E+04	7.04	30	0.800	0.720	6.06E+04
9.98	60	1.840	0.828	8.59E+04	10.05	61	1.770	0.783	8.64E+04
12.49	94	2.850	0.818	1.07E+05	12.54	95	2.760	0.784	1.08E+05
15.24	140	4.260	0.821	1.31E+05	15.22	140	4.200	0.810	1.31E+05
17.28	180	5.500	0.825	1.49E+05	17.26	180	5.450	0.817	1.48E+05
19.96	240	7.400	0.832	1.72E+05	19.93	240	7.330	0.824	1.71E+05
22.31	300	9.250	0.832	1.92E+05	22.28	300	9.200	0.828	1.92E+05
25.11	380	11.750	0.835	2.16E+05	25.07	380	11.650	0.827	2.16E+05
27.63	460	14.200	0.833	2.38E+05	27.59	460	14.125	0.829	2.37E+05
29.94	540	16.500	0.825	2.58E+05	30.14	549	16.750	0.823	2.59E+05
32.59	640	19.750	0.833	2.80E+05	32.54	640	19.700	0.831	2.80E+05
35.05	740	22.950	0.837	3.02E+05	34.99	740	23.000	0.839	3.01E+05
37.56	850	26.300	0.835	3.23E+05	37.50	850	26.400	0.838	3.23E+05
40.12	970	30.000	0.835	3.45E+05	40.06	970	30.200	0.840	3.45E+05
42.53	1090	33.750	0.836	3.66E+05	42.46	1090	34.000	0.842	3.65E+05
45.00	1220	38.000	0.841	3.87E+05	44.92	1220	38.000	0.841	3.87E+05
47.51	1360	42.600	0.845	4.09E+05	47.43	1360	42.500	0.843	4.08E+05
49.73	1490	47.000	0.851	4.28E+05	49.81	1500	47.000	0.846	4.29E+05
52.49	1660	51.900	0.844	4.52E+05	52.40	1660	51.200	0.832	4.51E+05
54.96	1820	56.000	0.830	4.73E+05	54.87	1820	56.000	0.830	4.72E+05
57.47	1990	61.500	0.834	4.94E+05	57.38	1990	61.000	0.827	4.94E+05
60.01	2170	66.800	0.831	5.16E+05	59.91	2170	67.000	0.833	5.15E+05
62.32	2340	72.600	0.837	5.36E+05	62.35	2350	73.000	0.838	5.36E+05
65.18	2560	80.000	0.843	5.61E+05	65.08	2560	80.000	0.843	5.60E+05
67.56	2750	86.000	0.844	5.81E+05	67.45	2750	86.000	0.844	5.80E+05
69.97	2950	92.500	0.846	6.02E+05	69.74	2940	92.500	0.849	6.00E+05
72.54	3170	100.000	0.851	6.24E+05	72.42	3170	100.000	0.851	6.23E+05
75.01	3390	107.500	0.856	6.45E+05	74.89	3390	108.500	0.864	6.44E+05
77.62	3630	115.000	0.855	6.68E+05	77.38	3620	116.500	0.869	6.66E+05
80.04	3860	123.000	0.860	6.89E+05	79.91	3860	125.000	0.874	6.88E+05
82.79	4130	132.500	0.866	7.12E+05	82.15	4080	132.500	0.877	7.07E+05

v m/s	Δp Pa	F_d N	C_d	Re	v m/s	Δp Pa	F_d N	C_d	Re
85.17	4370	140.000	0.865	7.33E+05	84.93	4360	142.000	0.879	7.31E+05
86.71	4530	145.000	0.864	7.46E+05	86.95	4570	148.000	0.874	7.48E+05

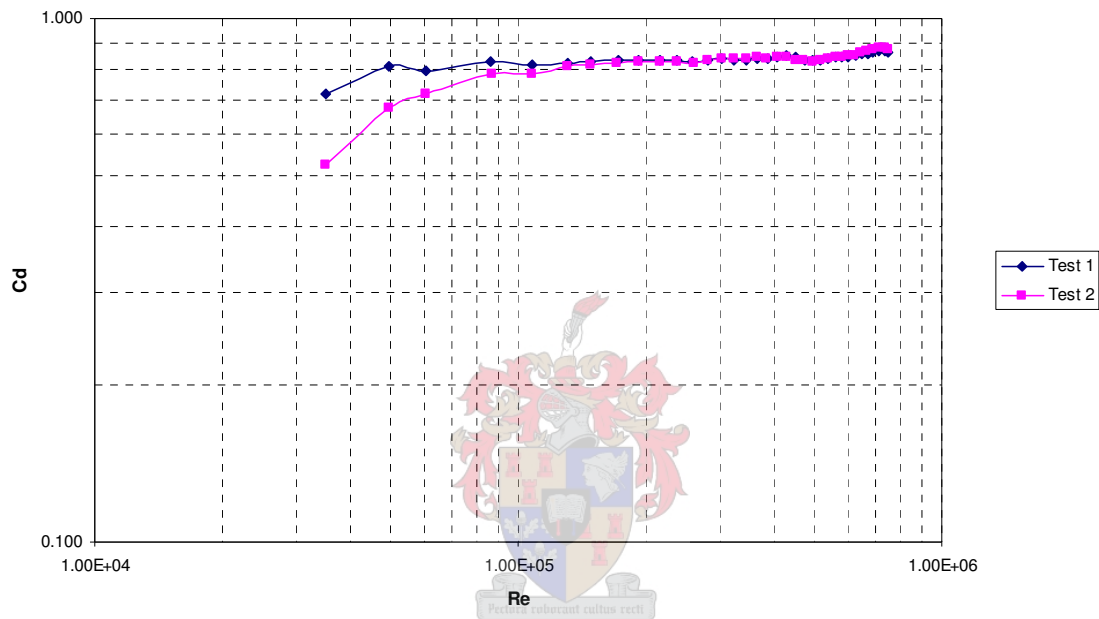


Figure D.1.3: Drag Coefficient of a Cylinder with Large Vertical Ribs

APPENDIX E: CFD RESULTS

E.1 Smooth Cylinder

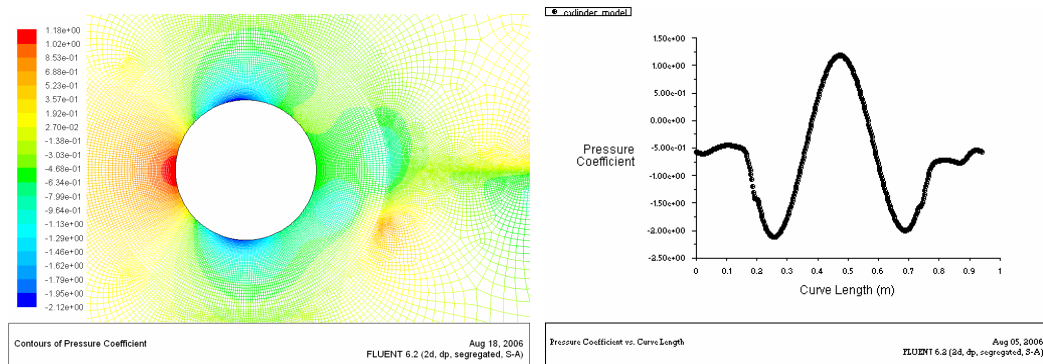


Figure E1.1: External Pressure Coefficients for 5m/s.

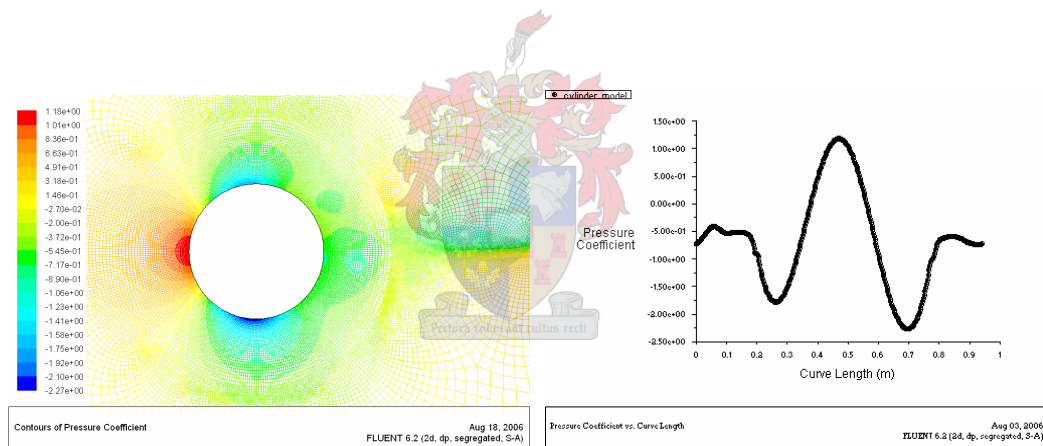


Figure E1.2: External Pressure Coefficients for 10m/s.

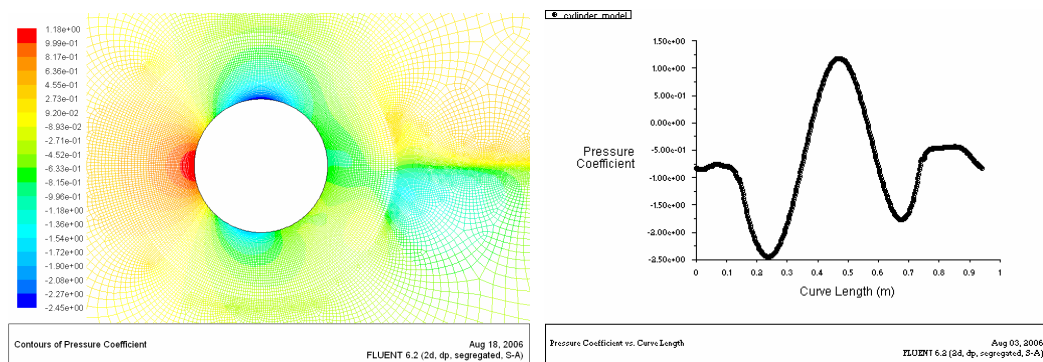


Figure E1.3: External Pressure Coefficients for 15m/s.

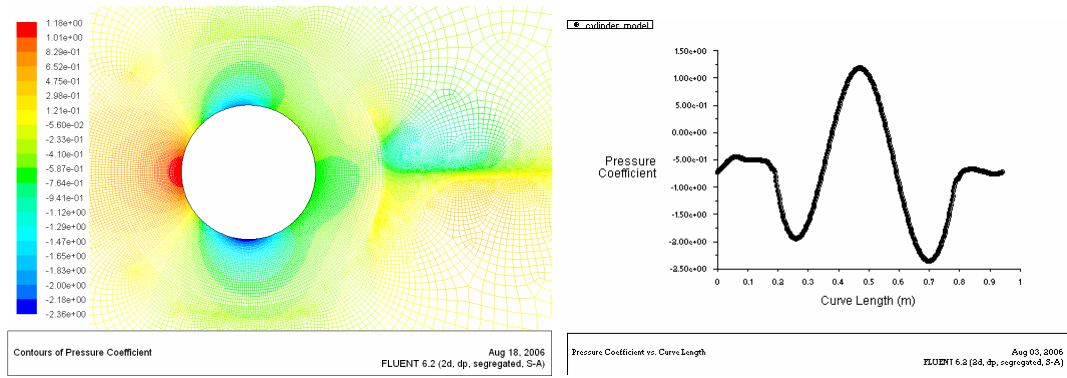


Figure E1.4: External Pressure Coefficients for 18m/s.

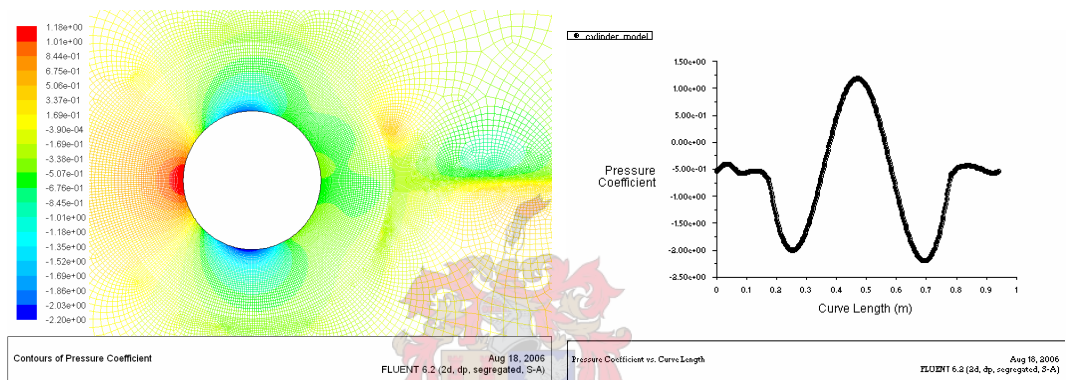


Figure E1.5: External Pressure Coefficients for 20m/s.

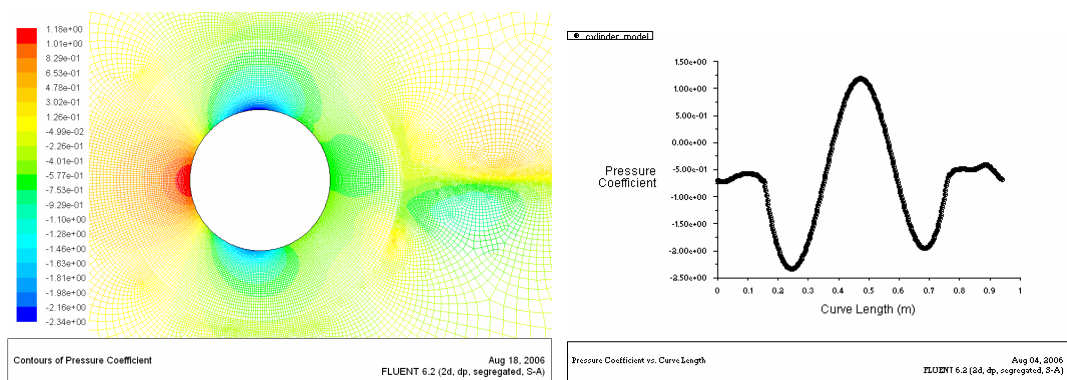


Figure E1.6: External Pressure Coefficients for 25m/s.

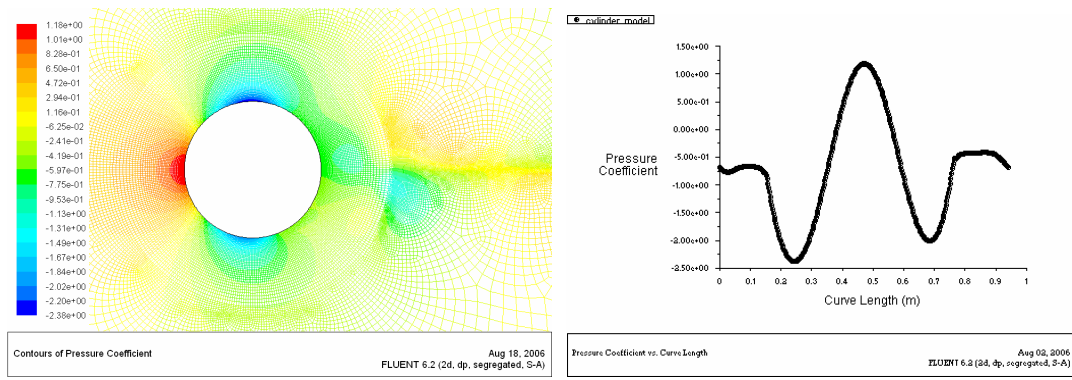


Figure E1.7: External Pressure Coefficients for 30m/s.

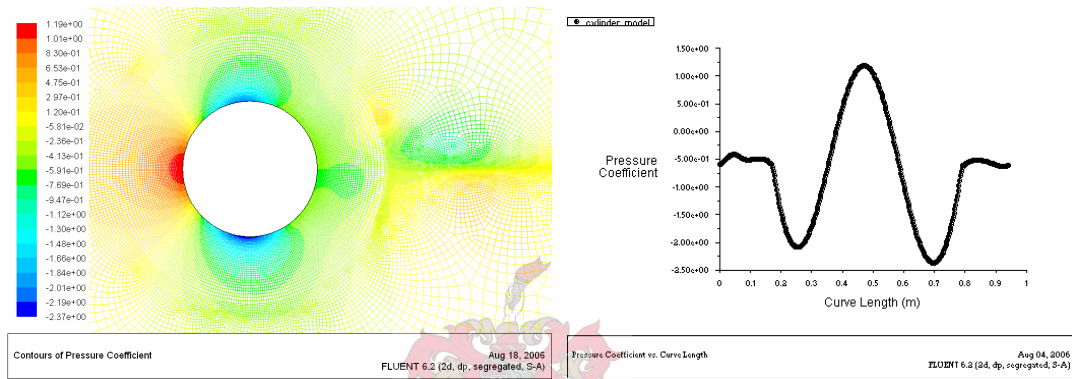


Figure E1.8: External Pressure Coefficients for 35m/s.

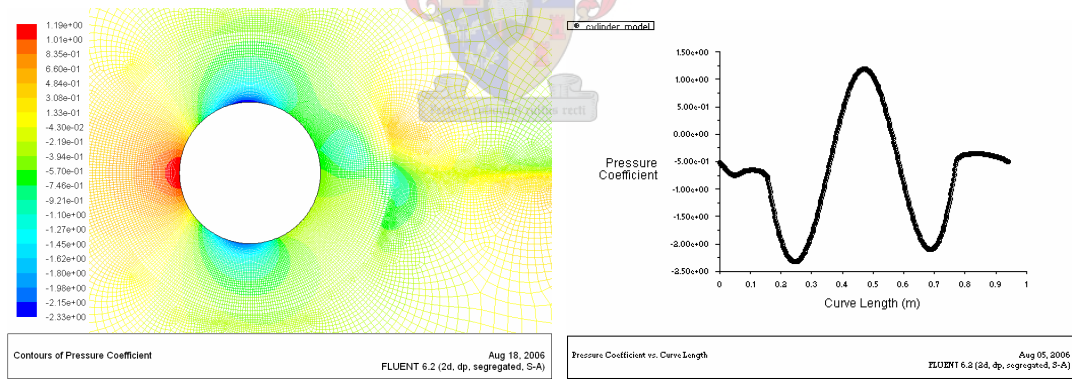


Figure E1.9: External Pressure Coefficients for 40m/s.

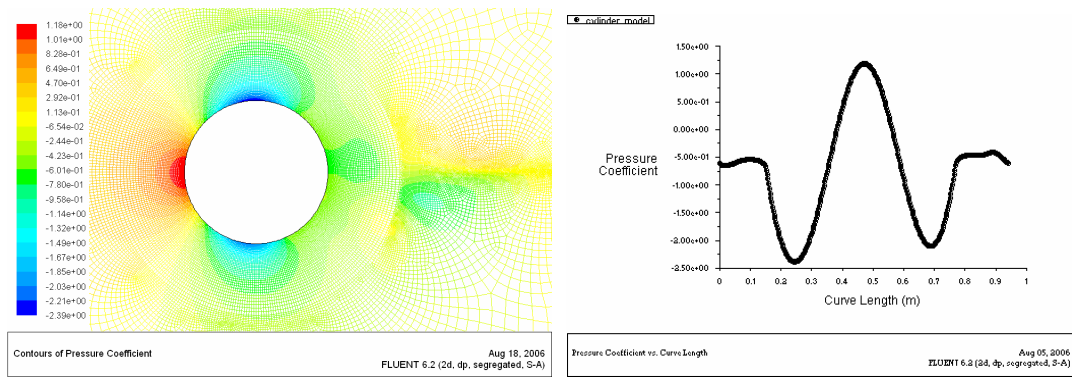


Figure E1.10: External Pressure Coefficients for 45m/s.

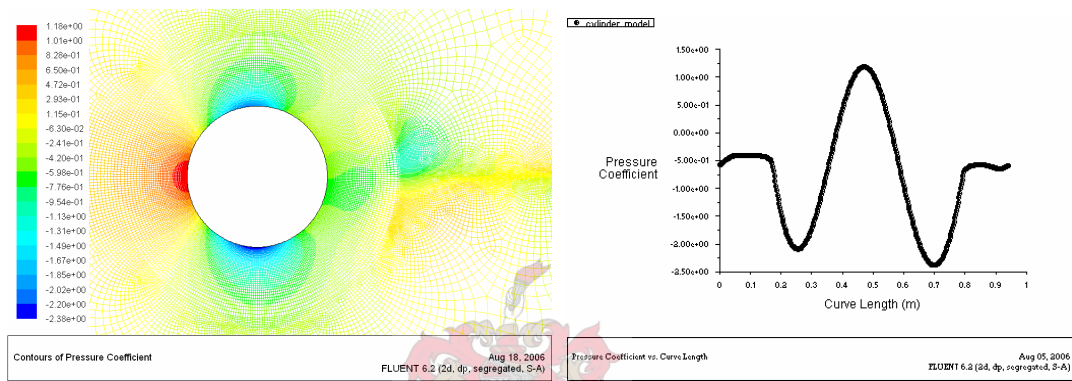


Figure E1.11: External Pressure Coefficients for 50m/s.

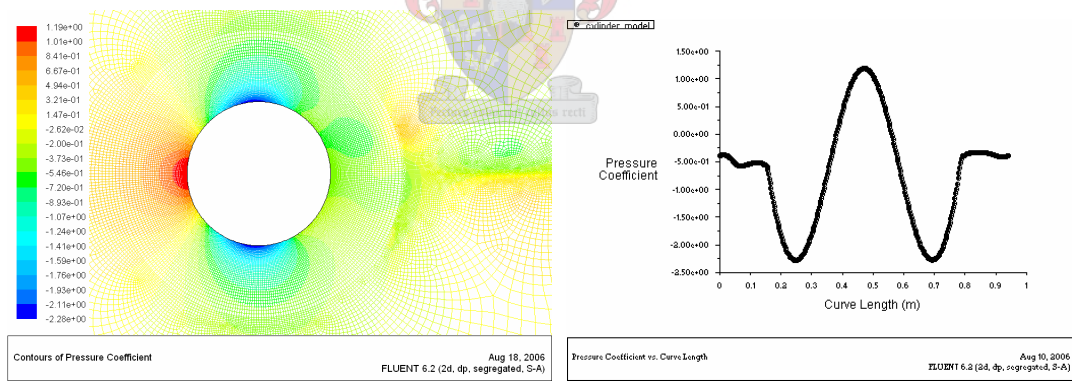


Figure E1.12: External Pressure Coefficients for 100m/s.

E.2 Cylinder with 45 Vertical Ribs

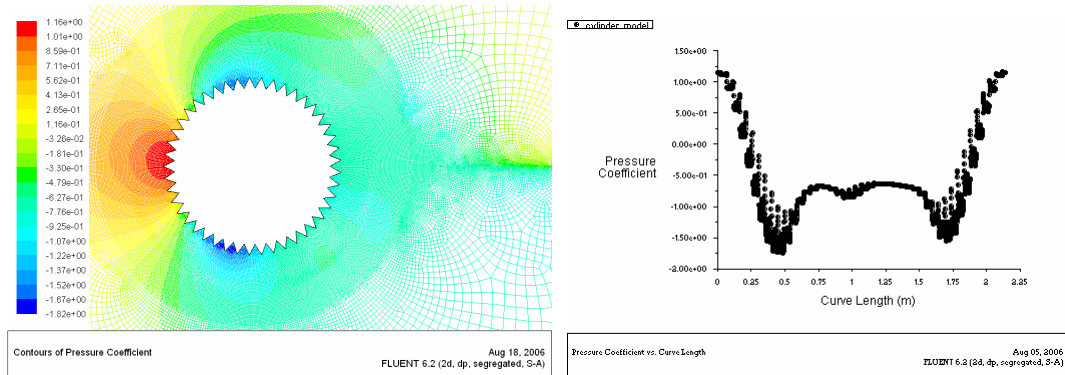


Figure E2.1: External Pressure Coefficients for 15m/s.

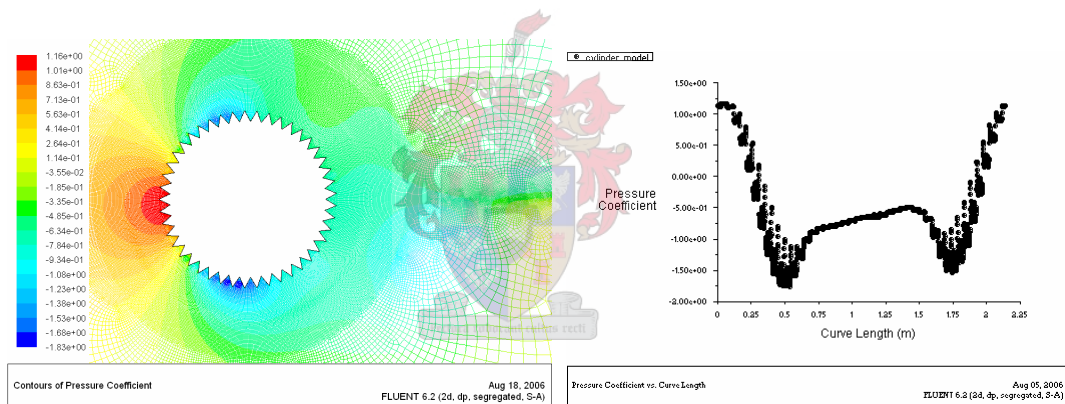


Figure E2.2: External Pressure Coefficients for 20m/s.

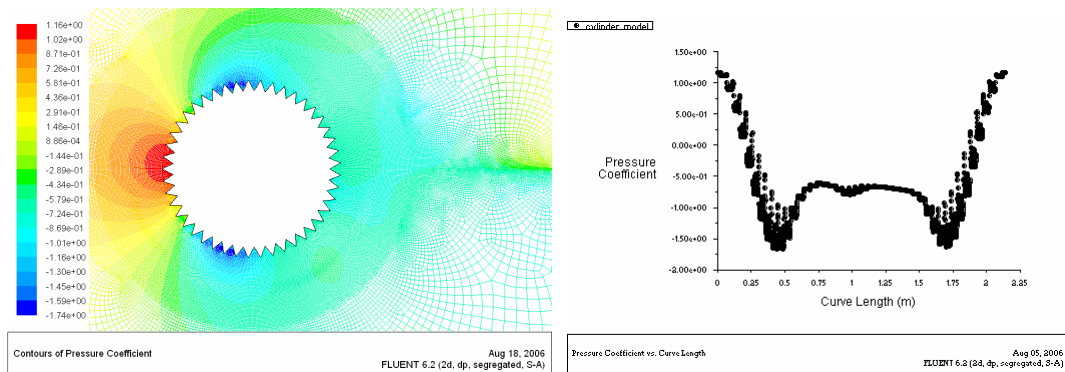


Figure E2.3: External Pressure Coefficients for 30m/s.

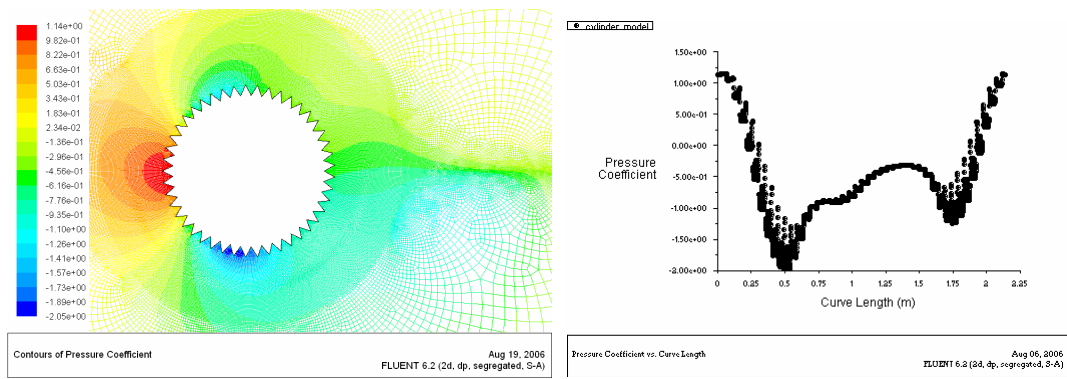


Figure E2.4: External Pressure Coefficients for 40m/s.

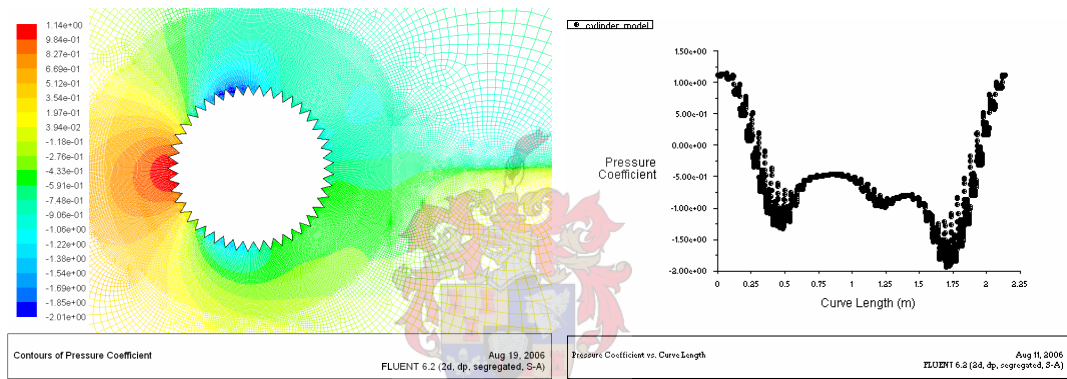


Figure E2.5: External Pressure Coefficients for 100m/s.

E.3 Cylinder with 90 Vertical Ribs

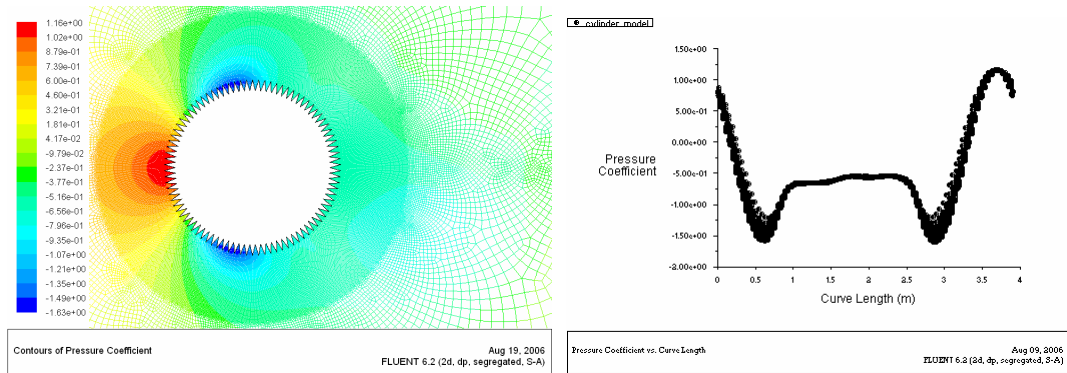


Figure E3.1: External Pressure Coefficients for 15m/s.

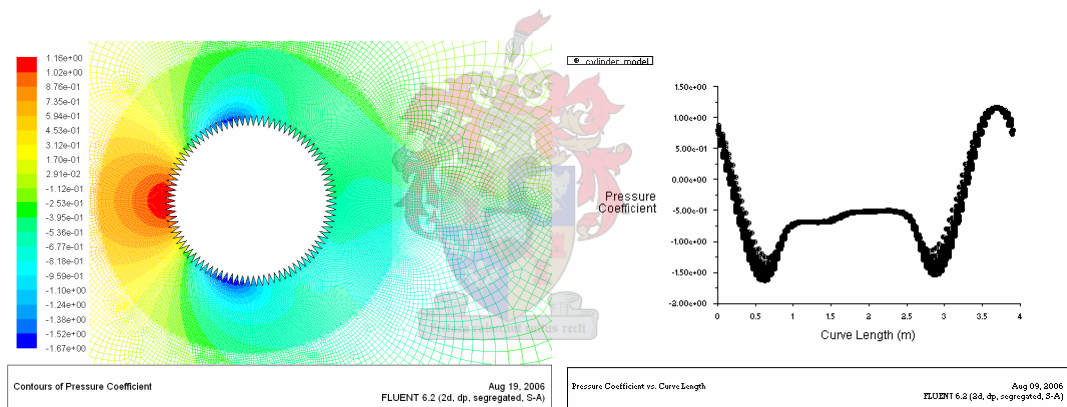


Figure E3.2: External Pressure Coefficients for 20m/s.

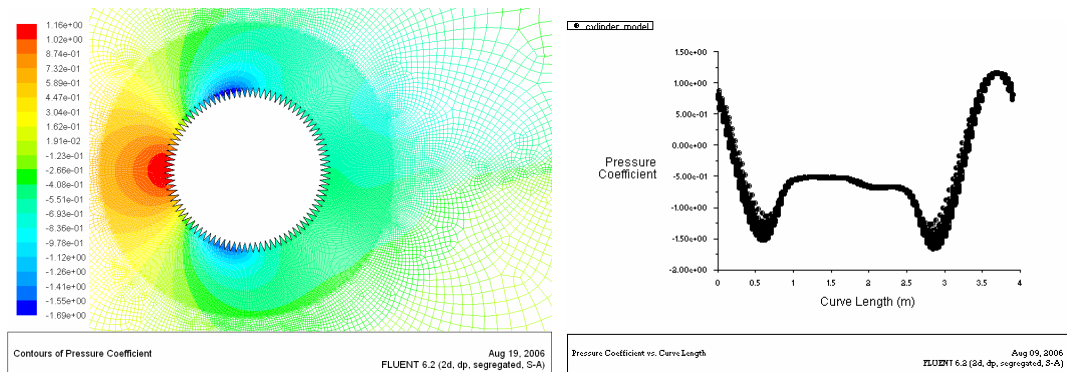


Figure E3.3: External Pressure Coefficients for 30m/s.

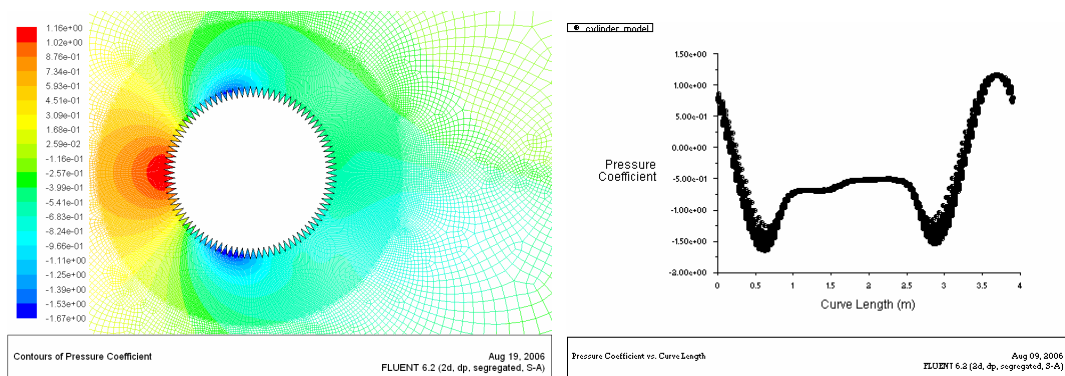


Figure E3.4: External Pressure Coefficients for 40m/s.

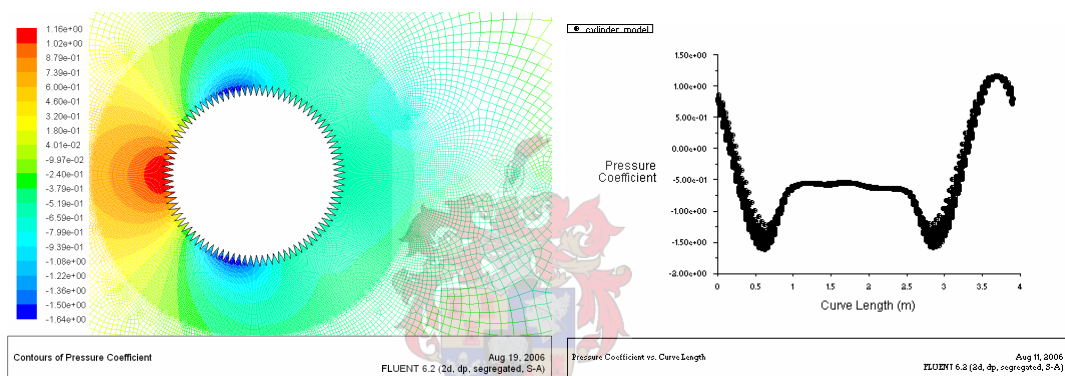


Figure E3.5: External Pressure Coefficients for 100m/s.

APPENDIX F: MATLAB PROGRAMMES

F.1 Japan: External Pressures

DIFFERENCE IN HEIGHT:

```

% SMOOTH CYLINDER

% This M-file reads in the 5 data files per wind speed (5 - 25 m/s).
% It then takes the average of the 5 readings for each wind speed.
% The average data is stored as the columns of Aav.
% The average data is split into the three rows of measurements and
% the difference in these three rows is then plotted on separate graphs
% per wind speed.

clc
clear

Ang = load('angles.txt');

for j = [5 10 15 16 17 18 19 20 25]
    wind = horzcat('N',num2str(j),'.');

    for i = 1:5
        name = horzcat(wind,num2str(i),'.dat');

        N = fopen(name,'r');
        N = textscan(N,'%f %f %f %f %f',135,'headerlines',1);

        Aall(:,i) = N(:,4);
        Aall;

    end

    Aav(:,j) = (Aall(:,1)+Aall(:,2)+Aall(:,3)+Aall(:,4)+Aall(:,4))/5;

    A_A = [Aav(1:45,j);Aav(1,j)];           % A is the top row
    A_B = [Aav(46:90,j);Aav(46,j)];        % B is the middle row
    A_C = [Aav(91:135,j);Aav(91,j)];       % C is the bottom row

    figure(j)
    plot(Ang,A_A,'r',Ang,A_B,'b',Ang,A_C,'g')
    axis ([0 360 -2.5 1.2])
    set(gca,'XTick',[0 30 60 90 120 150 180 210 240 270 300 330 360])
    grid on
    heading = horzcat('External Pressure Coefficients for Wind Speed
',num2str(j),' m/s');
    title(heading)
    xlabel('Degrees')
    ylabel('Cp')
    legend('A - Top','B - Middle','C - Bottom','Location','EastOutside')

```

```

end

% CYLINDER WITH 45 VERTICAL RIBS

% This M-file reads in the 5 data files per wind speed (5 - 25 m/s).
% It then takes the average of the 5 readings for each wind speed.
% The average data is stored as the columns of Aav.
% The average data is split into the three rows of measurements and
% the difference in these three rows is then plotted on seperate graphs
% per wind speed.

clc
clear

Ang = load('angles.txt');

for j = [5 10 15 16 17 18 19 20 25]
    wind = horzcat('A',num2str(j),'_');

    for i = 1:5
        name = horzcat(wind,num2str(i),'.dat');

        A = fopen(name,'r');
        A = textscan(A,'%f %f %f %f %f',135,'headerlines',1);

        Aall(:,i) = A{: ,4};
        Aall;

    end

    Aav(:,j) = (Aall(:,1)+Aall(:,2)+Aall(:,3)+Aall(:,4)+Aall(:,4))/5;

    A_A = [Aav(1:45,j);Aav(1,j)];           % A is the top row
    A_B = [Aav(46:90,j);Aav(46,j)];         % B is the middle row
    A_C = [Aav(91:135,j);Aav(91,j)];        % C is the bottom row

    figure(j)
    plot(Ang,A_A,'r',Ang,A_B,'b',Ang,A_C,'g')
    axis ([0 360 -1 1.2])
    set(gca,'XTick',[0 30 60 90 120 150 180 210 240 270 300 330 360])
    grid on
    heading = horzcat('External Pressure Coefficients for Wind Speed
',num2str(j),' m/s');
    title(heading)
    xlabel('Degrees')
    ylabel('Cp')
    legend('A - Top','B - Middle','C - Bottom','Location','EastOutside')

end

% CYLINDER WITH 90 VERTICAL RIBS

% This M-file reads in the 5 data files per wind speed (5 - 25 m/s).
% It then takes the average of the 5 readings for each wind speed.
% The average data is stored as the columns of Aav.
% The average data is split into the three rows of measurements and
% the difference in these three rows is then plotted on seperate graphs
% per wind speed.

```

```

clc
clear

Ang = load('angles.txt');

for j = [5 10 15 16 17 18 19 20 25]
    wind = horzcat('B',num2str(j),'_');

    for i = 1:5
        name = horzcat(wind,num2str(i),'.dat');

        B = fopen(name,'r');
        B = textscan(B,'%f %f %f %f',135,'headerlines',1);

        Aall(:,i) = B(:,4);
        Aall;

    end

    Aav(:,j) = (Aall(:,1)+Aall(:,2)+Aall(:,3)+Aall(:,4)+Aall(:,4))/5;

    A_A = [Aav(1:45,j);Aav(1,j)];           % A is the top row
    A_B = [Aav(46:90,j);Aav(46,j)];       % B is the middle row
    A_C = [Aav(91:135,j);Aav(91,j)];     % C is the bottom row

    figure(j)
    plot(Ang,A_A,'r',Ang,A_B,'b',Ang,A_C,'g')
    axis ([0 360 -1 1.2])
    set(gca,'XTick',[0 30 60 90 120 150 180 210 240 270 300 330 360])
    grid on
    heading = horzcat('External Pressure Coefficients for Wind Speed
',num2str(j),' m/s');
    title(heading)
    xlabel('Degrees')
    ylabel('Cp')

end

```

AVERAGE OVER HEIGHT (SEPARATE GRAPHS):

```

% SMOOTH CYLINDER

% This M-file reads in the 5 data files per wind speed (5 - 25 m/s).
% It then takes the average of the 5 readings for each wind speed.
% The average data is stored as the columns of Aav.
% The average data is split into the three rows of measurements and
% the average of the 3 different height readings is found.
% This single average data is stores as Aavall.
% The average Pressure Coefficient for each wind speed is then
% plotted on seperate graphs.

clc
clear

Ang = load('angles.txt');

for j = [5 10 15 16 17 18 19 20 25]
    wind = horzcat('N',num2str(j),'.');

    for i = 1:5
        name = horzcat(wind,num2str(i),'.dat');

        N = fopen(name,'r');
        N = textscan(N,'%f %f %f %f %f',135,'headerlines',1);

        Aall(:,i) = N(:,4);
        Aall;

    end

    Aav(:,j) = (Aall(:,1)+Aall(:,2)+Aall(:,3)+Aall(:,4)+Aall(:,4))/5;

    A_A = [Aav(1:45,j);Aav(1,j)];
    A_B = [Aav(46:90,j);Aav(46,j)];
    A_C = [Aav(91:135,j);Aav(91,j)];

    Aavall(:,j) = (A_A+A_B+A_C)/3;

    figure(j)
    plot(Ang,Aavall(:,j))
    axis ([0 360 -3 1.2])
    set(gca,'XTick',[0 30 60 90 120 150 180 210 240 270 300 330 360])
    grid on
    heading = horzcat('External Pressure Coefficients Cylinder Smooth
',num2str(j),' m/s');
    title(heading)
    xlabel('Degrees')
    ylabel('Cp')
    picture = horzcat('Smooth_',num2str(j));

end

```



```

% CYLINDER WITH 45 VERTICAL RIBS

% This M-file reads in the 5 data files per wind speed (5 - 25 m/s).
% It then takes the average of the 5 readings for each wind speed.
% The average data is stored as the columns of Aav.
% The average data is split into the three rows of measurements and
% the average of the 3 different height readings is found.
% This single average data is stores as Aavall.
% The average Pressure Coefficient for each wind speed is then
% plotted on seperate graphs.

clc
clear

Ang = load('angles.txt');

for j = [5 10 15 16 17 18 19 20 25]
    wind = horzcat('A',num2str(j),'_');

    for i = 1:5
        name = horzcat(wind,num2str(i),'.dat');

        A = fopen(name,'r');
        A = textscan(A,'%f %f %f %f %f',135,'headerlines',1);

        Aall(:,i) = A(:,4);
        Aall;

    end

    Aav(:,j) = (Aall(:,1)+Aall(:,2)+Aall(:,3)+Aall(:,4)+Aall(:,4))/5;

    A_A = [Aav(1:45,j);Aav(1,j)];
    A_B = [Aav(46:90,j);Aav(46,j)];
    A_C = [Aav(91:135,j);Aav(91,j)];

    Aavall(:,j) = (A_A+A_B+A_C)/3;

    figure(j)
    plot(Ang,Aavall(:,j))
    axis ([0 360 -3 1.2])
    set(gca,'XTick',[0 30 60 90 120 150 180 210 240 270 300 330 360])
    grid on
    heading = horzcat('External Pressure Coefficients Cylinder with 45
Vertical Ribs ',num2str(j),' m/s');
    title(heading)
    xlabel('Degrees')
    ylabel('Cp')

end

```

```

% CYLINDER WITH 90 VERTICAL RIBS

% This M-file reads in the 5 data files per wind speed (5 - 25 m/s).
% It then takes the average of the 5 readings for each wind speed.
% The average data is stored as the columns of Aav.
% The average data is split into the three rows of measurements and
% the average of the 3 different height readings is found.
% This single average data is stores as Aavall.
% The average Pressure Coefficient for each wind speed is then
% plotted on seperate graphs.

clc
clear

Ang = load('angles.txt');

for j = [5 10 15 16 17 18 19 20 25]
    wind = horzcat('B',num2str(j),'_');

    for i = 1:5
        name = horzcat(wind,num2str(i),'.dat');

        B = fopen(name,'r');
        B = textscan(B,'%f %f %f %f %f',135,'headerlines',1);

        Aall(:,i) = B(:,4);
        Aall;

    end

    Aav(:,j) = (Aall(:,1)+Aall(:,2)+Aall(:,3)+Aall(:,4)+Aall(:,4))/5;

    A_A = [Aav(1:45,j);Aav(1,j)];
    A_B = [Aav(46:90,j);Aav(46,j)];
    A_C = [Aav(91:135,j);Aav(91,j)];

    Aavall(:,j) = (A_A+A_B+A_C)/3;

    figure(j)
    plot(Ang,Aavall(:,j))
    axis ([0 360 -3 1.2])
    set(gca,'XTick',[0 30 60 90 120 150 180 210 240 270 300 330 360])
    grid on
    heading = horzcat('External Pressure Coefficients Cylinder with 90
Vertical Ribs ',num2str(j),' m/s');
    title(heading)
    xlabel('Degrees')
    ylabel('Cp')

end

```

AVERAGE OVER HEIGHT (ONE GRAPH):

```

% SMOOTH CYLINDER

% This M-file reads in the 5 data files per wind speed (5 - 25 m/s).
% It then takes the average of the 5 readings for each wind speed.
% The average data is stored as the columns of Aav.
% The average data is split into the three rows of measurements and
% the average of the 3 different height readings is found.
% This single average data is stores as Aavall.
% The average Pressure Coefficient for each wind speed is then
% plotted together on one graph.

clc
clear

Ang = load('angles.txt');

for j = [5 10 15 16 17 18 19 20 25]
    wind = horzcat('N',num2str(j),'.');

    for i = 1:5
        name = horzcat(wind,num2str(i),'.dat');

        N = fopen(name,'r');
        N = textscan(N,'%f %f %f %f',135,'headerlines',1);

        Aall(:,i) = N(:,4);
        Aall;

    end

    Aav(:,j) = (Aall(:,1)+Aall(:,2)+Aall(:,3)+Aall(:,4)+Aall(:,4))/5;

    A_A = [Aav(1:45,j);Aav(1,j)];
    A_B = [Aav(46:90,j);Aav(46,j)];
    A_C = [Aav(91:135,j);Aav(91,j)];

    Aavall(:,j) = (A_A+A_B+A_C)/3;

end

smooth = Aavall(:, [5 10 15 16 17 18 19 20 25]);
save smooth.out smooth -ASCII

figure(1)
plot(Ang,Aavall(:, [5 10 15 16 17 18 19 20 25]))
axis ([0 360 -3 1.2])
set(gca,'XTick',[0 30 60 90 120 150 180 210 240 270 300 330 360])
grid on
heading = horzcat('External Pressure Coefficients for Smooth
Cylinder');
title(heading)
xlabel('Degrees')
ylabel('Cp')
legend('5 m/s','10 m/s','15 m/s','16 m/s','17 m/s','18 m/s','19
m/s','20 m/s','25 m/s','Location','EastOutside')

```

```

% CYLINDER WITH 45 VERTICAL RIBS

% This M-file reads in the 5 data files per wind speed (5 - 25 m/s).
% It then takes the average of the 5 readings for each wind speed.
% The average data is stored as the columns of Aav.
% The average data is split into the three rows of measurements and
% the average of the 3 different height readings is found.
% This single average data is stores as Aavall.
% The average Pressure Coefficient for each wind speed is then
% plotted together on one graph.

clc
clear

Ang = load('angles.txt');

for j = [5 10 15 16 17 18 19 20 25]
    wind = horzcat('A',num2str(j),'_');

    for i = 1:5
        name = horzcat(wind,num2str(i),'.dat');

        A = fopen(name,'r');
        A = textscan(A,'%f %f %f %f %f',135,'headerlines',1);

        Aall(:,i) = A(:,4);
        Aall;

    end

    Aav(:,j) = (Aall(:,1)+Aall(:,2)+Aall(:,3)+Aall(:,4)+Aall(:,4))/5;

    A_A = [Aav(1:45,j);Aav(1,j)];
    A_B = [Aav(46:90,j);Aav(46,j)];
    A_C = [Aav(91:135,j);Aav(91,j)];

    Aavall(:,j) = (A_A+A_B+A_C)/3;

end

spike = Aavall(:,[5 10 15 16 17 18 19 20 25]);
save 45spike.out spike -ASCII

figure(1)
plot(Ang,Aavall(:,[5 10 15 16 17 18 19 20 25]))
axis ([0 360 -3 1.2])
set(gca,'XTick',[0 30 60 90 120 150 180 210 240 270 300 330 360])
grid on
heading = horzcat('External Pressure Coefficients Cylinder with 45
Vertical Ribs');
title(heading)
xlabel('Degrees')
ylabel('Cp')
legend('5 m/s','10 m/s','15 m/s','16 m/s','17 m/s','18 m/s','19
m/s','20 m/s','25 m/s','Location','EastOutside')

```

```

% CYLINDER WITH 90 VERTICAL RIBS

% This M-file reads in the 5 data files per wind speed (5 - 25 m/s).
% It then takes the average of the 5 readings for each wind speed.
% The average data is stored as the columns of Aav.
% The average data is split into the three rows of measurements and
% the average of the 3 different height readings is found.
% This single average data is stores as Aavall.
% The average Pressure Coefficient for each wind speed is then
% plotted together on one graph.

clc
clear

Ang = load('angles.txt');

for j = [5 10 15 16 17 18 19 20 25]
    wind = horzcat('B',num2str(j),'_');

    for i = 1:5
        name = horzcat(wind,num2str(i),'.dat');

        B = fopen(name,'r');
        B = textscan(B,'%f %f %f %f %f',135,'headerlines',1);

        Aall(:,i) = B(:,4);
        Aall;

    end

    Aav(:,j) = (Aall(:,1)+Aall(:,2)+Aall(:,3)+Aall(:,4)+Aall(:,4))/5;

    A_A = [Aav(1:45,j);Aav(1,j)];
    A_B = [Aav(46:90,j);Aav(46,j)];
    A_C = [Aav(91:135,j);Aav(91,j)];

    Aavall(:,j) = (A_A+A_B+A_C)/3;

end

spike = Aavall(:, [5 10 15 16 17 18 19 20 25]);
save 90spike.out spike -ASCII

figure(1)
plot(Ang,Aavall(:, [5 10 15 16 17 18 19 20 25]))
axis ([0 360 -3 1.2])
set(gca,'XTick',[0 30 60 90 120 150 180 210 240 270 300 330 360])
grid on
heading = horzcat('External Pressure Coefficients for Cylinder with 90
Vertical Ribs');
title(heading)
xlabel('Degrees')
ylabel('Cp')
legend('5 m/s','10 m/s','15 m/s','16 m/s','17 m/s','18 m/s','19
m/s','20 m/s','25 m/s','Location','EastOutside')

```

COMPARISON OF THREE MODELS:

```
% This m-file plots the pressure distributions for the 3 models on one
graph.
% green is the smooth model
% red is the 45 spike model
% blue is the 90 spike model

clc
clear

Ang = load('angles.txt');
smooth = load('smooth.out');
spike45 = load('45spike.out');
spike90 = load('90spike.out');

figure(1)
plot(Ang,smooth,'g',Ang,spike45,'r',Ang,spike90,'b')
axis ([0 360 -3 1.2])
set(gca,'XTick',[0 30 60 90 120 150 180 210 240 270 300 330 360])
grid on
title('External Pressure Coefficient Comparison')
xlabel('Degrees')
ylabel('Cp')
text(130,-1.1,'green = smooth')
text(130,-1.4,'red = 45 spike')
text(130,-1.7,'blue = 90 spike')
```



F.2 Japan: Calculating Drag

```

% SMOOTH CYLINDER

% This M-file reads in the 5 data files per wind speed (5 - 25 m/s).
% It then takes the average of the 5 readings for each wind speed.
% The average data is stored as the columns of Aav.
% The average data is split into the three rows of measurements.
% The external pressure coefficients are used to calculate
% the drag coefficient.
% This is done for all three heights and then plotted against
% windspeed and Reynolds number

clc
clear

Ang = load('angles.txt')

for j = [5 10 15 16 17 18 19 20 25]
    wind = horzcat('N',num2str(j),'.');

    CdA(1,j) = 0;
    CdB(1,j) = 0;
    CdC(1,j) = 0;

    for i = 1:5
        name = horzcat(wind,num2str(i),'.dat');

        N = fopen(name,'r');
        N = textscan(N,'%f %f %f %f %f',135,'headerlines',1);

        Aall(:,i) = N(:,4);
        Aall;

    end

    Aav(:,j) = (Aall(:,1)+Aall(:,2)+Aall(:,3)+Aall(:,4)+Aall(:,4))/5;

    A_A = [Aav(1:45,j);Aav(1,j)]           % A is the top row
    A_B = [Aav(46:90,j);Aav(46,j)];       % B is the middle row
    A_C = [Aav(91:135,j);Aav(91,j)];      % C is the bottom row

    for k = 1:46

        CdA(1,j) = CdA(1,j) + (0.5*8*pi/180*A_A(k,1)*cos(Ang(k,1)*pi/180))
        CdB(1,j) = CdB(1,j) + (0.5*8*pi/180*A_B(k,1)*cos(Ang(k,1)*pi/180));
        CdC(1,j) = CdC(1,j) + (0.5*8*pi/180*A_C(k,1)*cos(Ang(k,1)*pi/180));

    end

end

CDA = CdA(1,[5 10 15 16 17 18 19 20 25])'
```



```

CDB = CdB(1,[5 10 15 16 17 18 19 20 25])'
CDC = CdC(1,[5 10 15 16 17 18 19 20 25])'

WIND = [5 10 15 16 17 18 19 20 25];
RE = [9.9E3 2E4 3E4 3.2E4 3.4E4 3.6E4 3.8E4 4E4 5E4];

figure(1)
plot(WIND,CDA,'r',WIND,CDB,'b',WIND,CDC,'g')
axis ([0 30 0 1])
set(gca,'YTick',[0 0.1 0.2 0.3 0.4 0.5 0.6 0.7 0.8 0.9 1])
grid on
heading = horzcat('Drag Coefficient for Smooth Cylinder against Wind
Speed');
title(heading)
xlabel('Velocity m/s')
ylabel('Cd')

figure(2)
plot(RE,CDA,'r',RE,CDB,'b',RE,CDC,'g')
axis ([1000 5E4 -0.5 1.5])
set(gca,'YTick',[0 0.1 0.2 0.3 0.4 0.5 0.6 0.7 0.8 0.9 1])
grid on
heading = horzcat('Drag Coefficient for Smooth Cylinder against
Reynolds Number');
title(heading)
xlabel('Re')
ylabel('Cd')

% CYLINDER WITH 45 VERTICAL RIBS

% This M-file reads in the 5 data files per wind speed (5 - 25 m/s).
% It then takes the average of the 5 readings for each wind speed.
% The average data is stored as the columns of Aav.
% The average data is split into the three rows of measurements.
% The external pressure coefficients are used to calculate
% the drag coefficient.
% This is done for all three heights and then plotted against
% windspeed and Reynolds number

clc
clear

Ang = load('angles.txt');

for j = [5 10 15 16 17 18 19 20 25]
    wind = horzcat('A',num2str(j),'_');

    CdA(1,j) = 0;
    CdB(1,j) = 0;
    CdC(1,j) = 0;

    for i = 1:5
        name = horzcat(wind,num2str(i),'.dat');

        A = fopen(name,'r');
        A = textscan(A,'%f %f %f %f %f',135,'headerlines',1);

        Aall(:,i) = A(:,4);

```

```

    Aall;

end

Aav(:,j) = (Aall(:,1)+Aall(:,2)+Aall(:,3)+Aall(:,4)+Aall(:,4))/5;

A_A = [Aav(1:45,j);Aav(1,j)];           % A is the top row
A_B = [Aav(46:90,j);Aav(46,j)];       % B is the middle row
A_C = [Aav(91:135,j);Aav(91,j)];     % C is the bottom row

for k = 1:46

    CdA(1,j) = CdA(1,j) + (0.5*8*pi/180*A_A(k,1)*cos(Ang(k,1)*pi/180));
    CdB(1,j) = CdB(1,j) + (0.5*8*pi/180*A_B(k,1)*cos(Ang(k,1)*pi/180));
    CdC(1,j) = CdC(1,j) + (0.5*8*pi/180*A_C(k,1)*cos(Ang(k,1)*pi/180));

end

end

CDA = CdA(1,[5 10 15 16 17 18 19 20 25])'
CDB = CdB(1,[5 10 15 16 17 18 19 20 25])'
CDC = CdC(1,[5 10 15 16 17 18 19 20 25])'

WIND = [5 10 15 16 17 18 19 20 25];
RE = [9.9E3 2E4 3E4 3.2E4 3.4E4 3.6E4 3.8E4 4E4 5E4];

figure(1)
plot(WIND,CDA,'r',WIND,CDB,'b',WIND,CDC,'g')
axis ([0 30 0 1])
set(gca,'YTick',[0 0.1 0.2 0.3 0.4 0.5 0.6 0.7 0.8 0.9 1])
grid on
heading = horzcat('Drag Coefficient for Smooth Cylinder against Wind
Speed');
title(heading)
xlabel('Velocity m/s')
ylabel('Cd')

figure(2)
plot(RE,CDA,'r',RE,CDB,'b',RE,CDC,'g')
axis ([1000 5E4 -0.5 1.5])
set(gca,'YTick',[0 0.1 0.2 0.3 0.4 0.5 0.6 0.7 0.8 0.9 1])
grid on
heading = horzcat('Drag Coefficient for Smooth Cylinder against
Reynolds Number');
title(heading)
xlabel('Re')
ylabel('Cd')

% CYLINDER WITH 90 VERTICAL RIBS

% This M-file reads in the 5 data files per wind speed (5 - 25 m/s).
% It then takes the average of the 5 readings for each wind speed.
% The average data is stored as the columns of Aav.

```

```

% The average data is split into the three rows of measurements.
% The external pressure coefficients are used to calculate
% the drag coefficient.
% This is done for all three heights and then plotted against
% windspeed and Reynolds number

clc
clear

Ang = load('angles.txt');

for j = [5 10 15 16 17 18 19 20 25]
    wind = horzcat('B',num2str(j),'_');

    CdA(1,j) = 0;
    CdB(1,j) = 0;
    CdC(1,j) = 0;

    for i = 1:5
        name = horzcat(wind,num2str(i),'.dat');

        B = fopen(name,'r');
        B = textscan(B,'%f %f %f %f %f',135,'headerlines',1);

        Aall(:,i) = B(:,4);
        Aall;

    end

    Aav(:,j) = (Aall(:,1)+Aall(:,2)+Aall(:,3)+Aall(:,4)+Aall(:,4))/5;

    A_A = [Aav(1:45,j);Aav(1,j)];           % A is the top row
    A_B = [Aav(46:90,j);Aav(46,j)];         % B is the middle row
    A_C = [Aav(91:135,j);Aav(91,j)];        % C is the bottom row

    for k = 1:46

        CdA(1,j) = CdA(1,j) + (0.5*8*pi/180*A_A(k,1)*cos(Ang(k,1)*pi/180));
        CdB(1,j) = CdB(1,j) + (0.5*8*pi/180*A_B(k,1)*cos(Ang(k,1)*pi/180));
        CdC(1,j) = CdC(1,j) + (0.5*8*pi/180*A_C(k,1)*cos(Ang(k,1)*pi/180));

    end

end

CDA = CdA(1,[5 10 15 16 17 18 19 20 25])'
CDB = CdB(1,[5 10 15 16 17 18 19 20 25])'
CDC = CdC(1,[5 10 15 16 17 18 19 20 25])'

WIND = [5 10 15 16 17 18 19 20 25];
RE = [9.9E3 2E4 3E4 3.2E4 3.4E4 3.6E4 3.8E4 4E4 5E4];

figure(1)
plot(WIND,CDA,'r',WIND,CDB,'b',WIND,CDC,'g')
axis ([0 30 0 1])

```

```
set(gca, 'YTick', [0 0.1 0.2 0.3 0.4 0.5 0.6 0.7 0.8 0.9 1])
grid on
heading = horzcat('Drag Coefficient for Smooth Cylinder against Wind
Speed');
title(heading)
xlabel('Velocity m/s')
ylabel('Cd')

figure(2)
plot(RE, CDA, 'r', RE, CDB, 'b', RE, CDC, 'g')
axis ([1000 5E4 -0.5 1.5])
set(gca, 'YTick', [0 0.1 0.2 0.3 0.4 0.5 0.6 0.7 0.8 0.9 1])
grid on
heading = horzcat('Drag Coefficient for Smooth Cylinder against
Reynolds Number');
title(heading)
xlabel('Re')
ylabel('Cd')
```



LIST OF ILLUSTRATIONS

Figure 1.1: Solar Chimney Principle (Schlaich, 2004)

Figure 1.2: Drag Coefficient for a Smooth Cylinder

Figure 2.1: The Saguaro Cactus (Talley, 2002)

Figure 2.2: Pressure distribution of all cylinders at $Re = 1.1 \times 10^5$ (Talley, 2002)

Figure 3.1: The Model of the Closed Circuit Wind Tunnel, Shimizu Corporation, Tokyo, Japan.

Figure 3.2: Three cylinder models of height 1000 mm used for this test.

Figure 3.3: The difference in pressure distributions with height for the vertically ribbed cylinders for 20m/s.

Figure 3.4: The difference in pressure distributions with height for the smooth cylinder for 16m/s.

Figure 3.5: The difference in pressure distributions with height for the smooth cylinder for 20m/s.

Figure 3.6: External Pressure Coefficients of Cylinder with 45 Vertical Ribs.

Figure 3.7: External Pressure Coefficients of Cylinder with 90 Vertical Ribs.

Figure 3.8: External Pressure Coefficients of the Smooth Cylinder.

Figure 3.9: Calculated Drag Coefficients for the three Cylinders

Figure 4.1: General Layout of the Wind Tunnel (Du Buisson, J.J. 1988).

Figure 4.2: Three cylinder models of height 285 mm used for this test.

Figure 4.3: Drag Coefficient graph for flow around a Cylinder. (Potter, 2002)

Figure 4.4: Drag Coefficient graph for Test Cylinder 1, Smooth.

Figure 4.5: Drag Coefficient graph for Test Cylinder 2, Small Vertical Ribs.

Figure 4.6: Drag Coefficient graph for Test Cylinder 3, Large Vertical Ribs.

Figure 5.1: The cylinder model and air flow domain as created in GAMBIT.

Figure 5.2: The meshed flow domain for the smooth cylinder.

Figure 5.3: The meshed flow domain for the smooth cylinder zoomed.

- Figure 5.4:** The meshed flow domain for the cylinder with 45 vertical ribs zoomed.
- Figure 5.5:** The meshed flow domain for the cylinder with 90 vertical ribs zoomed.
- Figure 5.6:** Drag Coefficient comparison between Literature and Theoretical CFD analysis.
- Figure 5.7:** Comparison of Drag coefficients
- Figure 5.8:** Drag Coefficient graph for Cylinder with 45 Vertical Ribs.
- Figure 5.9:** Drag Coefficient graph for Cylinder with 90 Vertical Ribs.
- Figure 5.10:** External Pressure Coefficients for the Smooth Cylinder for 30m/s.
- Figure 5.11:** External Pressure Coefficients for the Ribbed Cylinders for 30m/s.
- Figure 5.12:** External Pressure Coefficients for the Cylinder with 45 Vertical Ribs for a Wind Speed of 30m/s as generated by FLUENT.
- Figure 5.13:** External Pressure Coefficients Contours for the Cylinder with 45 Vertical Ribs for a Wind Speed of 30m/s as generated by FLUENT.
- Figure 5.14:** External Pressure Coefficients for a Wind Speed of 30m/s.
- Figure 5.15:** Contours of External Pressure Coefficients for the Smooth Cylinder for a Wind Speed of 30m/s.
- Figure 5.16:** Contours of External Pressure Coefficients for the Cylinder with 45 Vertical Ribs for a Wind Speed of 30m/s.
- Figure 5.17:** Contours of External Pressure Coefficients for the Cylinder with 90 Vertical Ribs for a Wind Speed of 30m/s.
- Figure 6.1:** Drag Coefficient Comparison for the Solar Chimney

LIST OF TABLES

Table 4.1: Dimensions of the Wind Tunnel

LIST OF EQUATIONS

Equation 1.1: $R_e = \frac{vD}{\nu}$

Equation 1.2: $C_d = \frac{F_d}{0.5 \rho v^2 A}$

Equation 1.3: $St = \frac{fL}{v}$

Equation 3.1: $C_d = 0.5 \int_0^{2\pi} C_p \cos \theta d\theta$



Equation 4.1: $C_d = F_d / (0.5 \times \rho \times v^2 \times A)$

Equation 6.1: $F_d = 0.5 \times C_d \times \rho \times v^2 \times A$